Study of the polar mesopause region by remote sensing of OH airglow

Hidehiko Suzuki

DOCTOR OF PHILOSOPHY

Department of Polar Science,
School of Multidisciplinary Sciences,
The Graduate University for Advanced Studies

March, 2010

Acknowledgement

The author wishes to express his sincere gratitude to Dr. Masaki Tsutsumi of his appropriate guidance, advises, stimulating supervision for the present work, and for the careful reading of the manuscript. The author deeply thanks Professor Makoto Taguchi for his guidance and many kinds of arrangements for field observations in Arctic and Antarctic which are essential for the present study. The author is also thankful to Professor Takuji Nakamura for his appropriate advises and comments for the present study and continuous encouragements to achieve this work.

The author expresses his gratitude to Dr. Yoshihiro Tomikawa for valuable discussions and giving him a general knowledge about middle and upper atmospheric climatology through the reading circles. The author thanks Dr. Mitsumu Ejiri, Dr. Yoshimasa Tanaka, Dr. Shin Suzuki and Dr. Yasunobu Ogawa for the valuable comments, useful and helpful discussions and criticism in weekly science meeting held in National Institute of Polar Research. The author is also indebted to Dr. Hiroyuki Shinagawa.

Special thanks are due to Professor Natsuo Sato and Professor Hisao Yamagishi for their management to realize my wintering observation in Syowa Station, Antarctica. The author also thanks Professor Hiroshi Miyaoka, Professor Akira Kadokura, and Dr. Akira Sessai Yukimatsu for helping with the data analysis of aurora and observation in Syowa. The author is grateful to Dr. Masaki Okada for his kindly help and supports for observations in Syowa during wintering period of 49th Japanese Antarctic Research Expedition (JARE49). The author also wishes to express his appreciation to all member of JARE49 for their cooperation to his observation.

The author deeply thanks Ms. Nobuko Takahama, Ms. Haruko Anyoji and all staffs of National Institute of Polar Research for supporting his study life with many tangible and untangible helps. Thanks are also due to all students of Graduate University for Advanced Studies for encouraging each other during his study.

Remarkable auroral activity on 3rd of Sep, 2008.

Abstract

The OH Meinel band emissions are the brightest night airglow emissions in the near-infrared regions, and peak at mesopause altitudes. Since the intensity distribution in these vibration-rotation bands is quickly equalized to that determined by the local kinetic temperature, the OH rotational temperature can be derived from the spectrum of OH airglow. This technique has been widely used as a conventional and reliable method of temperature measurement in the mesopause region, especially in the middle- and low-latitude regions. However, it is known to be difficult to apply in the polar regions, because auroral emissions contaminate OH airglow spectra. There are a few examples of OH rotational temperature observations conducted in Antarctic for the purposes of studying the relationship between aurora activity and OH rotational temperature. However, highly energetic auroral electrons can reach altitudes just below the mesopause (~90 km) and can cause heating of the neutral atmosphere at that altitude. There are virtually no previous reports that show a quantitative relationship between auroral precipitations and OH rotational temperature.

A fast high-resolution spectrometer designed specifically to observe the spectrum of the OH vibrational-rotational band in the auroral zone has been developed. The OH 8-4 band around the 950-nm wavelength region in the nightglow spectrum was selected as the most suitable vibration-rotation band for observation in polar regions, based on Arctic survey observations. Its suitability lies in the fact that it is less susceptible to contamination from strong auroral emission. The new spectrometer comprises a fast optical system, a transmission grating and a CCD camera. The operating spectral region just encompasses the OH 8-4 band (900-990 nm) and a moderate spectral resolution of 0.27 nm is realized. A back-illuminated CCD with an infrared-enhanced quantum efficiency is used as the imaging device. The sensitivity and spectral resolution of the spectrometer were calibrated at the National Institute of Polar Research (NIPR).

The instrument was installed in the Optical Building at Syowa Station in February, 2008 by the 49th Japanese Antarctic Research Expedition. The instrumental field-of-view of 4.5×0.007 deg is centered on the local magnetic zenith. The nominal exposure time is 1 min.

The total dataset consists of observations over 153 nights during the 2008 austral winter season at Syowa Station. The dataset shows both short-term (several minutes) and long-term (seasonal) variations. Typical temperature trends (high in winter and low in summer) in the polar mesopause region are also evident. These trends are very similar to those observed at the Davis Station which is located at nearly the same latitude as the Syowa Station. In addition to the seasonal trend, large-scale heating and cooling is seen over a period of several days.

Short-term variations which relate to auroral activity can also be observed. Only six nights of data was found to be suitable, in terms of weather conditions and auroral activity, to study the relationship between auroral precipitations and OH airglow variations. In particular, a significant increase in the rotational temperature and a decrease in the airglow intensity related to auroral activity were identified on the night of March 27-28, 2008, but no such variations were seen on other nights. The horizontal magnetic-field disturbance on the night of March 27-28 was the largest observed during the entire winter, and cosmic radio noise absorption was also very strong. These facts indicate that a large flux of high-energy auroral particles precipitated during this night. It is suggested that the observed variations in the OH rotational temperature and airglow intensity were caused by a lowering of the average airglow altitude as a result of OH depletion in the upper part of the layer where high-energy auroral particles can reach.

Although in normal auroral activity there are no auroral effects, this study reveals the occurrence of rapid fluctuations related to very high auroral activity or hard particle precipitation in the polar mesopause region.

Table of contents

The list of figures

The list of tables

1 Introduction

1-1 General introduction of the middle atmosphere

The Earth's atmosphere is generally divided into four vertical regions on the basis of their temperature structure. Figure 1-1 shows the annual global mean temperature profile produced by the CIRA86 (COSPAR International Reference Atmosphere) model [Fleming et al., 1988]. In principle, the regions are separated by points of zero temperature gradient. The region from the ground to an altitude of 10~15 km, where most of meteorological phenomena which directly affect our life occur, is called the troposphere. It should be noted that there are several different definitions of the tropopose, although the details are not considered here. The atmospheric temperature in the troposphere decreases with increasing altitude. Therefore this region is generally unstable and subject to active convection which gives rise to most of the familiar climatological phenomena. Above the troposphere, a region called the stratosphere extends up to an altitude of 50 km. In this region, the temperature increases with altitude and achieves a maximum at an altitude of about 50 km, which is referred to as the stratopause. The increase in temperature with altitude in the stratosphere is caused by absorption of solar ultraviolet radiation by ozone molecules. This positive temperature gradient makes the stratosphere highly stable, and airplanes cruise through this region for most of their course during long flights. The total mass of atmosphere confined below the stratopause accounts for over 99.9% of the Earth’s atmosphere.

The region from 50 km to about 90 km is called the mesosphere. The upper limit of the mesosphere is called the mesopause, and it is here that the lowest atmospheric temperatures occur during the summer. This region has an atmospheric density less than 1/10000 that at ground level, and the atmosphere mainly consists of neutral species. Because of its low density this region is characterized by many interesting phenomena. In the upper part of the mesosphere, there are some ionized species created by dissociation

of atmospheric molecules by solar radiation or energetic particles which penetrate into this region. However, the density of charged species is still lower than that of neutral species. Therefore, the mesopause is a boundary region where both electromagnetic phenomena and neutral atmospheric dynamics play important roles. The complexity of the mesopause region makes it difficult to form a clear understanding of its behavior. Consequently, much study is required to clarify the dynamics of this region. A detailed review of the latest investigations of the mesosphere and the mesopause is given below.

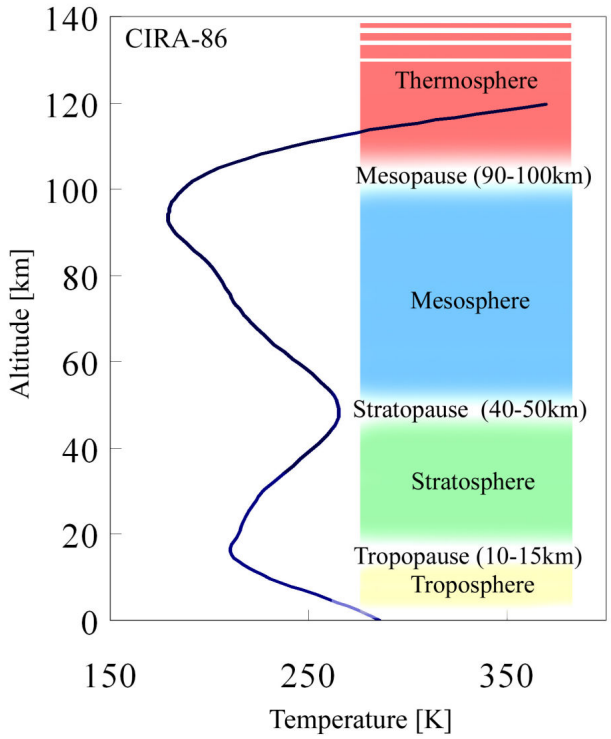

Figure 1-1 Annual global mean of temperature profile given by the CIRA86, empirical model. The terminologies for divided layers and boundaries are also denoted.

The primary source of energy input for the mesosphere is solar radiation. In particular, absorption of UV radiation (1~300 nm) by oxygen and ozone molecules has both direct and indirect effects on the energy balance in the mesosphere. The indirect effect involves modulation of the ozone concentration. Ozone plays an important role in chemical reactions occurring in the mesosphere. According to Mlynczak [1997], ozone is

responsible for 80% of exothermic chemical reactions in this region. A primary cooling mechanism in the mesosphere is radiative cooling by infrared active species such as CO_2, O_3, H_2O, and NO. Emissions from excited atmospheric species due to electronic transitions are referred to as airglow. Airglow is not a direct cooling mechanism but causes changes to the degree of solar heating or the efficiency of chemical reactions. Sources of energy and temperature variations in the mesosphere and lower thermosphere are listed in Table 1-1 (Quoted from Table 1 of Beig et al. [2008]).

Solar-particle precipitation is also an indirect source of energy input to the mesosphere. Unlike solar irradiance, its amplitude varies more drastically. In particular, CME (coronal mass ejection) events, the emission of energetic particles from flares rising from the surface of the Sun, occur almost at random and can vary the thermal structure of the mesosphere. Evidence of destruction of O_3 by solar-storm events associated with CME was reported by Seppälä et al. [2004] and Rohen et al. [2005].

Atmospheric motion in the mesosphere is not solely determined by a thermal structure involving simple radiative equilibrium and geostrophic wind relationships. Other dominant influences on the dynamics of the mesosphere include atmospheric waves such as tides, planetary waves, and internal gravity waves. These waves are excited mainly in the troposphere or lower stratosphere, and propagate to the lower-density upper atmosphere, where their amplitude increases in order to conserve their energy density. Thus, the wave amplitude can become very large in the upper mesosphere and mesopause regions. Figure1-2(a) shows an example of amplitude increase of an inertial gravity wave in the mesosphere observed with the MU radar in Shigaraki (34.9°N, 136.1°E) [Muraoka et al., 1988]. The wave amplitude grows exponentially with altitude from 64 to 80 km, corresponding to an exponential decrease in atmospheric density. One thing to note here, however, is that wave amplitude growth stops around 80 km, corresponding to dissipation of the gravity wave in the upper mesosphere. In general, gravity waves disintegrate due to convective and dynamic

instabilities [Fritts and Rostogi, 1985]. The significance of momentum flux deposition by wave breaking for global circulation in the mesosphere is described in Section 1-2.

The presence of gravity waves can also be directly detected by imaging techniques. Figure 1-3 shows airglow images observed by a sensitive CCD all-sky camera [Taylor et al., 1995]. Horizontal wave structure caused by a gravity wave can be clearly seen in the airglow image. Since the peak height is different for each airglow layer, the difference between the wave patterns in simultaneously-observed image sequences such as Figure 1-3 is an indication of the vertical structure of the wave. The imaging of airglow by an all-sky imager is a very effective method to directly measure the horizontal velocity, horizontal wavelength, and amplitude of gravity waves.

As mentioned above, the role of gravity waves is very important in the mesosphere. The effect of global meridional circulation driven by the breaking of gravity waves on the polar mesopause structure is described in the next section.

Table 1-1 Source of energy or temperature variation for the mesosphere and lower thermosphere. (This table is made based on Beig et al. [2008])

Source of energy variation	Summary
Solar heating	Absorption of UV by O_2, O_3.
Chemical heating	$H + O_3 \rightarrow OH + O_2$
	$H + O_2 + M \rightarrow HO_2 + M$
	$O + OH \rightarrow H + O_2$
	$O + HO_2 \rightarrow OH + O_2$
	$O + O + M \rightarrow O_2 + M$
	$O + O_2 + M \rightarrow O_3 + M$
	$O + O_3 + M \rightarrow O_2 + O_2 + M$
Radiative cooling	Infrared emission from, CO_2, O_3, NO, H_2O
Airglow (Energy loss)	O_2, CO_2, OH, O_3

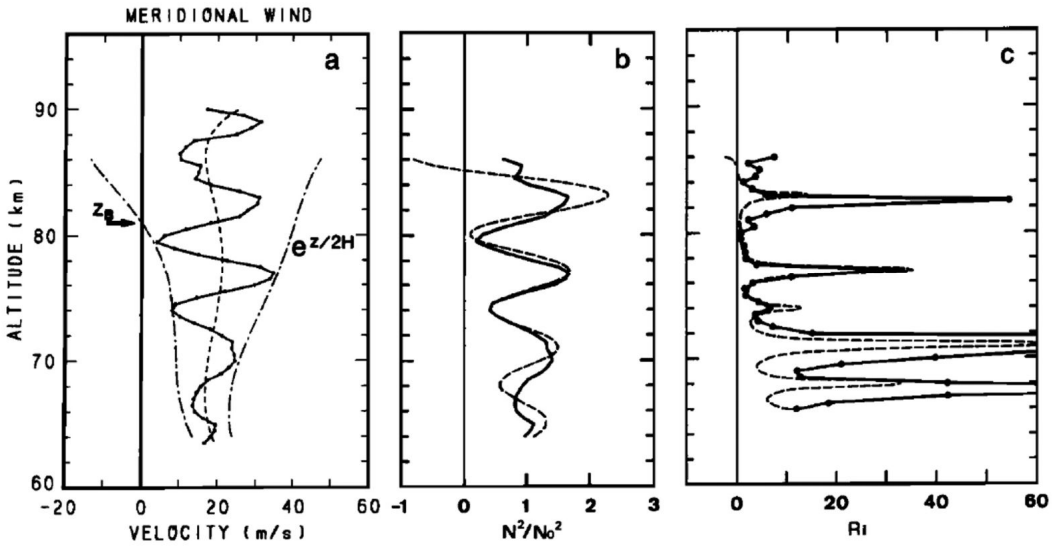

Figure1-2 A comparison between height profiles of (a) meridional wind velocity observed by the MU radar, (b)normalized total static stability (N^2/N_0^2) and (c) Richardson number (Ri) in the mesosphere. The solid, dashed and dot dashed lines in the wind profile indicate a measured meridional wind, the mean flow and an exponential growth of the wind perturbation, respectively. [Muraoka et al., 1988]

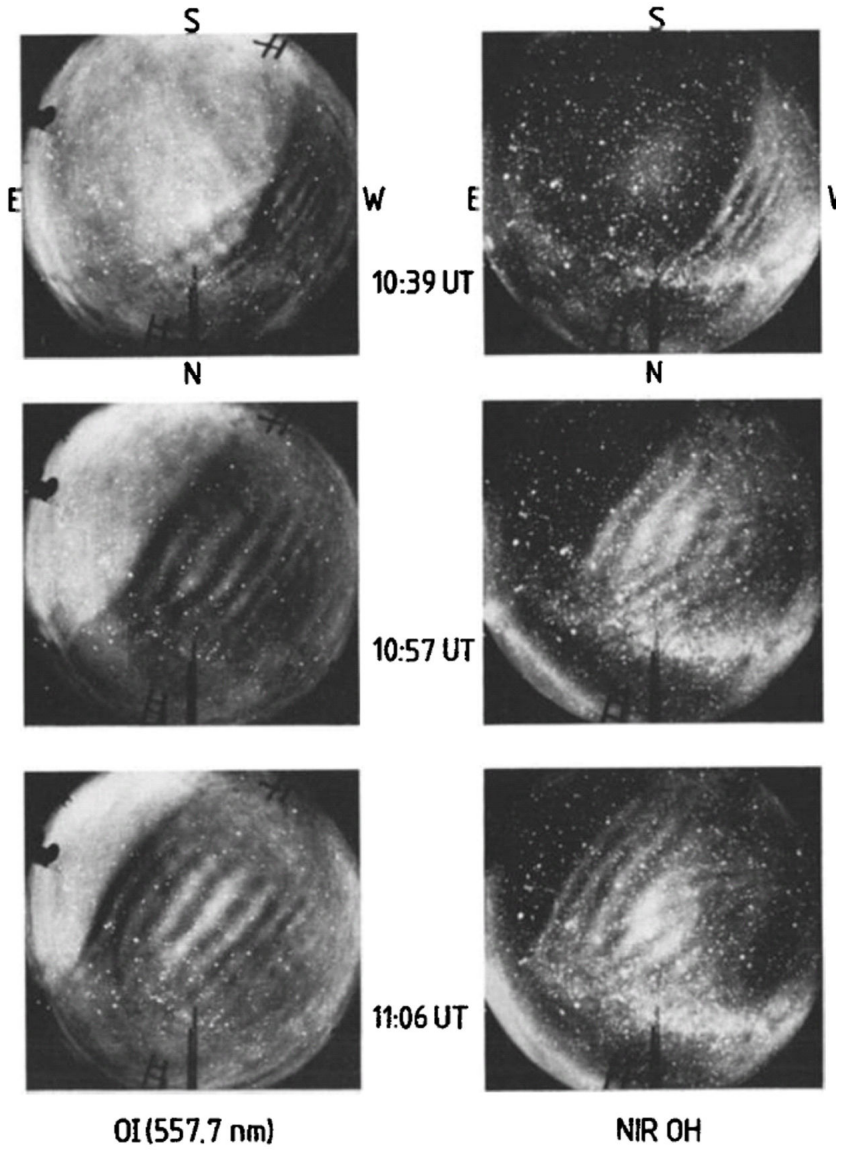

Figure 1-3 Sequence of all-sky CCD images showing a rapid transit of a wave event at NIR OH (right) and OI(557.7 nm) (left) wavelengths (integration time for OH and OI are 20 and 90 sec, respectively.) [Taylor et al., 1995].

1-2 Polar mesopause region.

Perturbations induced by gravity waves are major sources of atmospheric motion in the mesopause and upper mesosphere as mentioned in the previous section. In the polar region, the seasonal variation of the temperature in the mesopause region is driven by meridional global circulation induced by gravity wave breaking. According to the theory presented by Lindzen [1981], atmospheric acceleration at mesopause altitudes in low and middle latitudes caused by gravity wave breaking causes global meridional circulation which flows from the summer hemisphere to the winter hemisphere. There is upward motion that gives rise to adiabatic cooling of the atmosphere in the polar summer mesopause region from which the circulation starts, while in the winter mesopause regions, the end point of the circulation, descending motion causes adiabatic heating. Figure 1-4 shows a schematic drawing of global meridional circulation induced by gravity wave breaking at the mesopause.

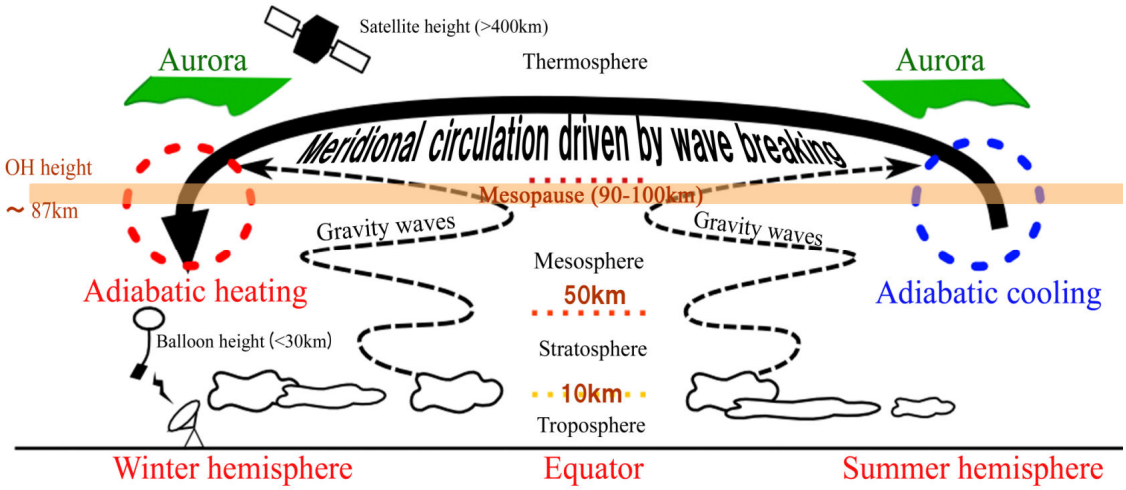

Figure 1-4. A schematic drawing of global meridional circulation induced by the gravity wave breaking in the mesopause region. Some related phenomena and altitudes of observations by several methods are also described.

This gravity-wave-driven global circulation leads to the presence of a peculiar temperature structure in the polar mesopause region. Figure 1-5 shows latitude-altitude cross sections of zonal mean temperature calculated using the global climatological model reported by Chandra et al. [1990]. The seasonal behavior of the temperature at the mesopause altitude appears curious in that it is high in winter and low in summer, although in the polar regions there are almost 24 hours of sunlight in summer and no daylight at all in mid winter. This is another illustration of the importance of gravity waves in the mesopause regions.

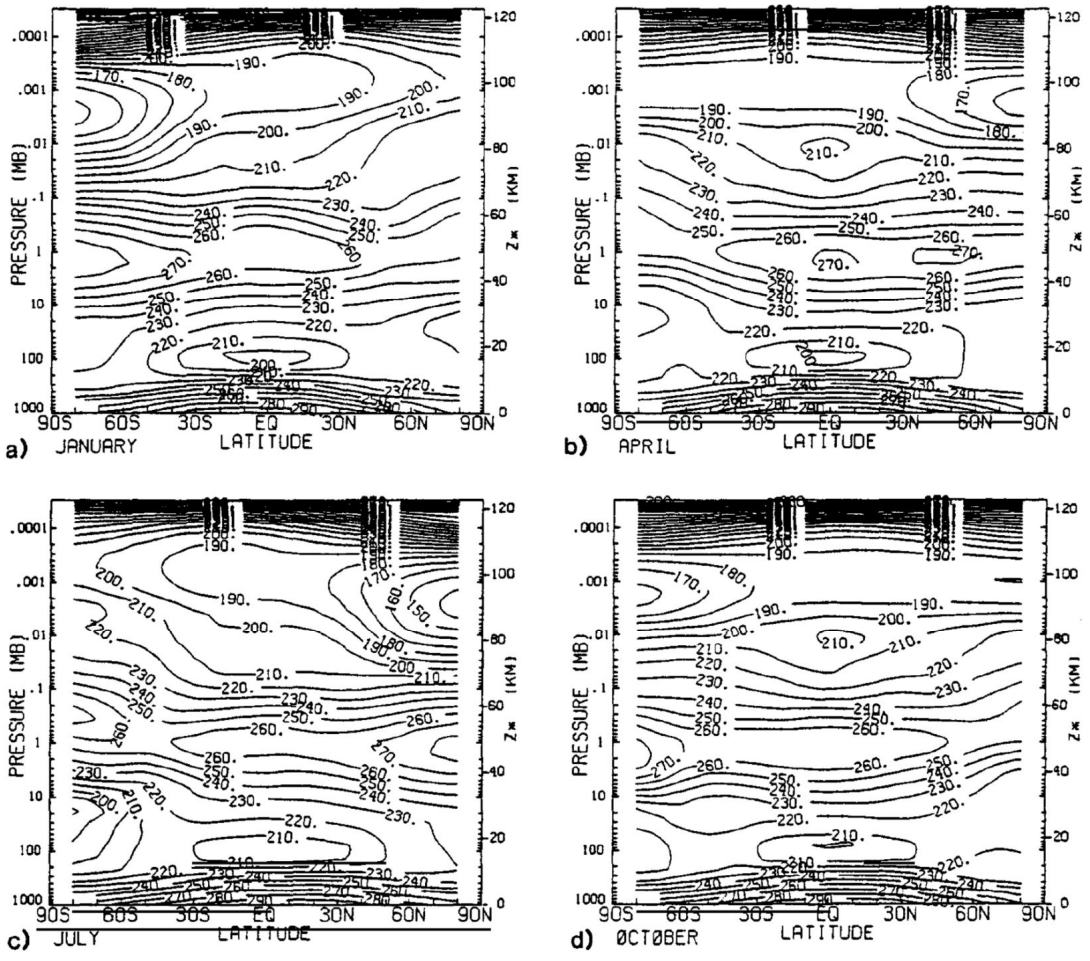

Figure 1-5. Latitude-height cross sections of zonal mean temperature for a) January, b) April, c) July, and d) October from a Climatological model by Chandra et al. [1990]. Contour interval is 10 K.

As described above, wave-driven global circulation plays a dominant role in maintaining the temperature and wind fields in the polar mesopause region. However, auroral precipitation is a possible source of modulation in this region, since high-energy electrons sometimes penetrate down to the mesopause altitude. Intense auroras characterized by vivid pink borders are called Type-B auroras and are often observed when hard auroral precipitation occurs. Figure 1-6 shows an altitude versus wavelength distribution of the intensity of Type-B auroras observed by a sensitive TV camera [Gattinger et al., 1985]. This provides direct evidence that auroral electrons can reach mesopause altitudes.

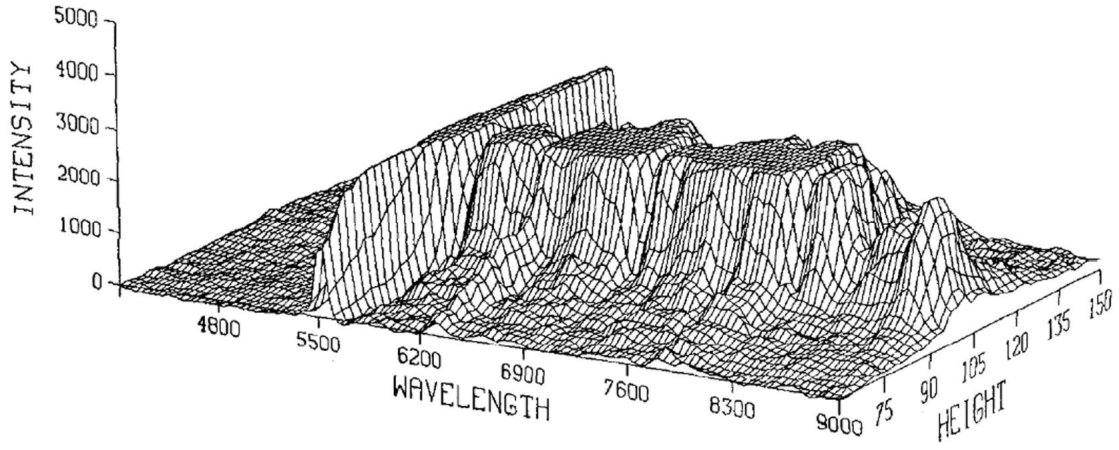

Figure 1-6. Height and wavelength distribution of intensity for Type-B aurora observed by a sensitive TV camera [Gattinger et al., 1985].

As already stated, it is highly possible that auroral precipitations can influence the dynamics of the mesopause region. However, such effects are still not very well understood. In this thesis, a study of the polar mesopause region using remote sensing of OH airglow is presented, focusing on auroral effects.

1-3 Overview of the study of OH airglow

OH airglow is one of the strongest emissions in the night sky. It was first discovered by Meinel in the late 1940's [Meinel, 1950]. The spectral lines of vibration–rotation bands called the Meinel bands ($v' < 9$) appear in the visible to infrared regions. These bands are also useful as source of wavelength and intensity calibrations in astronomy fields [e.g. Oliva and Origlia, 1992]. The mean altitude and thickness of the OH airglow layer have been measured to be 87 and 8 km, respectively, by rocket-borne observations [Baker and Stair, 1988]. The main source of excited OH molecules in that region is the reaction of atomic hydrogen with ozone [Bates and Nicolet, 1950]. The distribution of rotational lines from low rotational quantum number transitions is determined by the Boltzmann distribution with a rotational temperature, T_{rot} [Pendletone et al., 1993]. Thus, the OH rotational temperature derived from the intensity ratio of these rotational lines is considered to be the local kinetic temperature of the emitting region.

OH airglow spectroscopy is a very reliable and useful method for determining the temperature of the upper mesosphere region, and many optical observations have been made not only by ground based but also by a rocket-borne [e.g. Watanabe et al., 1971; Clemesha and Takahashi, 1986], an air-borne [e.g. Pick et al., 1972; Moreels et al., 1973], and aircraft-borne instruments [e.g. Dick et al., 1970; Dodd et al., 1994]. The countless numbers of ground-based OH observations are conducted in previous. For example, Sivjee et al. [1972] performed ground-based and airborne observations of the OH 7-2 and OH 8-3 bands with an Ebert spectrometer consisting of a 1200 grs/mm grating and a cooled photomultiplier tube to study the latitudinal and local time dependence of the OH airglow. Krassovsky [1972] also used a grating spectrometer to observe the OH 4-1 band and investigated nocturnal variations of brightness and rotational temperature in Zvenigorod in Russia (56°N). Takahashi et al. [1974] found

various patterns in the nocturnal variations of temperature and intensity of the OH 8-3 band with a tilting-filter photometer in Brazil (23°S). In addition to them, many optical observations are conducted mainly in low and mid latitudes [e.g. Chamberlain et al. 1959; Fiocco et al., 1970; Peterson and Kieffaber, 1973; Takeuchi et al. 1979; Takahashi et al., 2002; López et al., 2007; Guharay et al. 2008]. As mentioned in the first sentence of this chapter, OH airglow is the strongest emission in the kinds of airglow emissions. Thus two dimensional imaging observations are also conducted since Taylor et al. used a cooled CCD camera equipped with band pass filters and successfully found gravity wave patterns in the airglow layers at the upper atmosphere [Taylor and Hill, 1991]. The numelous imaging observations reveals a presence of the various kinds of gravity waves and horizontal structures in the upper mesosphere and the lower thermosphere [e.g. Hecht et al., 1997; Nakamura et al., 1999; Frey et al., 2000; Yamada et al., 2001; Tang et al.. 2002; Shiokawa et al., 2003; Brown et al., 2004; Onoma et al., 2005; Suzuki et al., 2007, Vadas et al., 2009].

Recently global observations by satellites have revealed detailed characteristics of OH airglows. For example, an exact empirical model of the altitude profile of OH emission has been constructed based on six years of measurements by the Wind Imaging Interferometer (WINDII) onboard the UARS satellite [Liu and Shepherd, 2006]. The WINDII measures volume emission rate profiles of the OH 8-3 band P1(3) line airglow (734 nm) as shown in Figure 1-7 [Liu and Shepherd, 2006]. The altitude resolution of this data is 2 km and the lines plotted with the data points are Gaussian fitted curves. They used 50,000 such profiles collected within ±40° latitudes over the period from November 1991 to August 1997 and found a universal inverse correlation between the altitude of the peak in the profile and the integrated emission rate. They also found a positive correlation between the peak altitude and the intensity of the F10.7 cm solar irradiance flux and included it in their model of OH emission profiles.

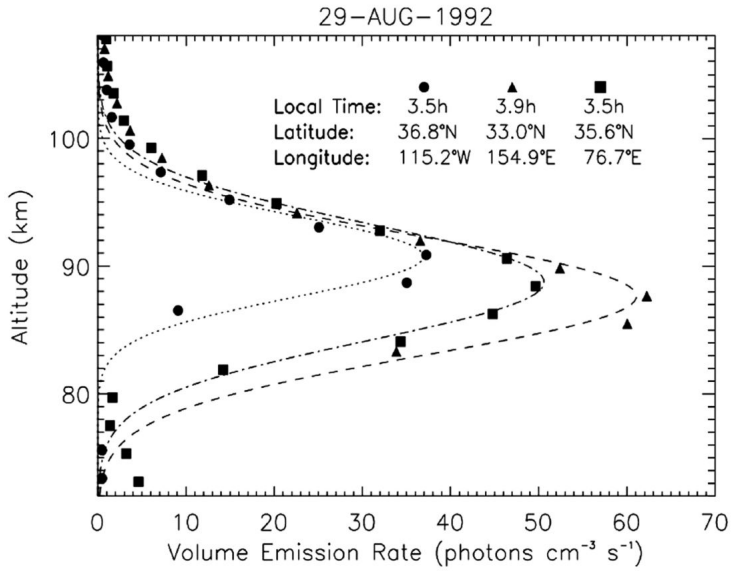

Figure 1-7 Examples of volume emission rate profiles of OH airglow observed by WINDII/UARS [Liu and Shepherd, 2006].

The inverse relationship between peak altitude and intensity of the OH airglow is also verified by the SABER (Sounding of the Atmosphere by Broadband Emission Radiometry) instrument onboard the TIMED (Thermosphere Ionosphere Mesosphere Energetics and Dynamics) satellite (see Russell et al. [1999]) in the polar region. The SABER has ten channels which measure infrared radiation from the atmosphere. Winick et al. [2009] showed relationship between OH layer height and peak volume emission rate over nighttime and latitudes between -60° to +80° during February to March of 2004, 2005, and 2006. These are shown in Figure 1-8. According to their results, the northern high latitude region for 2004 and 2006 was under unusual condition during in 2004 and 2006. The unusual condition means extremely low height of OH emission peak which sometimes descended down to 80 km, and is thought to be related to a major stratospheric warming event. The inverse relationship is still valid even in such extreme cases.

The modulation of OH airglow emission is mainly caused by vertical shift of peak layer height [Marsh et al., 2006]. The major source of vertical motion is atmospheric

tide in the low and middle latitudes. In addition to such modulations a vertical motion accompanied with a downward transportation of O rich air is also a significant source for lowering of OH layer in the polar regions [Mlynczak and Solomon, 1993]. In both cases, the enhancement and lowering of OH airglow occur when downward motion is enhanced. Therefore the universality of inverse relationship between OH layer height and a peak emission is kept. The downward motion causes lowering of OH profile and adiabatic heating of the atmosphere leading to rising of OH rotational temperature. Eight channels of the SABER instruments observe near-global distribution of the infrared emissions from CO_2 to retrieve kinetic temperature profiles of atmosphere from 0 to 100 km in altitude. Figure 1-9 shows a relationship between height of layer peak and rotational temperature at OH peak height shown by Winick et al. [2009]. The inverse relationship between these values is clearly seen. Thus it is obvious that the positive correlation between the rotational temperature and the intensity of OH airglow is expected.

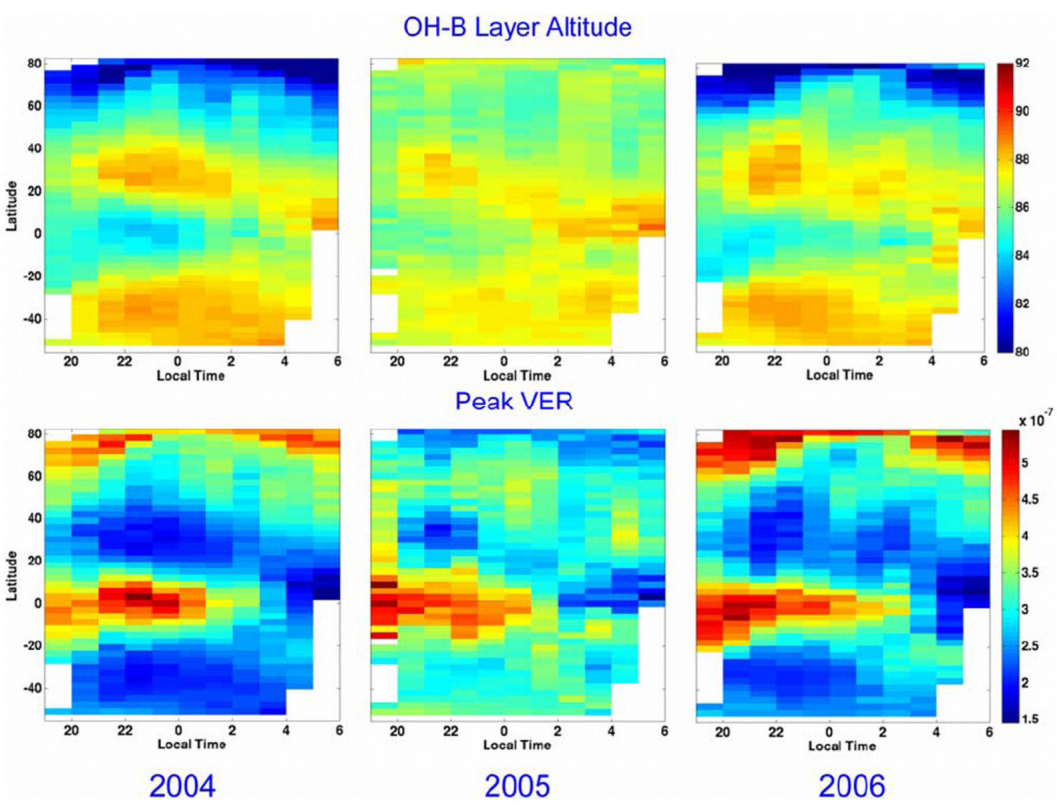

Figure 1-8. Latitude and LT dependences of OH layer altitude (top) and peak volume

emission rates (bottom) observed by SABER for January to March of 2004, 2005, and 2006 [Winick et al., 2009]. The units for the upper and lower panels are in km and photons/m^3/s, respectively.

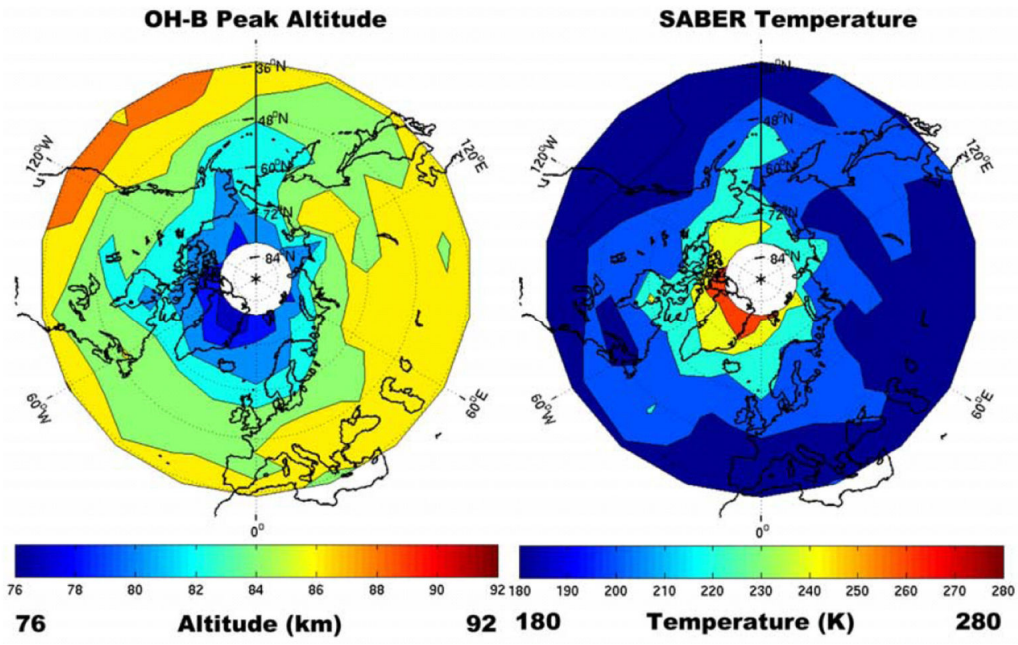

Figure 1-9. Relationship between a rotational temperature at OH peak height and height of layer peak. Data are from 7 to 8 February, 2004, under an unusual condition.[Winick et al., 2009].

The positive correlation between rotational temperature and airglow brightness has already been known through many ground-based observations. This relationship has been found to be valid over all time scales observed (several minutes to annual). An example of such ground-based data is shown in Figure 1-10, from the work of Cho et al. [2006]. This is a scatter plot of temperature versus OH 6-2 emission rate from the SATI (Spectral Airglow Temperature Imager) data obtained at Resolute Bay (74.68°N). The daily mean data from November, 2001 to January, 2005 are plotted here. The winter-time averages are indicated on the data as large circles. It is noteworthy that each winter-time

average point falls on the regression line for the daily data of that particular winter, or that the four regression lines have similar slopes and the winter-time average points roughly align along the average of these slopes. This indicates that the positive correlation between rotational temperature and intensity applies over time scales from days to years.

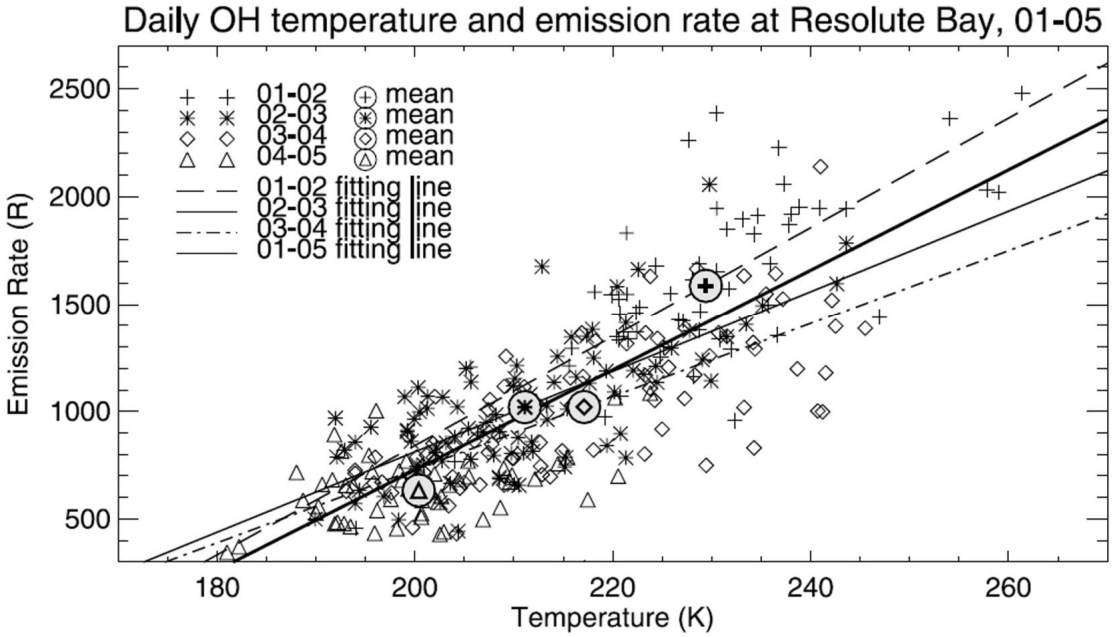

Figure 1-10. The scatter plot of temperature and emission rate of OH 6-2 from the SATI data at Resolute Bay. The daily averaged data from November, 2001 to January, 2005 are presented here. The winter time averages are indicated as large circles [Cho et al., 2006].

A positive correlation is also found between fluctuations in rotational temperature and intensity due to gravity waves passing through an OH layer. However, these are not perfectly in phase since quantities measured on the ground are height integrated through the OH layer. This effect has been modeled by Liu and Swenson [2003]. They modeled perturbations of the OH rotational temperature caused by gravity waves with different vertical wavelengths and damping factors. The damping factor is a ratio representing the damping amplitude rate with altitude. Figure 1-11 shows

unperturbed (thick solid line) and perturbed (thin gray lines) volume emission rates for (a) O_2 and (b) OH, generated by a gravity-wave perturbation with 2% temperature amplitude. The wave amplitude does not change with altitude (damping factor = 1), and the vertical wavelength is 25 km. The gray lines represent waves with 24 different phases, each of which is 15° apart. The bottom axis corresponds to these lines. The thin solid line, which corresponds to the upper axis, is the standard deviation of the perturbed emission with respect to the unperturbed one. This indicates that the largest perturbation of the volume emission rate occurred at an altitude lower than the peak emission altitude. On the other hand, the rotational temperature is equivalent to the temperature averaged over the OH layer with the profile of the OH volume emission rate as a weighting function. This means that the main region that contributes to the amplitude of the perturbation caused by a gravity wave is different between the intensity and the rotational temperature. The phase of most gravity waves propagates downward. Therefore the phase of the perturbation of rotational temperature caused by a gravity wave leads that of intensity. Figure 1-12 shows contour plots of the phase differences between the perturbation of the rotational temperature, $T'_{R,OH}$, and the intensity of OH airglow, I'_{OH} as functions of vertical wavelengths and damping factors. The phase difference between $T'_{R,OH}$ and I'_{OH} is defined as the phase of $T'_{R,OH}$ minus that of I'_{OH}. Thus, a positive phase difference indicates that $T'_{R,OH}$ leads I'_{OH}. The results indicate the phase shift is always positive for typical gravity waves, and ranges from 0 to 40°. This is useful for identifying whether the source of the variation is a gravity wave or some other phenomenon, when the only data available is from a single ground-based observation.

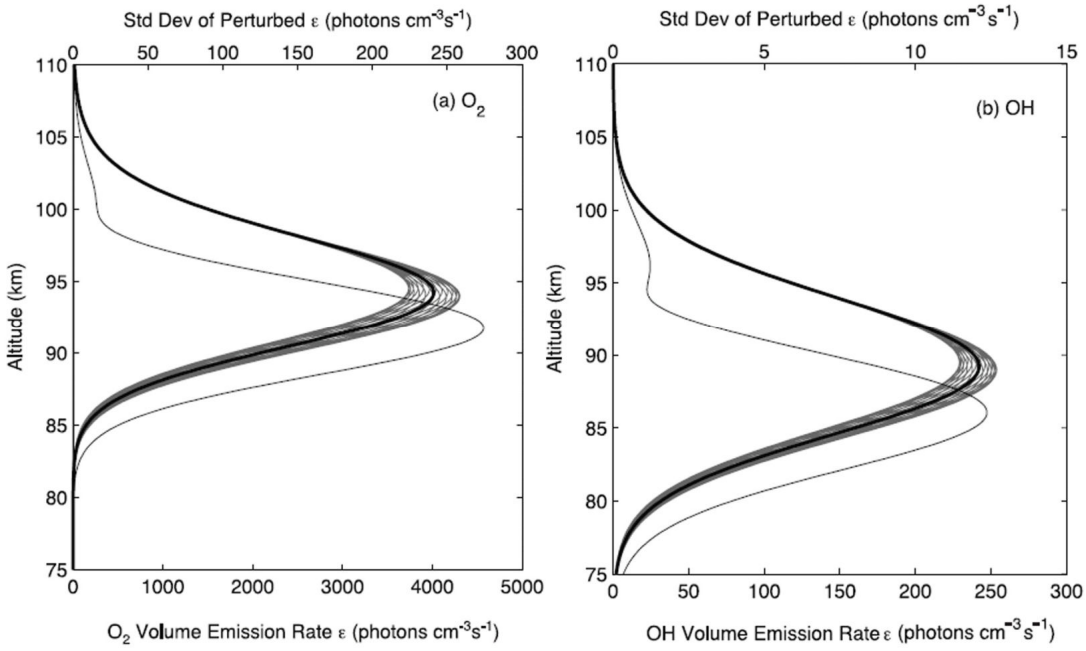

Figure 1-11. Unperturbed (thick solid line) and perturbed (thin gray lines) (a) O_2 and (b) OH volume emission rates, generated by a gravity wave perturbation with 2% temperature amplitude. The wave amplitude does not change with altitude (damping factor = 1) and the vertical wavelength is 25 km. The gray lines represent waves with 24 different phases, each of which is 15° apart. These lines refer to scale on the bottom axis. The thin solid line is the standard deviation of the perturbed emission with respect to the unperturbed one, and refers to the upper axis. These results are from simulations performed by Liu and Swenson [2003].

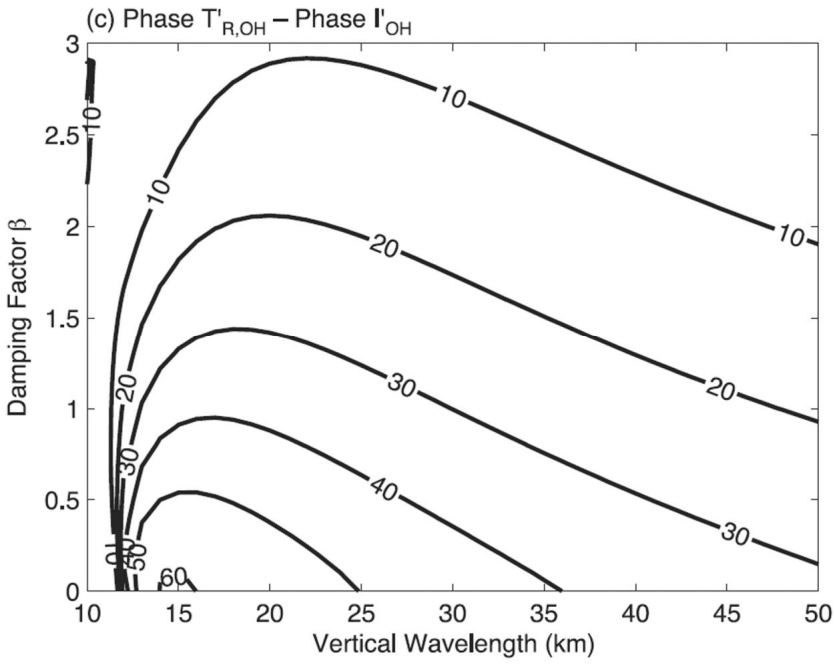

Figure 1-12. Contour plot of the phase differences between rotational temperature perturbation, $T'_{R,OH}$ and intensity of OH airglow, I'_{OH} as functions of vertical wavelengths and damping factors. Phase difference between $T'_{R,OH}$ and I'_{OH} is defined as phase of $T'_{R,OH}$ minus phase of I'_{OH}. Positive phase indicates $T'_{R,OH}$ leads to I'_{OH} [Liu and Swenson, 2003].

As mentioned earlier in this section, the character of the OH airglow has been investigated by combining ground-based and recent satellite observations. However, ground-based observations in the Antarctic polar region in particular are still limited in number. Thus, local effects on the OH airglow due to hard auroral precipitations or solar proton events, for example, are not fully understood. In the next section, the importance of OH airglow observation in the polar region is discussed.

1-4 Study of polar mesopause by remote sensing of OH airglow

Several ground-based OH airglow observations in the polar region were conducted by investigators using various optical instruments. In the northern polar region, Myrabø et al. [1984] reported behaviors of OH8-3 band based on three-winter observations in Poker Flat, Alaska (65°N). Oznovich et al. [1995] used a Michelson interferometer to observe the OH 3-0 band, and a scanning photometer for other airglow emissions (OI 557.7 nm and Na 589.3 nm) to investigate the behavior of atmospheric waves passing through these layers in Eureka in Canada (80°N). Nielsen et al. [2002] reported a long-term variation of the OH rotational temperature, using a 20-year dataset obtained with an Ebert–Fastie scanning spectrometer in Longyearbyen in Norway (78°N). Though OH airglow measurements made in the Antarctic are limited in locations, some important works are also conducted. The first long term observation of the OH rotational temperature that showed seasonal and interannual variations in seven years using a Czerny–Turner scanning spectrometer at Davis Station (68.6°S) was reported by Burns et al. [2002]. French and Burns [2004] reported a seven-year trend of the OH rotational temperature. They found a long-term correlation between temperature and the solar cycle and effects of planetary wave penetration into the upper mesosphere during the winter season. By using the same OH rotational temperature dataset at Davis Station, French et al. [2005] reported unusual high temperature for winter of 2002 and found 14-day oscillation with large amplitude (~15-20K) in early spring related to a planetary wave penetration into the mesopause region. Espy et al. [2003] also found rapid and large scale variation in OH rotational temperature which occurred simultaneously in Rothera Station (68°S, 68°W) and Halley Station (76°S, 27°W). Since the meridional wind variation observed by a medium frequency (MF) radar in Rothera Station showed a very good correlation with the temperature variation during this period, they concluded that the temperature variation was caused by an enhancement of the inter-hemispheric meridional

flow from summer (north) to winter hemisphere (south). Won et al., 2002 showed a spectrum analysis of gravity waves using datasets of rotational temperature by a Michelson interferometer in King Sejong Station (62°S). As mentioned above, the observations of OH airglow conducted in the polar regions in the past were mostly to find the relatively long-term trend of the OH rotational temperature as a climatological study of the mesopause. However, the effects of auroral particles, such as direct energy deposition and Joule heating, on the OH rotational temperature are still not clear.

Stubbs et al. [1983] reported a rise in the OH rotational temperature after auroral particle precipitation. Figure 1-13 shows their results. This plot shows the rotational temperature and intensity of the rotational lines (lower panel) for the OH 8-3 band observed by a scanning photometer during a single night at Mawson Station, Antarctica (67° 36 'S, 62° 53' E). The region enclosed by a broken line corresponds to a period of high auroral activity. As shown in the figure, the intensity data for the OH rotational line during this period suffer from contamination due to auroral emissions and are not used for further temperature estimation. The difference between temperature values before and after the auroral contamination is approximately +40 K. However, the data gap of nearly 5 hours is too long to identify whether the perturbation is induced by atmospheric waves or by the aurora. The other difficulty in interpreting these results is that positively correlated variation is also observed in the intensity of the rotational lines. This positive correlation between rotational temperature and intensity of OH airglow is normal for fluctuations caused by gravity waves or other atmospheric waves (See Figure 1-10). Therefore it is difficult to say that the rise in temperature is caused by auroral precipitation. This type of fluctuation was also observed in the case of an atmospheric tide passing through the OH airglow layer [see Appendix].

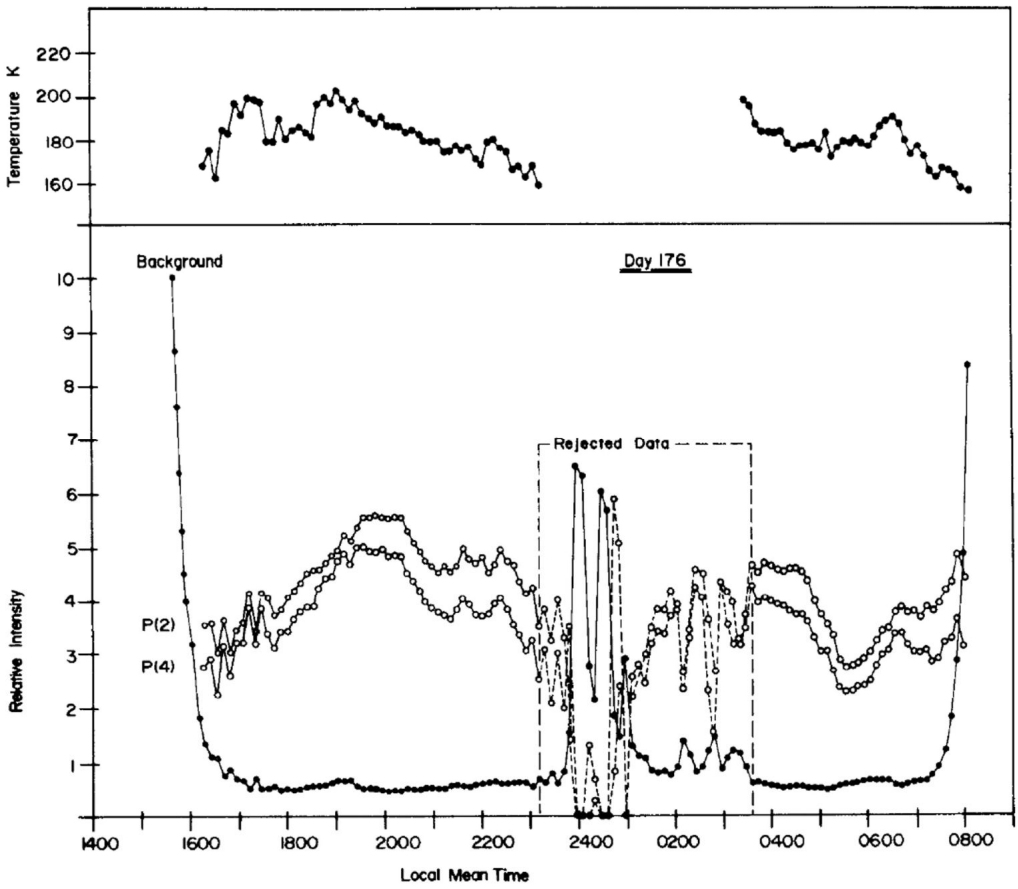

Figure 1-13. Rotational temperature (upper panel) and intensity of the rotational lines (lower panel) of the OH 8-3 band observed by a scanning photometer during a single night at Mawson Station, Antarctica (67° 36'S, 62° 53' E) [Stubbs et al., 1983].

As noted above, spectral overlap of the auroral and airglow emissions makes it difficult to study the relationship between the aurora and airglow by optical methods, since the airglow and auroral emissions can not be completely separated in the spectral dataset. To study long-term variations in the upper mesospheric temperature in Antarctica, and the effects of auroras, we have developed a high-sensitivity spectrometer consisting of a cooled CCD and a transmission grating as described in the next chapter. Spectroscopic observations made with a Czerny–Turner spectrometer covering the wavelength range 350–980 nm show that the OH 8-4 band in the near infrared region (900–986 nm) exhibits the least auroral contamination. Thus, the new spectrometer is specifically designed to observe the OH 8-4 band.

The specifications of the spectrometer and observation results at Syowa Station in Antarctica are presented in the next chapter and the observation results are shown in Chapters 3, 4 and 5.

2 Instrumentation

2-1 Difficulty of optical observation of airglow in auroral zone.

Remote sensing of the OH airglow is important for the study of the dynamics of the mesopause region, as described in Chapter 1. However, in general, precise optical observation of airglows is difficult in the auroral zone because of the existence of brighter emissions from auroras. For example, the characteristic airglow emission from excited atomic oxygen at 557.7 nm (Transition: $^1S \rightarrow {}^1D$) is also a major auroral emission, producing the well-known green light. The typical intensity of the 557.7-nm line from airglow emission is on the order of 10^2 R. On the other hand, the brightest green auroral emissions often reach 10^5 R. Therefore, it is impossible to detect fluctuations in airglow emission without contamination during an active aurora event. This is common for other major airglow emissions. Although sodium (589.3 nm) and hydroxyl (visible to far infrared) emissions are peculiar to airglow, these emissions overlap over most of their spectral range with intense auroral band emissions such as the N_2 and N_2^+ band systems.

The spectrum of the night sky changes drastically in the presence of aurora activity. Figure 2-1 shows spectra from 720 to 970 nm during quiet and active auroral conditions. These spectra were obtained on October 28, 2006 by a grating spectrometer consisting of a cooled CCD and three gratings in turret 1 at the EISCAT (European Incoherent Scatter) radar site, Tromsø (69.58°N, 19.22°E) [Suzuki, 2006]. The spectrometer has an F-number of 4.2 and a focal length of 320 mm. Although the sensitivity and wavelength resolution were not so high, this instrument was able to obtain nightglow spectra over a wide wavelength range (400-970 nm) by changing the gratings. The details of the spectrometer are described in Suzuki et al. [2008].

The upper panel of Figure 2-1 is a spectrum of the night sky under quiet auroral conditions. The term ‘quiet conditions’ means that no visible aurora was present in the field of view of the spectrometer during the exposure period. Many rotational-vibration

bands of the OH airglow are seen and no aurora-related emissions can be recognized. On the other hand, many intense band structures due to auroral emissions such as N_2^+ and N_2 are seen in the spectrum taken under active auroral conditions, as shown in the lower panel of Figure 2-1. Most of the OH bands are overlapped by the more intense auroral emissions. The fluctuations of the airglow are hidden by those of the bright auroral emission. Therefore it is difficult to detect only airglow emissions when an aurora is present in the sky.

Ideally, the target airglow line should not be contaminated by auroral emissions. However, most auroral emissions have a wide band structure as shown in Figure 2-1 and spectrum regions free from auroral emission lines or bands are limited. Thus, a realistic solution is to find a less contaminated spectral region for airglow observations in the auroral zone. Fortunately, the Meinel OH band has many rotational-vibration bands associated with many kinds of transitions.

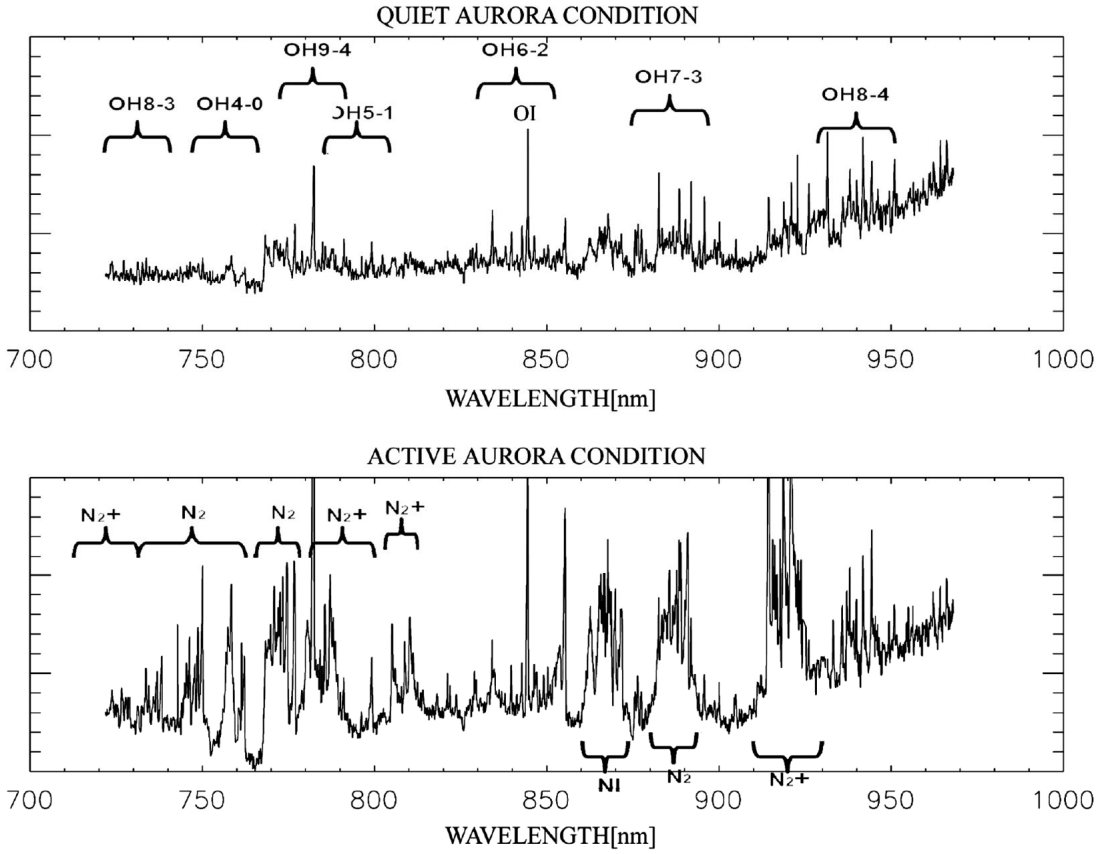

Figure 2-1. The spectra of the night sky between 720 nm and 970 nm under quiet and active auroral conditions. The upper and lower panels are for quiet (upper panel) and active (lower panel) conditions observed at Tromsø, Norway.

2-2 Contamination from auroral emissions to OH bands.

The Meinel bands lie in the visible and infrared regions and correspond to the transitions in the vibrational state. In principle, the rotational temperature can be derived from any vibrational–rotational band. In practice, however, the target band must be selected by considering both the intensity of the band and the degree of contamination from other emissions. Since the main subject of this study is OH airglow in the auroral zone, the target band should contain as little contamination as possible from auroral emission. The OH 7-2 [e.g. Sivjee et al., 1972], OH 8-3 [e.g. Sivjee et al., 1972; Takahashi et al., 1974], and OH 6-2 [e.g. Nielsen et al., 2002; French and Burns, 2004] bands are ones that have been mostly used for investigating mesospheric dynamics. However, the OH 7-2 and OH 8-3 bands are unsuitable for observations in the polar regions because they overlap with intense auroral bands (e.g., Jones, 1971). The OH 6-2 band has been used for observations in the polar region because it is sufficiently intense for detection and it suffers relatively little contamination from auroral emissions (e.g., Nielsen et al., 2002; French and Burns, 2004). Figure 2-2 shows spectra of the OH 6-2 and OH 8-4 bands obtained simultaneously on 3 May 2008 at Syowa Station, Antarctica. The spectrum of the OH 6-2 band was obtained by using a medium-resolution grating spectrometer equipped with a cooled CCD camera. The details of this instrument are described in Suzuki [2008]. The spectra of both bands during active and quiet auroral conditions are shown. Contamination by auroral emissions in the OH 8-4 band is weak even under active auroral conditions, whereas the OH 6-2 band suffers from severe contamination. By comparing spectra obtained under various auroral conditions over the course of the boreal winter of 2006–2007, OH 8-4 was selected as the target band for observations. Therefore the sensitive spectrometer specified to observe OH8-4 band is developed in this study. The details of the instrument are described in the next section.

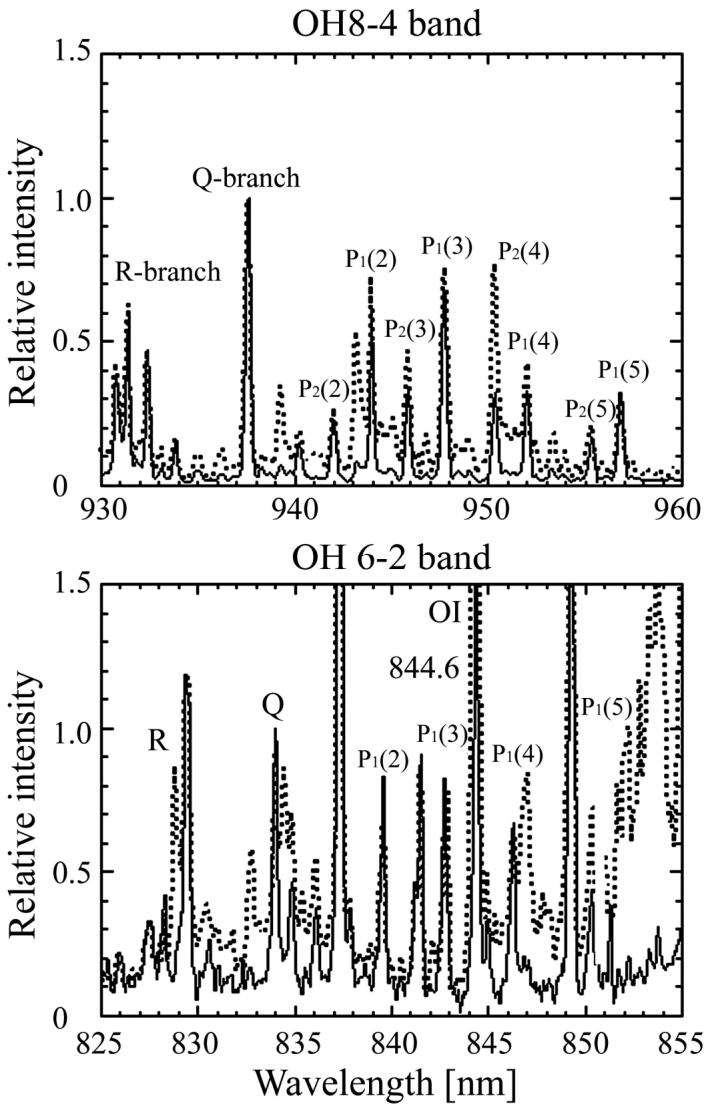

Figure 2-2. Comparison of spectra of the OH 6-2 and OH 8-4 bands obtained simultaneously on 3 May 2008 at Syowa Station. Dotted and solid spectra are obtained at 18:15 UT and 21:57 UT, respectively. The exposure time was 1 min for both spectrometers. Each of the intensities is normalized by the counts of the corresponding Q branch during quiet auroral conditions (18:15 UT).

2-3 The spectrometer for OH8-4 band

The spectrometer consists of an objective lens, a slit, a collimator lens, a plane transmission grating and a CCD camera. The objective lens focuses incident light from the sky on the slit. It has a diameter of 100 mm and a focal length of f = 170mm (F# = 1:7). Slit width can be selected to be 25 μm, 35 μm or 50 μm (corresponding, respectively, to fields of view along the meridian of 0.0084°, 0.0118° and 0.0169°) by varying the position of a plate containing the slits. The length of the slit is fixed so as to limit the field of view to within 4.5° in full angle across the meridian. A slit width of 25 μm is most commonly used in observations. The slit plate also contains a 13 μm diameter pinhole, corresponding to a single pixel of the CCD. It is used to adjust the focus of the optical system by projecting its image onto the focal plane.

Figure 2-3 shows the widths and positions of the slits on the slit plate. A long-pass filter is set in front of the slit to eliminate light from second-order diffractions. Figure 2-4 shows the transmittance of the long-pass filter. The light from the slit is collimated and passes onto the grating with an incident angle of 10°. The groove frequency of the grating is 600 grooves / mm, and the blaze angle is 34°. The light diffracted by the grating is focused onto the cooled CCD image sensor. A mechanical shutter is placed in front of the detector. The arrangement and dimensions of the optical system are illustrated in Figure 2-5. A hood in front of the objective system prevents light from outside the field of view from entering the objective lens. The spectrometer is oriented such that the center of the field of view points to the local magnetic zenith, with a zenith angle of 28:5°. This lets data obtained by using the auroral observation instruments at Syowa Station (such as an all-sky imager and a scanning photometer) be directly compared with the OH airglow intensity and rotational temperature. The cooled CCD image sensor has 1024 × 1024 pixels and each pixel has dimensions of 13 μm×13 μm. Its sensitivity in the near-infrared region is enhanced, and etaloning is suppressed.

The pixel size is nearly half the width of the projected image of the 25 μm slit on the image sensor. The CCD head is attached to the end of the optical system and aligned so that the dispersion and spatial directions correspond to the columns and rows of the CCD, respectively. The CCD is cooled to −70°C by a thermoelectric cooler to reduce thermal noise.

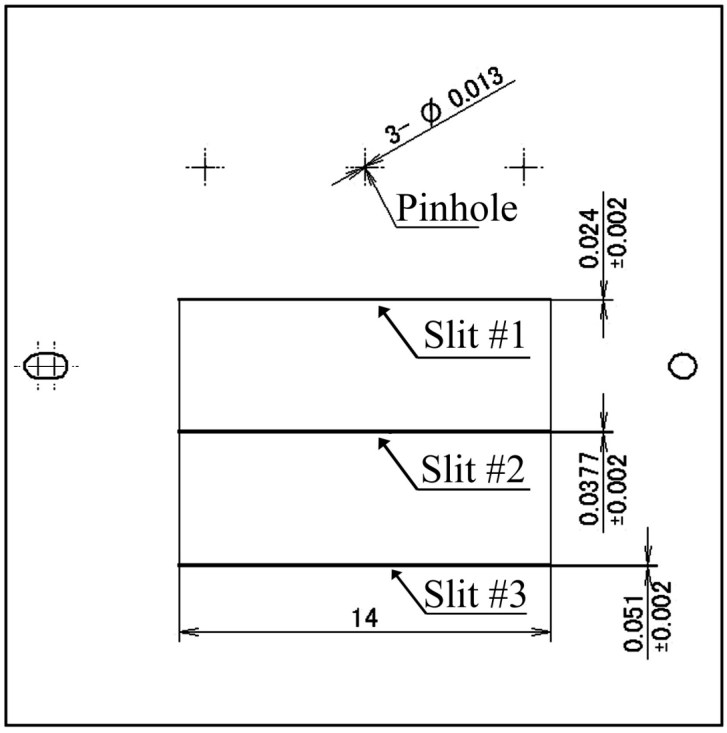

Figure 2-3. Width and position of the slits on the slit plate.

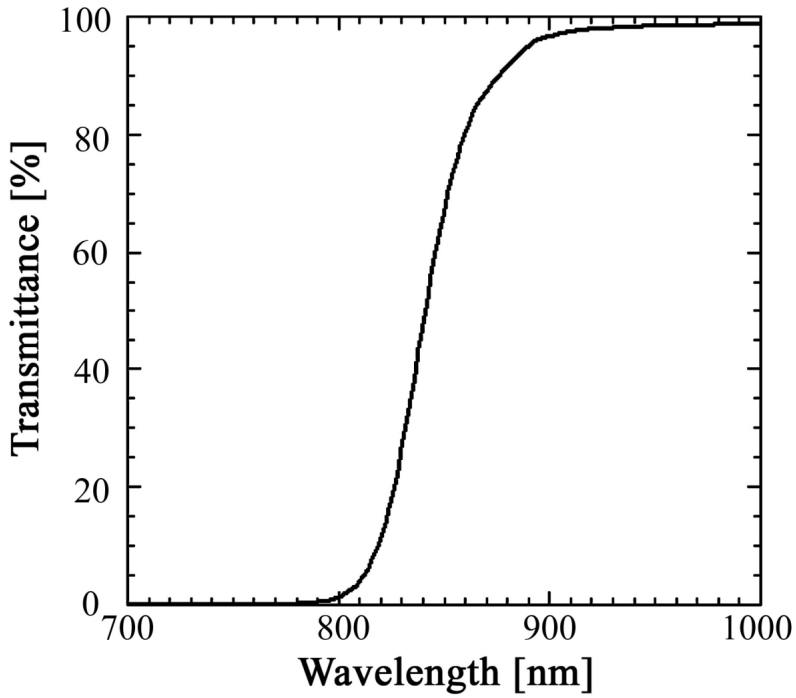

Figure 2-4. Transmittance of the long-pass filter to cut second-order diffraction.

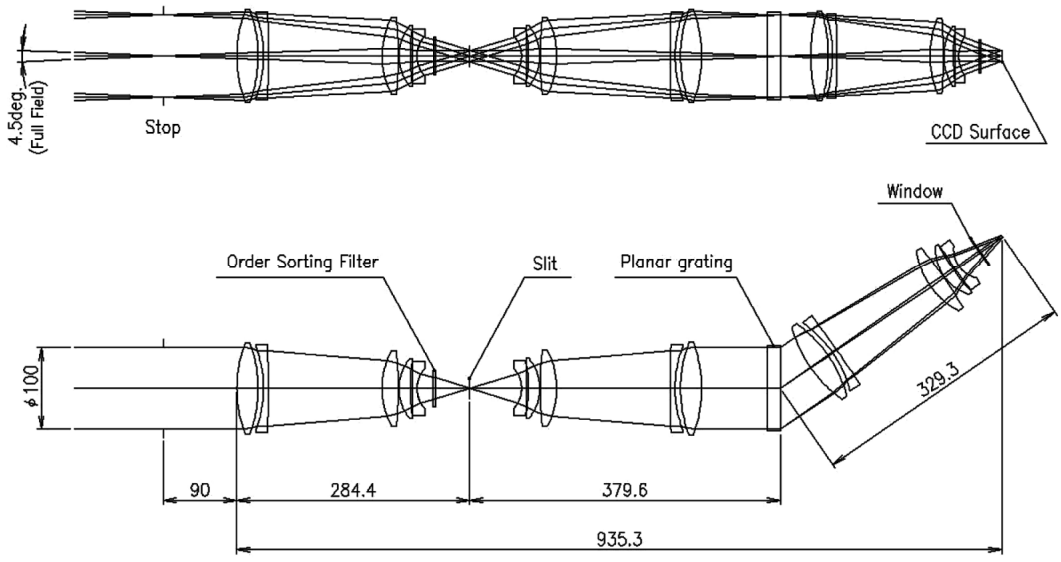

Figure 2-5. Optical system of the spectrometer.

2-4 Calibration of the spectrometer

Calibration to determine the sensitivity and the dispersion of the spectrometer was performed using an integrating sphere light source at the National Institute of Polar Research, Japan. The integrating sphere has a diameter of 1.8 m and emits light from an inner light source to the ideal plane of uniform emission.

First, a neon lamp was used as the light source to determine the line dispersion on the CCD elements. Figure 2-6 shows the raw image obtained by the spectrometer with the slit of 25 μm. Hereafter, the position of each element is defined by two address numbers, $0 \leq X$ and $Y \leq 1023$. The X direction corresponds to wavelength (dispersion) and the Y direction corresponds to the angle in the field-of-view. A spectrum is obtained by summing the counts of each column along the Y direction. However, a simple summation along a column gives an asymmetric shape of the spectral line and degradation in the wavelength resolution, because each projected line slightly curves as a result of differences in the incident angle to the grating, as can be seen in

Figure 2-6.

To correct this effect and realize the highest resolution, counts along the curve must be summed. Figure 2-7 shows the amount of position shift of a spectrum to the center of the field-of-view versus Y. To ensure these peaks have the same X position, each element of raw data is shifted in the –X direction by a quantity determined by its Y position (see Figure 2-8). The maximum amount of shift is 11 pixels at a raw number of Y = 1023. Therefore, after this correction the image becomes slightly smaller in size, 1013×1024 pixels. Figure 2-9 shows the spectrum of the neon lamp obtained by summing the counts of the image. The positions of two emission lines at 930.1 nm and 953.4 nm fall at pixel numbers X = 345 and 617, respectively, yielding a spectral dispersion of 0.0857 nm/pixel.

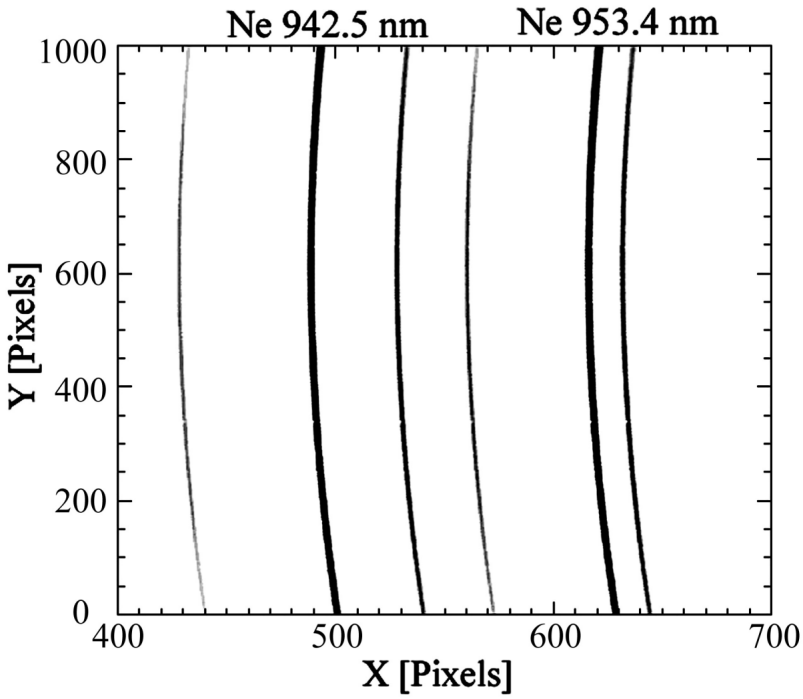

Figure 2-6. Raw spectral image of the neon lamp.

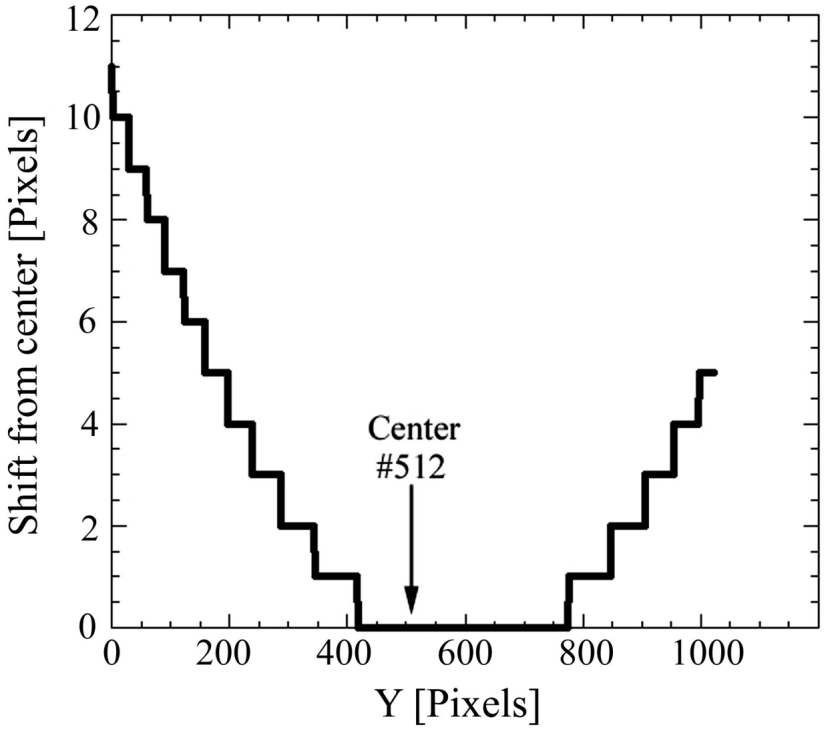

Figure 2-7. Position shift of a spectrum versus Y position.

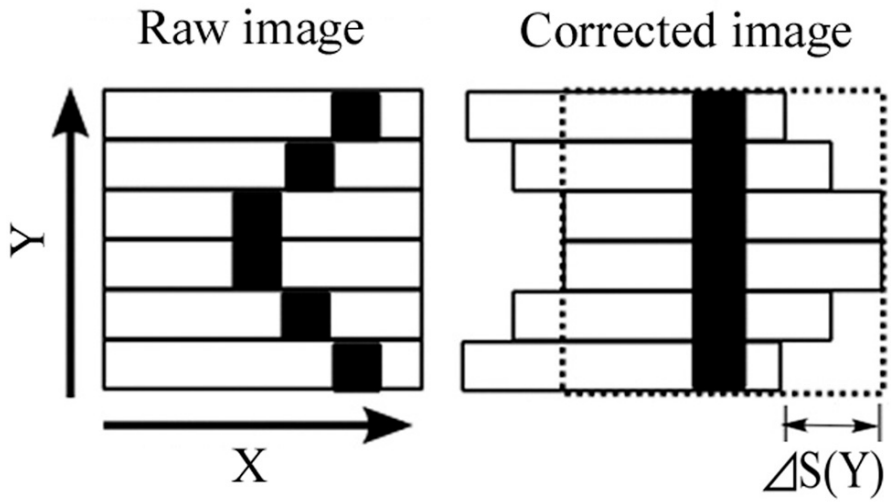

Figure 2-8. Concept of the spectral shift correction.

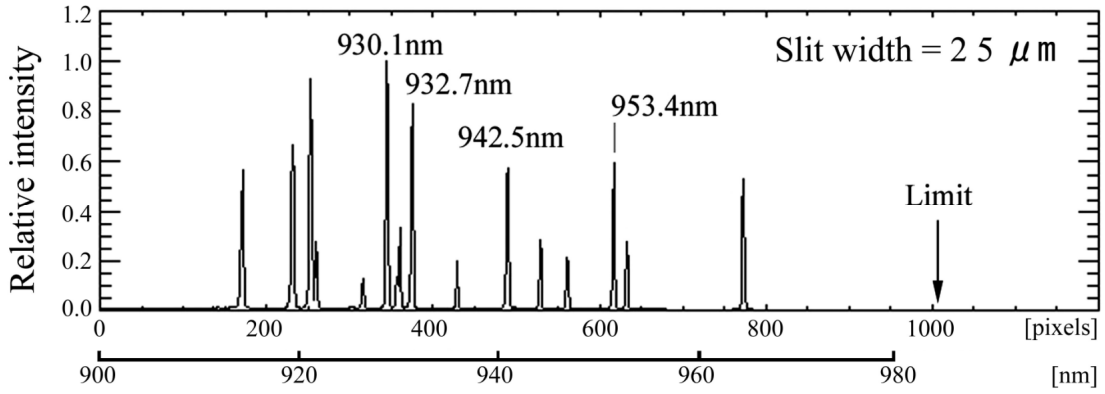

Figure 2-9. Spectrum of the neon lamp extracted from the corrected image.

The observed spectral shape $F_{obs}(\lambda)$ is represented by a convolution of the instrumental function $F(\lambda)$ and the original shape of the emission $S(\lambda)$, as follows

$$F_{obs}(\lambda) = \int_{-\infty}^{+\infty} F(\lambda - \lambda') \cdot S(\lambda')\, d\lambda' \tag{1}$$

The kinetic motion of an OH molecule under a typical mesopause temperature of ~200 K gives a Doppler width of < 0.0001 nm. This value is sufficiently small compared with the line dispersion of the spectrometer of 0.0857 nm/pixel. Therefore, if the original

shape of emitting line is a singlet, the natural shape can be represented by the delta function:

$$S(\lambda) = \delta(\lambda - \lambda_0) \tag{2}$$

where λ_0 is the center position of the spectral line. By substituting this expression into Equation (1) we obtain

$$F_{obs}(\lambda) = F(\lambda - \lambda_0) \tag{3}$$

This means that the observed line shape can be regarded as the instrumental function shape of the spectrometer if natural shape is a singlet. Figure 2-10 shows the instrumental function of the spectrometer for a slit width of 25 μm. The FWHM of the instrumental function is 0.23 nm. Since the spectral intervals of the rotational lines in the OH 8-4 band are larger than 1.7 nm, the resolution is sufficient to resolve these lines. However, in general the original shape of the each rotational lines are not singlet but having doublet structure, because of energy level perturbation caused by interaction between the electronic orbital motion and the rotation of the nucleus called lambda-type splitting. This effect is the order of 0.1 – 1 cm^{-1} [Kendall, 1979] corresponding to ≤ 1 pixel on the CCD. Thus, a width of instrumental function is treated as one of the fitting parameter in temperature analysis. This experiment shows no severe Rowland ghosting around singlet spectrum lines of the neon lamp. Their intensity is confirmed enough less than 1 % to intensity of the main line.

Second, a halogen tungsten lamp was used as the light source of the integrating sphere to measure the sensitivity of the spectrometer. The counts of the spectrum at x pixel, $I(x)$ [counts/pixel], obtained by exposing the integrating sphere, is represented as

$$I(x) = \tau(S(x)L(x) + D) + I_0 \tag{4}$$

where $S(x)$ is the sensitivity of the spectrometer in the units of [counts/pixel/sec]/[R/nm], τ is the exposure time, L is luminosity of the light source [R/nm] and D is the dark count. Thus $S(x)$ can be written as

$$S(x)=\left(\frac{I(x)+I_0}{\tau}-D\right)\Big/L(x) \tag{5}$$

Figure 2-11 shows the relative sensitivity of the spectrometer obtained by experiment and by using this relationship. The uncertainty of the relative sensitivity is less than 1%. The spectral dependence of the sensitivity mainly results from the quantum efficiency of the CCD image sensor.

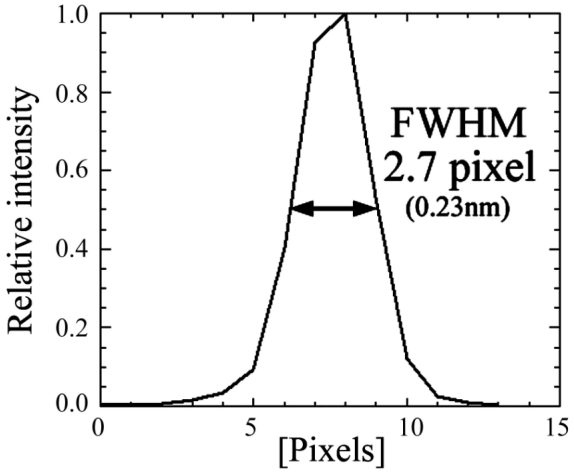

Figure 2-10. Instrumental function of the spectrometer.

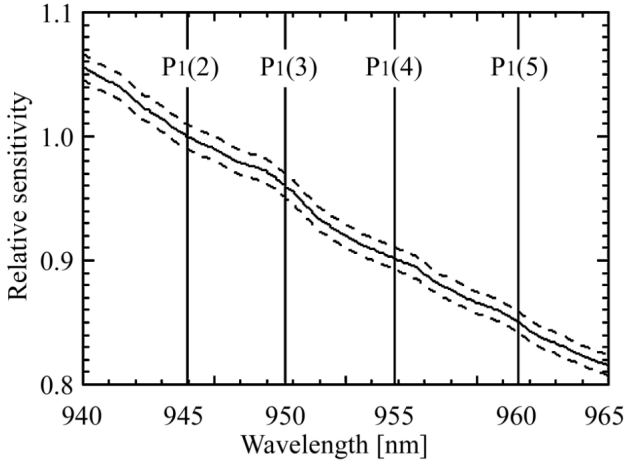

Figure 2-11. Relative sensitivity of the spectrometer. The sensitivity at position of rotational line P1(2) (944nm) is assumed to be 1. The uncertainty is estimated less than ±1% order and shown by dotted line.

2-5 Installation of the spectrometer at Syowa Station

The spectrometer was installed at Syowa Station, Antarctica (69°S, 39°E) by the 49th Japanese Antarctic Research Expedition (JARE49), and observations were begun on February 29, 2008. The spectrometer and the computer to control the CCD and shutter were installed in a dark room with a skylight window. The skylight window is tilted by 28.5° from the zenith to point in the magnetic zenith direction. The window glass is kept at room temperature by a thermostat-controlled heater set in front of the roof to prevent condensation induced by the extremely low outside temperatures.

Optical adjustments such as focusing are made by inserting shims and only need to be carried out once, just before the first observational season. The spectrometer itself has no movable parts for focus adjustment, which makes it a maintenance-free system for stable operation. Photographs of the skylight and the spectrometer are shown in Figure 2-12 and Figure 2-13, respectively.

Figure 2-12. Skylight set on the roof of the optical building at Syowa Station. The window is tilted to direct the field of view of the spectrometer to the magnetic zenith.

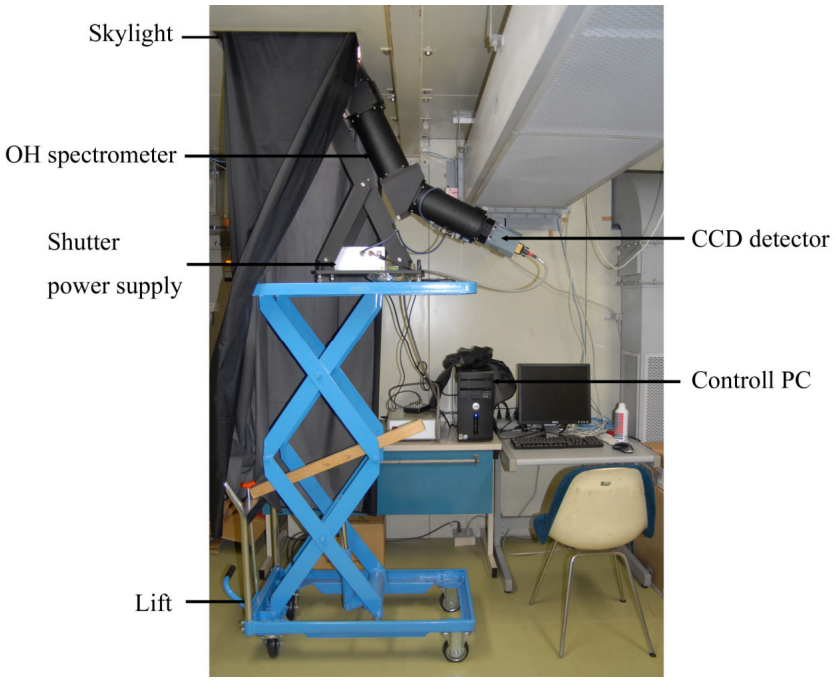

Figure 2-13. OH spectrometer system installed at Syowa Station.

2-6 Other optical instruments at Syowa Station

There are many kinds of optical instruments at Syowa Station, and the data obtained using some of them are also used in this study. In particular, information from the all-sky imager is essential to determine the spatial distribution of auroras and airglows. Overviews of these instruments are given below.

[1] All-sky Television camera (ATV)

The ATV (all-sky television camera) is a panchromatic all-sky TV camera recording aurora morphology at 30 frames/sec. The field of view covers the entire sky using a fish-eye lens (Nikkor f=8 mm / F#=2.8). A high-voltage image intensifier (I.I.) is used to enhance the faint signals from the sky. The ATV is installed in an optical dome on the building next to the optical building where the OH spectrometer is installed. This instrument can record rapid variations of auroral intensity (e.g., flickering), changes in

shape and auroral movement at a high sampling rate.

[2] Color Digital Camera (CDC)

The CDC (Color Digital Camera) is a single lens reflex digital camera for general use (Canon EOS 1Ds MarkII) attached to the all-sky lens (Nikkor f=8 mm / F#=2.8). This instrument was originally installed for a study of the morphology of visible aurora. It is placed in the optical dome next to the ATV and operated with exposure times of 20 sec at 30 sec intervals during the winter nighttime. The camera can record the spatial and color distribution of the visible aurora with a very high spatial resolution.

[3] All sky imager (ASI)

The ASI (All sky imager) is a sensitive camera equipped with a cooled CCD sensor, a very bright fish-eye lens (f=6 mm, F#=1.4) and three band-pass filters set in a turret. The center wavelengths of the transmittance of the band-pass filters are 557.7 nm (OI emission), 630.0 nm (OI emission), and 427.8 nm (N_2^+ emission). Usually the filters are changed every 20 sec by a rotating turret and the exposure time for each acquisition is set to 2 sec. The order of rotation is 557.7, 630.0, and 427.8 nm. Exposures begin every 00, 20, and 40 sec during each minute. This instrument can obtain a snapshot of the shape and spatial distribution of the aurora emission from the three different lines. This data can be used to determine the average energy of the precipitation of electrons during an auroral event. From the ratio of the luminosity of the different lines, the characteristics of auroral particles can be well determined. Details of the ASI are described in Okada et al. [1997].

3 Observations

3-1 Data analysis

Figure 3-1 shows an example of the OH 8-4 band spectra obtained with 1-minute exposure. These spectra are obtained by using the method of correction described in section 2-4. The upper (a) and lower (b) spectra were obtained at 17:00 UT on 8 May 2008 and 1:00 UT on 9 May 2008, respectively, and represent spectra obtained under quiet and active auroral conditions, respectively. A remarkable difference between Figure 3-1(a) and (b) is the presence in (b) of the N_2^+ (1-0) band emission around 920 nm and N_2 first positive (4-4) band emission around 944 nm from the aurora. The N_2^+ (1-0) emission is useful as a measure of the auroral activity. The N_2 first positive (4-4) band emission partially overlaps a rotational line of the OH 8-4 band. However, the contamination from the aurora emission is so weak that it is possible to distinguish the rotational line even when a strong aurora is seen in the field-of-view.

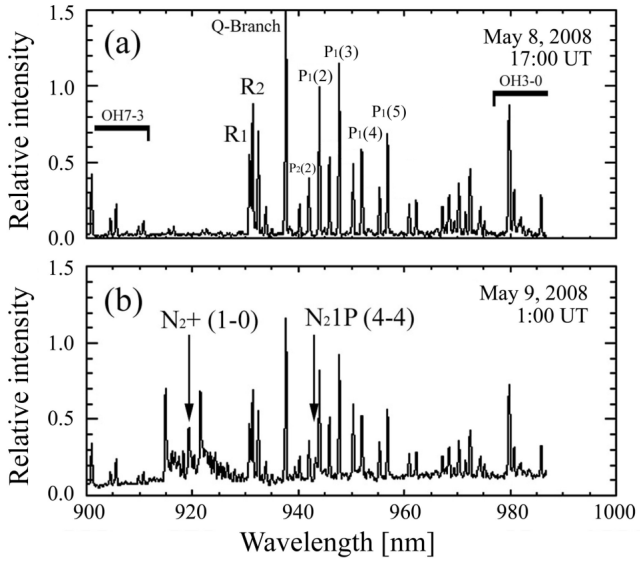

Figure 3-1. Example spectra of the OH 8-4 band obtained with 1-minute exposure. These spectra were obtained by using the method of correction described in section 2-4. The upper (a) and lower (b) spectra were obtained at 17:00 UT on 8 May 2008 and 1:00 UT on 9 May 2008, respectively.

The intensity of the rotational lines and the background value are derived by fitting the instrumental function shown in Figure 2-10 to the observed spectra. The parameters of least square fitting are intensity of rotational line, an inclination and counts of the background, and width of the instrumental function to consider the lamda-splitting of rotational lines. The fitting concept of this analysis are shown in Figure 3-2. According to [Mies, 1974], the emission rate of each rotational line of the OH band is represented as

$$I(J', i', v' \rightarrow J'', i'', v'') = N_{v'} \overline{A}(J', i', v' \rightarrow J'', i'', v'') \frac{2(2J'+1)}{Q_{v'}(T_{rot})} \exp\left[-\frac{E_{i'v'}(J')}{k_B T_{rot}} \right] \quad (6)$$

where J, i and v are the quantum numbers of the rotational, doublet and vibrational states, respectively, N_v is the concentration of OH molecules in the vibrational state v, $Q(T_{rot})$ is a partition function, T_{rot} is the rotational temperature, $E(J)$ is the rotational energy term, k_B is the Boltzmann constant and A is the Einstein coefficient. Therefore, the intensity ratio of two different rotational lines belonging to same rotational–vibrational band is

$$\frac{I_1}{I_2} = \frac{\overline{A}_1}{\overline{A}_2} \frac{2J_1'+1}{2J_2'+1} \exp\left[\frac{E_2 - E_1}{k_B T_{rot}} \right]. \quad (7)$$

Then, the rotational temperature is represented as

$$T_{rot} = \frac{E_2 - E_1}{k_B \log\left[\frac{I_1 \overline{A}_2 (2J_2^{'}+1)}{I_2 \overline{A}_1 (2J_1^{'}+1)} \right]}. \quad (8)$$

It is obvious from this relation that the sensitivity of the rotational temperature to the intensity ratio depends on the choice of the combination of two rotational lines. Figure 3-3 shows the relationship between the rotational temperature and the ratio of the rotational lines of the OH 8-4 band calculated with Equation (8) and the Einstein coefficients given in Reference [Langhoff et al., 1986]. The intensity ratio of the rotational lines $I(P_1(2))/I(P_1(5))$ is most sensitive to fluctuation of the rotational

temperature at a typical temperature of the mesopause region. Therefore, this combination is most commonly used to derive the rotational temperature in this work. The ratio of $P_1(3)$ and $P_1(5)$ is also used to validate the derived temperature. More precisely, deviation between the rotational temperature derived from ratio of $I(P_1(2))/I(P_1(5))$ (T_{25}) and $I(P_1(3))/I(P_1(5))$ (T_{35}) is used to examine the accuracy of the fitting. In this work, the data points that satisfy $|T_{25}-T_{35}| > 5$ are discarded. This criterion sorts the severely contaminated data by strong aurora emission or numerous absorption lines of water vapor rising with scattered continuum emission from Moon or Sun light. The rotational line $P_1(4)$ is not used for temperature derivation because of severe absorption by water vapor in the atmosphere. There exists a strong absorption line next to $P_1(4)$ line with an interval of only 0.053 nm [Giver, 1982].

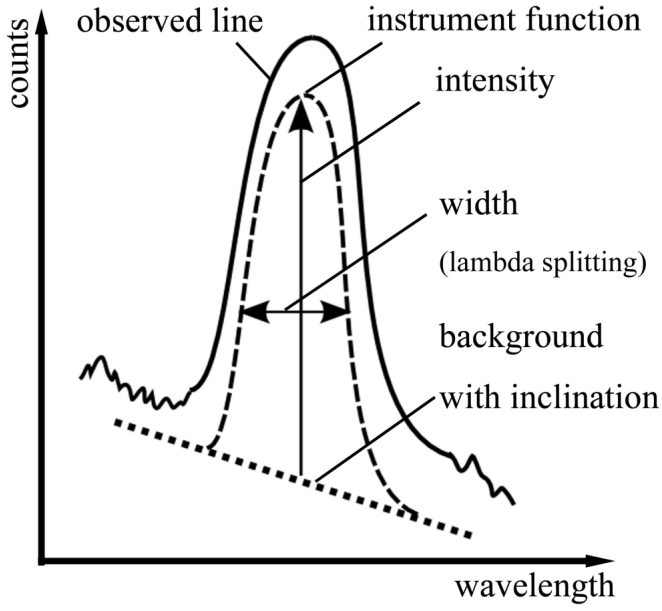

Figure 3-2. Fitting parameters used to determine the intensity of rotational lines

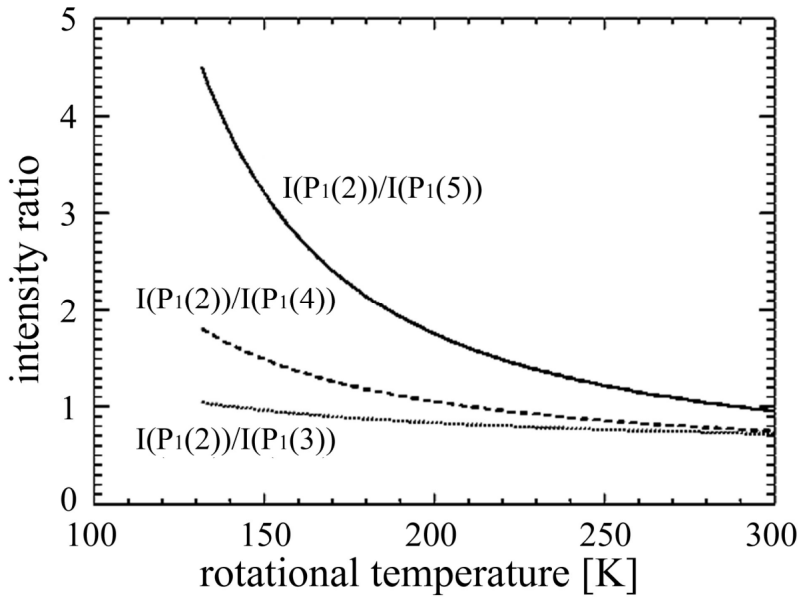

Figure 3-3. Relationship between the rotational temperature and the ratio of the rotational lines of the OH 8-4 band.

The temperature dependence of the intensity ratio becomes less significant with increasing temperature as shown in Figure 3-3. It leads to a larger estimation error for a high temperature by random noise such as the dark noises. The standard error of derived rotational temperature caused by the random noises in the case of typical signal to noise ratio obtained with 1 minute exposure are listed in Table 3-1.

Table 3-1. Standard deviation of the derived rotational temperature caused by random noises with the typical signal to noise ratio (S/N = 100) for 1 minute exposure.

Rotational temperature [K]	150	200	250
Standard error [K]	± 1.9	± 2.1	± 2.5

3-2 Summary of the OH observation at Syowa Station in the austral winter season in 2008.

The spectrometer was installed at Syowa Station by 49th Japanese Antarctic Research Expedition in early February, 2008. The observation was made between 29th of February and 18th of October, 2008. This period corresponded to the period from early autumn to the late spring, when the dark night existed. The observation time of the each night was determined by a solar zenith angle. In principle, the observations were conducted when a solar elevation angel was less than 18° (astronomical twilights). The exposure time was set to 1 minute through the whole season in 2008. The sequence of the observation was as follows; 1, Setting number of the images to be taken in the control program, 2, executing start of the observation, 3, the program records a CCD image with the shutter closed. (Acquiring dark image.), 4, the program starts to record the CCD images with shutter opened, and 5, the program stops observation when the number of shots reaches the specified value. The sequences after 3 are performed automatically by the program. Though the observation over the one night was operated automatically by the control PC, it had to be decided manually whether the observation should be conducted or not. In operation of the 2008, the observations were conducted over 158 nights including even cloudy days except under extremely bad weather such as blizzard or heavy snow. Of all the observed nights, 59 nights were perfectly clear, 57 nights were partly clear, and the others were perfectly cloudy. The weather conditions for the nights in 2008 are summarized in Table 3-2.

Table 3-2. The weather conditions for nights in 2008. The meanings of the each symbol are ; ○:Clear, △:Partially clear, ×:Cloudy, -: No observation.

day	Feb	Mar	Apr	May	Jun	Jul	Aug	Sep	Oct
1	-	×	△	△	○	-	△	△	-
2	-	-	-	○	○	△	○	△	×
3	-	×	△	○	△	○	○	○	△
4	-	○	△	○	×	×	○	×	○
5	-	△	-	○	○	-	△	-	-
6	-	-	-	○	○	-	○	-	△
7	-	○	-	○	△	○	○	△	○
8	-	△	-	△	-	△	○	○	○
9	-	△	○	△	△	△	△	×	○
10	-	-	△	○	△	○	○	×	△
11	-	×	△	○	△	△	-	-	×
12	-	-	×	△	-	×	-	-	○
13	-	×	×	△	-	-	-	×	△
14	-	-	○	×	○	△	△	△	○
15	-	-	△	-	-	○	-	-	○
16	-	△	-	-	-	×	-	-	○
17	-	×	×	-	×	-	-	△	○
18	-	-	-	-	-	○	○	○	○
19	-	-	-	-	-	×	△	×	-
20	-	-	-	△	△	-	-	△	-
21	-	○	-	-	△	-	-	○	-
22	-	×	×	-	△	-	×	-	-
23	-	○	×	×	-	×	○	-	-

Table 3-2. continued.

24	-	×	△	△	△	×	△	-	-
25	-	-	○	-	-	-	○	-	-
26	-	×	×	×	△	-	-	○	-
27	-	○	-	×	△	-	×	-	-
28	×	△	×	×	○	×	○	-	-
29	△	×	△	△	○	×	○	×	-
30		-	△	○	×	○	○	△	-
31		○		△		△	-		-

4 Temperature variations due to dynamical effects

4-1 Seasonal variation of rotational temperature

From the one spectrum data as shown in Figure 3-1, the OH rotational temperature and intensity of the each rotational line of the OH 8-4 band, and intensity of the auroral N2+ band emission can be derived by the fitting method described in section 3-1. Figure 4-1 shows local time and seasonal dependence of the intensity of the auroral N_2^+(1-0) band emission (left panel), intensity of the Q-branch (center panel), and rotational temperature of OH 8-4 band (right panel) observed in the austral winter season of 2008. The characteristic shape of the contour map is due to the difference of the observation time. The longest observation period was performed around midwinter when longest continuous observation over 16 hours is possible. The data-missing gaps shown in aurora and OH intensity between days of year from 60 to 108 (9^{th} of Feb to 17^{th} of April) are due to an inappropriate setting of the observation. During this period, the gain for each acquisition was set as automatic. Thus the variable sensitivity for each image made it impossible to determine absolute intensity. However the rotational temperature can be derived even in such cases as shown in Figure 4-1, because only relative intensity is needed for it.

The aurora activity is clearly high after midnight while the intensity of the OH and the rotational temperature have no such clear local time dependence. There seems no obvious correlation between aurora brightness and OH intensity or rotational temperature. This fact is consistent with previous works (e.g. Harrison [1970]; Sigernes et al. [2003]) Phenomena with a shorter periodicity that might related to aurora activity are described in Chapter 5. Another remarkable feature is a large day-to-day variability of the OH airglow intensity and rotational temperature. In particular, a significant enhancement of the intensity of the OH airglow and rotational temperature is seen during days of year from

120 to 130. The detailed analysis and discussions for this event are described in the next section.

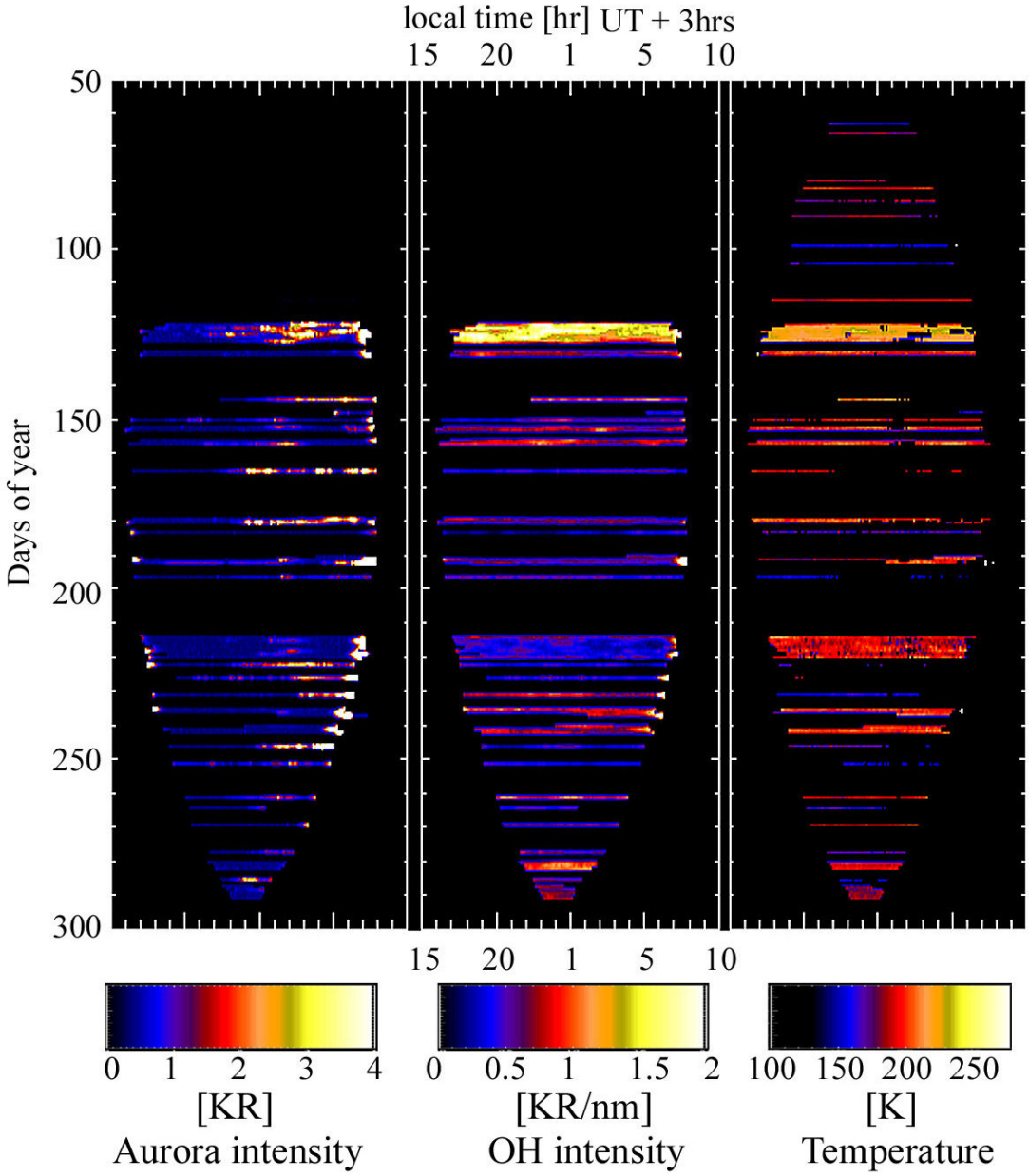

Figure 4-1. Local time and seasonal dependence of the intensity of the auroral N_2^+(1-0) band emission (left panel), intensity of the Q-branch (center panel), and rotational temperature of OH8-4 band (right panel).

Figure 4-2 shows the seasonal variation of the daily averaged OH rotational temperature over Syowa Station in 2008. The error bar shows standard deviation of the fluctuation during each night. The solid blue line over-plotted together with OH temperature is atmospheric temperature at 87 km height over Syowa Station (69°S, 39°E) from the atmospheric empirical model MSISE-90 (Mass-Spectrometer, Incoherent-Scatter Extended). The details of the model are described in Hedin [1991]. The absolute values of the rotational temperature are roughly consistent with MSISE model. The seasonal variation shown in both data, high in winter and low in summer, is a typical variation at the polar mesopause height (~90-100km). This typical seasonal variation is similar to the result of the previous ground OH observation conducted by French and Burns [2003]. They reported seasonal variations in 6 years (1995-2000) of the OH rotational temperature at Davis Station (69°S, 78°E), Antarctica. Davis Station is located at almost the same latitude with Syowa. Thus the similarities of the seasonal behavior of the OH rotational temperature are expected.

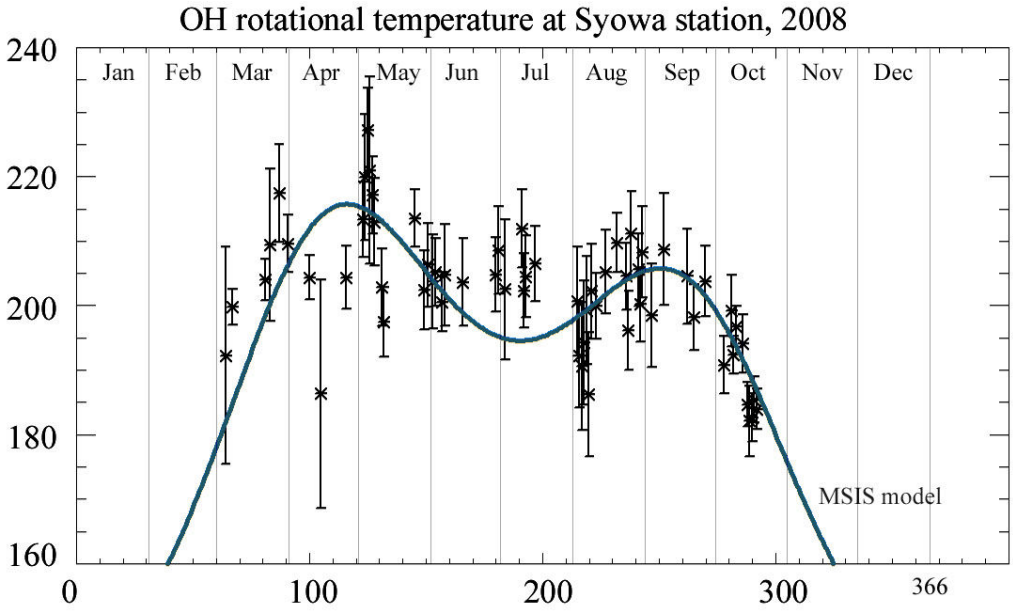

Figure 4-2. The seasonal variation of the daily averaged OH rotational temperature over Syowa Station in 2008. The error bar shows standard deviation of the fluctuation during each night. The solid blue line is the seasonal variation of atmospheric temperature from

the atmospheric empirical model MSISE-90 at 87 km height above Syowa Station (69S, 39E).

4-2 Large temperature fluctuations with a periodicity of several days in early May

As shown in Figure 4-1 and Figure 4-2, the large enhancement in the intensity of the OH airglow and the rotational temperature were observed in early May of 2008. Figure 4-3 shows the hourly averaged intensity of the Q-branch (upper panel) and rotational temperature (lower panel) during DOY from 123 to 130. The error bars show standard deviations of the fluctuations within the corresponding hour. The weather condition from 2 and 8 of May was very good with no moon light as shown in Table 3-2. Thus continuous observation except for day time was able to be conducted. The OH rotational temperature shown in Figure 4-3 consists of fluctuations with a periodicity of several hours to several days. The relatively rapid fluctuations with several hours are thought to be due to passing of gravity waves and atmospheric tides through the OH airglow layer. Figure 4-4 shows the comparison of the OH rotational temperature and hourly wind velocities of MF radar during the period from 2 to 8, May, 2008. Note that 24 hours running mean is removed from the MF data. In both eastward and northward wind data, the semi diurnal tide showing a downward phase propagation is clearly seen. The observation time during this season is about 14 hours a day, thus whole one cycle of the semi-diurnal tide is covered by the one night OH observation.

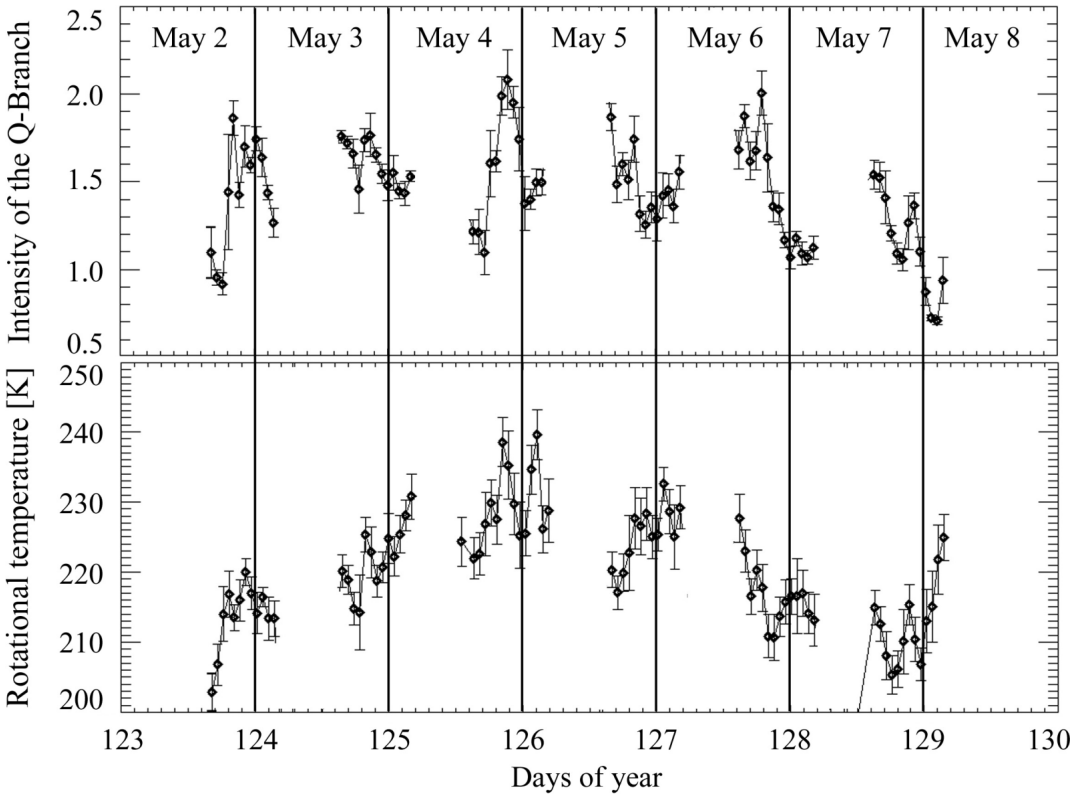

Figure 4-3. An hourly averaged intensity of the Q-branch (upper panel) and rotational temperature (lower panel) during DOY from 123 to 130. The error bar shows standard deviation of the fluctuations within an hour.

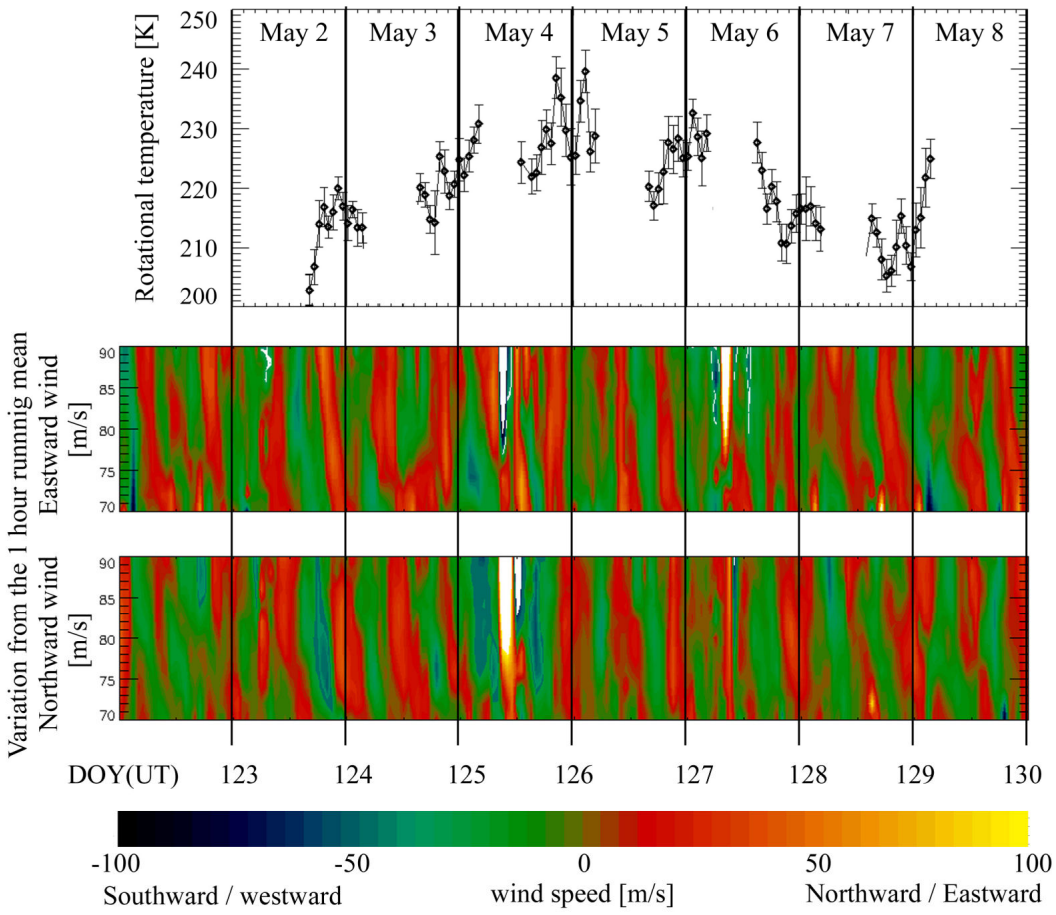

Figure 4-4. Comparison of the OH rotational temperature and wind speed measured by the MF radar during the period of from 2 to 8, May, 2008. 24-hour running mean is removed from the MF radar data.

To identify the source of the large fluctuation with a period of 5 to 6 days, the OH layer height observed by the SABER (Sounding of the Atmosphere by Broadband Emission Radiometry.) instrument onboard TIMED (Thermosphere Ionosphere Mesosphere Energetics and Dynamics) satellite is presented in Figure 4-6. SABER is a ten-channel radiometer providing near-global measurements of the emissions from several sources. Two of these channels are designed to observe the emission from OH airglow. These channels measure the 2.0μm and 1.6μm radiation from the pair of OH 9-7 and OH 8-6 and the pair of OH 5-3 and OH 4-0 bands, respectively [Russell et al., 1999].

From these data, a vertical profile of the volume emission rate from OH airglow can be derived. The other channels obtain near infrared to infrared radiation from CO_2 and these are used to retrieve atmospheric temperature and pressure up to ~100km altitude. The orbit of the TIMED satellite has 60 days yaw cycle; switching the northern hemisphere viewing mode (83°N-52°S) and southern hemisphere viewing mode (52°N-83°S) every 60 days. Fortunately, SABER was viewing the tangential points near Syowa Station in early May.

Figure 4-6 shows SABER profiles of the OH airglow volume emission rate (upper panel) and atmospheric temperature (lower panel) during DOY from 120 to 130. The OH peak height gradually descended from DOY 120, and reached the bottom height of 82~83km on DOY 125 or 126, and returned to the original height of ~86km 2 or 3 days later. This descending and ascending phases of the OH layer are coincident well the variation of rotational temperature observed by the ground based observation shown in Figure 4-3.

In addition, height vs. time contour plot of SABER temperature is shown in Figure 4-7 to clearly see the temperature profiles during this period. A relatively high temperature region is extended over upper mesospheric region (80 ~ 90km) around DOY 126, when the peak temperature is recorded with the ground observation.

The comparison of the temperature between SABER data and ground observation is also conducted. For the comparison, some processing of the SABER data are needed, because satellite data is height profiles of the temperature while the ground-based spectrometer temperature is averaged one through the layer weighted by the distribution of OH volume emission rate. Since SABER data has both the emission distribution of OH airglow and temperature, OH equivalent temperature can be derived by averaging the atmospheric temperature through the OH layer with weighting function that is made from simultaneously obtained OH profile itself.

Figure 4-8 shows the comparison between OH rotational temperature obtained

by ground observation and OH equivalent temperature derived from SABER data. The SABER profiles were obtained by averaging tangential points, typically 3 ~ 4 points, within 500km from Syowa Station. A good agreement between the ground observation and SABER data is seen except for the data in late DOY of 128. A possible reason for this difference is the effect of unknown local heating because the field of view of SABER is not completely the same with that of the ground observation. The unusual condition shown by SABER temperature data on DOY 128 is also seen in Figure 4-6 and Figure 4-7. The large temperature gradient and high temperature at upper altitude are clearly seen. Further discussion on this unusual event will not be made because it is out of the scope of this thesis.

4-3 Discussion and conclusions

Usually, seasonal variation shown in Figure 4-2 is thought to be a result of the global circulation modulated by gravity waves through momentum deposition [Lindzen, 1981]. The meridional circulation around the mesopause consists of meridional flow from summer to winter hemispheres, and ascends and descends in the summer and winter hemispheres, respectively. There is an upward motion that causes adiabatic cooling of the atmosphere at the polar summer mesopause region where the circulation starts, while in winter mesopause region, the end point of the circulation, descending motion causes adiabatic heating. Figure 4-5 shows contour plots of horizontal wind velocities over Syowa Station observed by the Middle frequency atmospheric radar (MF radar) in 2008. Fluctuations with a period shorter than 30 days are cut off to see the seasonal variation. The eastward component is roughly categorized into two seasons. The one is the summer circulation that is dominantly westward in all through the mesosphere corresponding to DOYs of 1 ~ 70 and 280 ~ 366 and the other is the winter circulation that is dominantly eastward corresponding to DOYs of 70 ~ 280. During summer, gravity waves with a phase speed directed to eastward have a more chance to propagate up to the mesopause

height (90-100km). Waves that break and are saturated around the mesopause region deposits the momentum to the background wind and accelerates it in their horizontal phase speed direction. As a result, the meridional circulation is driven to cancel the acceleration due to the waves with the Coriolis force. Thus the dragging forces by waves are mainly used for driving meridional flow. In winter, the inverse mechanism works and a pole-ward circulation is driven. The northward component shown in Figure 4-5 indicates this wave driven circulation pattern. At the mesopause height, the poleward (south ward) and equatorward (northward) wind is dominant in winter and summer, respectively. Therefore, the seasonal variation, high in winter and low in summer observed by the OH spectrometer is thought be due to the modulation by the inter hemispheric circulation.

The model has a midwinter minimum around DOY~190, while the ground data does not show such a feature. Furthermore, many large fluctuations with duration of several days are shown in the ground observation. One of the reasons for such differences is that the model is based on multiple year observations and short period variations are smoothed out. Another reason may be an effect of a fluctuation of the height of the OH airglow layer. In general the rotational temperature derived from OH airglow is assumed as atmospheric temperature at the mean OH airglow layer peak height, 87 km. However, recent satellite observations reveal a significant variability of the thickness, the peak height, and a height profile of the OH airglow with a seasonal scale [e.g. Winick et al., 2009]. Therefore it is necessary to include the effect of the layer height variation for detailed analysis of the rotational temperature.

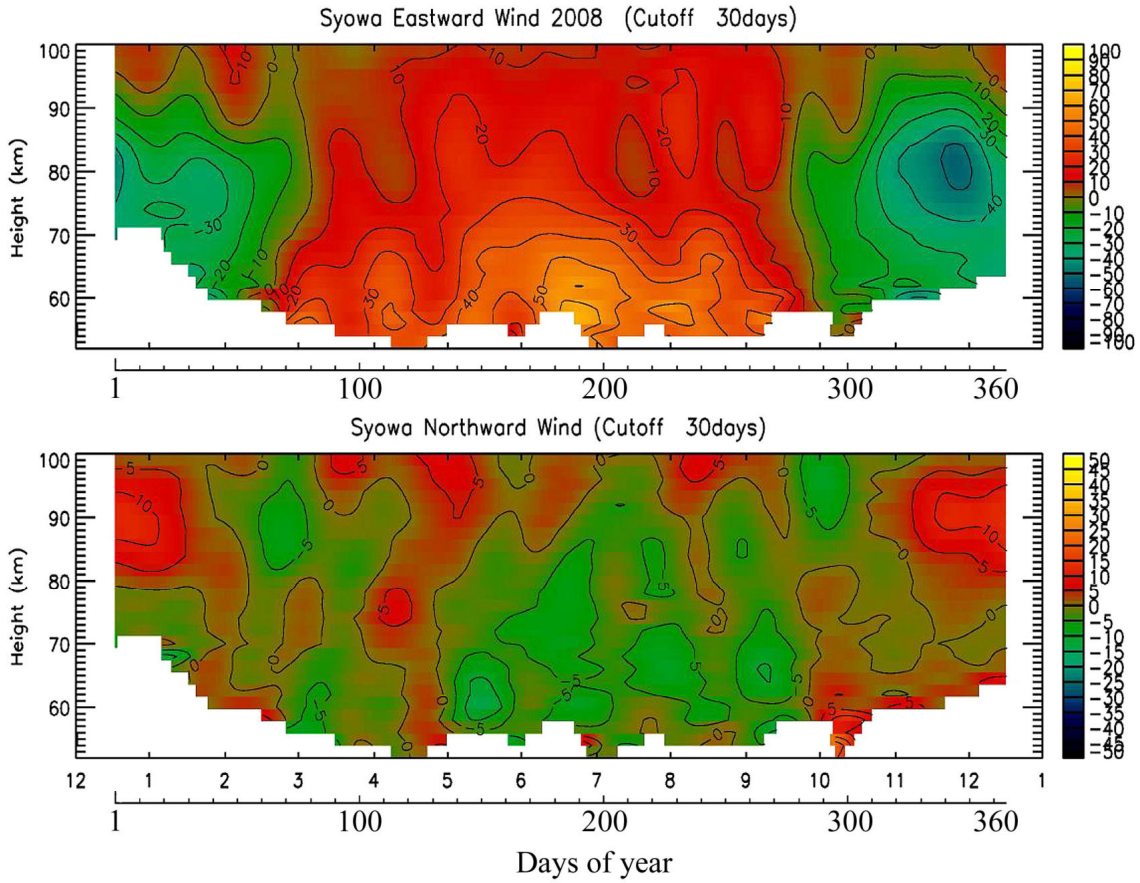

Figure 4-5. Contour plots of horizontal wind velocities over Syowa obtained using the MF radar in 2008. The upper and lower panels show eastward and northward winds, respectively. The fluctuations with a period shorter than 30 days are removed using a low pass filter. The unit of the wind speed is in m/s.

The large fluctuation in early May shown in Figure 4-2 is discussed considering the layer height effect in bellow. As a first interpretation for these results, the large temperature change during DOY 124 to 129 is due to the change of the peak position of OH airglow layer. However the descending of the peak height is 3 km at maximum. Thus gradient of the temperature, -7.0 K / km is needed to explain the 20K increase with the peak height change. However, no such gradients are shown in SABER temperature profiles shown in the lower panel of the Figure 4-6. Moreover most of these profiles show

the positive gradients of the temperature during this period.

The interpretation that explains both high temperature and lowering of the peak height of OH airglow is the downward motion of an upper atmosphere. This story has been already supported and verified by previous works. Recently, Liu and Shepherd [2006] show strong negative correlation between OH layer peak height and volume emission rate at there by using nearly 6 year data of WINDII (Wind Imaging Interferometer) onboard the UARS (Upper Atmosphere Research Satellite). They concluded that most dominant process which modulates the OH intensity and peak height is vertical motions, induced by tide, planetary wave and gravity wave in low to middle latitude. Their result can also explain the positive correlation between OH rotational temperature and intensity of an emission which many ground based observer has already showed in previous works because an adiabatic heating or temperature gradient effect can occur simultaneously with peak height lowering. In polar region, Cho and Shepherd [2006] showed a strong positive correlation between the intensity of OH airglow and rotational temperature using 4 winter ground observation data obtained with SATI (Spectral Airglow Temperature Imager) and found that such correlation is also seen for fluctuations with a wide range of periodicities from a single day to annual scale in Resolute Bay (74.68 °N). More recently, Winick et al. [2009] showed that such a correlation is also valid in unusual boreal winter condition in 2004 and 2006. They reported anomalous lowering of the OH airglow layer reaching 76 km and extremely high temperature reaching nearly 300 K in polar region (>60°N) by using SABER data in boreal anomalous winters, 2004-2005 and 2006-2007. Their result implies that the enhanced downward motion after stratospheric sudden warming events in 2004 and 2006 transported atomic oxygen and NOx species which had an effect to lower the peak height and enhance OH airglow. Though the mechanism for lowering OH layer height is different from that of a tide or a planetary wave, the observed relationship is the same. All these results support the generality of the fact that the predominant mechanism for

perturbations of OH intensity and rotational temperature are vertical motion and corresponding adiabatic heating or cooling.

The presented results also support previous works. The large fluctuation observed in early May, 2008 in Syowa Station is thought to be due to the enhancement of the downward motion and following adiabatic heating and temperature gradient effect in mesopause region. The enhanced amplitude of the vertical wind during the period can be estimated by a following simple discussion.

Assuming the temperature profile and constant vertical wind before the vertical wind enhancement as $T_0(z)$ and w_0, respectively, the equation of thermodynamics for initial condition is represented as

$$w_0\left(\frac{\partial T_0}{\partial z}+\frac{g}{c_p}\right)=-\frac{T_0-T_{rad}}{\tau} \tag{9}$$

, where g is gravitational acceleration, cp is a specific heat at constant pressure, Trad is radiative equilibrium temperature and τ is the time constant of a radiative cooling. After the vertical wind and temperature changed to $w_0 + w'$, and $T_0 + T'$, respectively, the equation of thermodynamics is represented as

$$\frac{\partial T'}{\partial t}=-(w_0+w')\left(\frac{\partial T_0}{\partial z}+\frac{g}{c_p}\right)-\frac{(T_0+T')-T_{rad}}{\tau} \tag{10}$$

, where the assumption, $\partial T'/\partial z = 0$ is assumed. From these two equations, a relationship between increase of vertical wind, w' and temperature, T' is derived as

$$w'=-\left(\frac{\partial T'}{\partial t}+\frac{T'}{\tau}\right)\Bigg/\left(\frac{\partial T_0}{\partial z}+\frac{g}{c_p}\right). \tag{11}$$

For observed case, $\partial T'/\partial t$ is about 20 [K]/2[days]. A typical value for τ is about 5 [days] [Wehrbein and Leoby, 1982], and g/c_p is ~9.7 x 10^{-5} [K/cm]. By using these values and an assumption of $\partial T_0/\partial z=0$, enhancement of vertical wind is estimated as 1.4 [cm/days]. The typical value for downward wind in spring season is about 0.5~1.0 [cm/day] at the mesopause height in Antarctica [Zhu et al., 2001; Dunkerton, 1978]. Thus increase of

temperature observed in early May is thought as a result of an enhancement of downward wind with a magnitude of twice order compared to the usual condition.

The comparison of SABER OH equivalent temperature and ground OH rotational temperature during the period when was SABER operated under the southern hemisphere mode in 2008 is shown in Figure 4-9. The altitude of the OH layer peak and atmospheric temperature derived by SABER during DOY from 80 to 140 of 2008 are shown in Figure 4-10. A good agreement between the ground OH temperature and OH equivalent temperature is also seen over the matched period. It is clearly seen through out the observed period that the OH layer height is higher when the upper mesosphere is colder, and vice-versa. The peak height of the OH airglow varies between 82km to 89km in the first half of winter in 2008 as shown in Figure 4-10. The large fluctuation observed in early May corresponds to the period of the lowest layer height. The range of the variation in peak altitude, ~7km, is relatively small compared to 14km (76 ~ 90km) observed by Winick et al. [2009] above 72 ~ 78° N in unusual boreal winter, 2004. The variations observed over Syowa in 2008 are similar to those observed in a typical year, 2005. This implies that disturbances in the upper mesosphere over Syowa Station in 2008 were not as significant as those found by Winick et al. [2009], which were caused by polar vortex breaking or stratospheric sudden warming. Finally, the difference between OH equivalent temperature and temperature at altitude of 87km, a typical peak altitude of OH airglow, is shown in Figure 4-11. Both temperature estimates reconstructed are reconstructed from SABER data. Although, the temperature variation pattern looks roughly the same between the two, individual values sometimes show differences as large as 10 K. The standard deviation of the differences is 3.9K. This is thought to be due to the layer height modulation effect. In fact, the correlation between the ground observed temperature and SABER OH equivalent temperature is much better than that with SABER temperature at 87km. This indicates that the vertical motion and following modulation of the OH layer is essential for fluctuation in OH rotational

temperature.

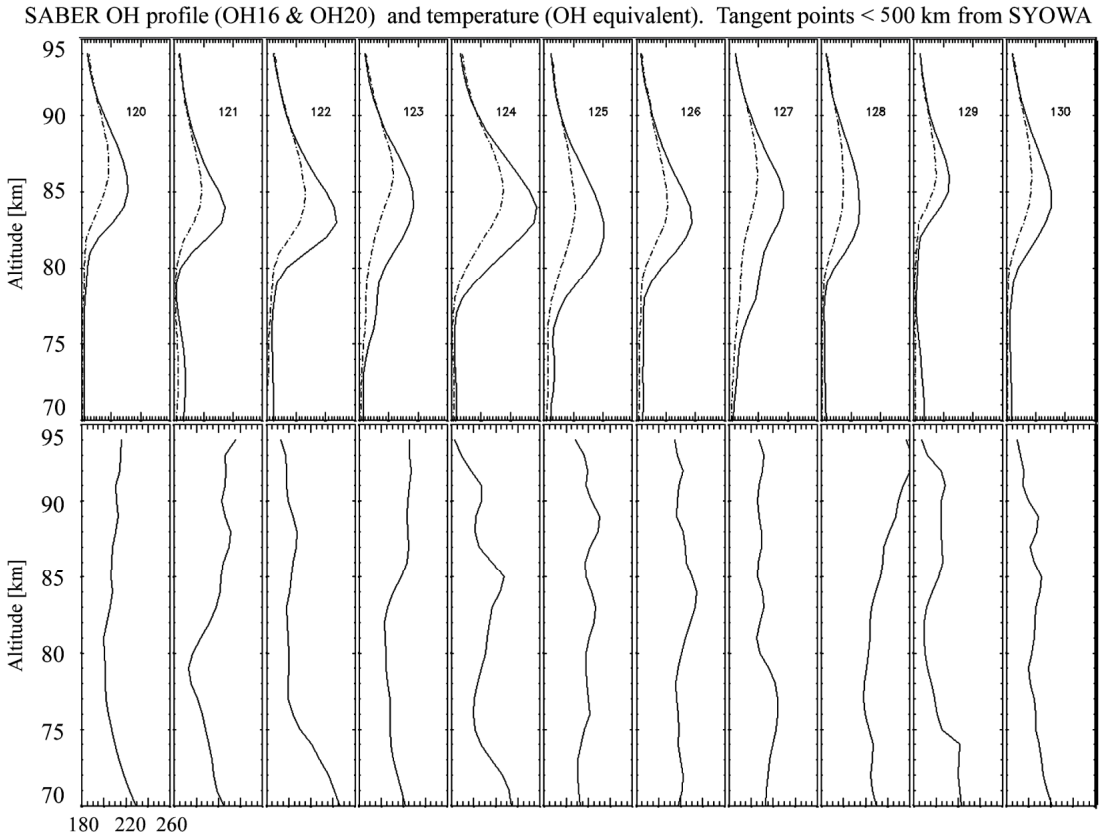

Figure 4-6. SABER profiles of the OH airglow volume emission rate (upper panel) and atmospheric temperature (lower panel) during DOY from 120 to 130. The SABER profiles were obtained by averaging tangential points, typically 3 ~ 4 points, within 500km from Syowa Station. The solid line and the dotted line shown in plot of the OH volume emission rate correspond to 1.6μm and 2.0μm channels, respectively.

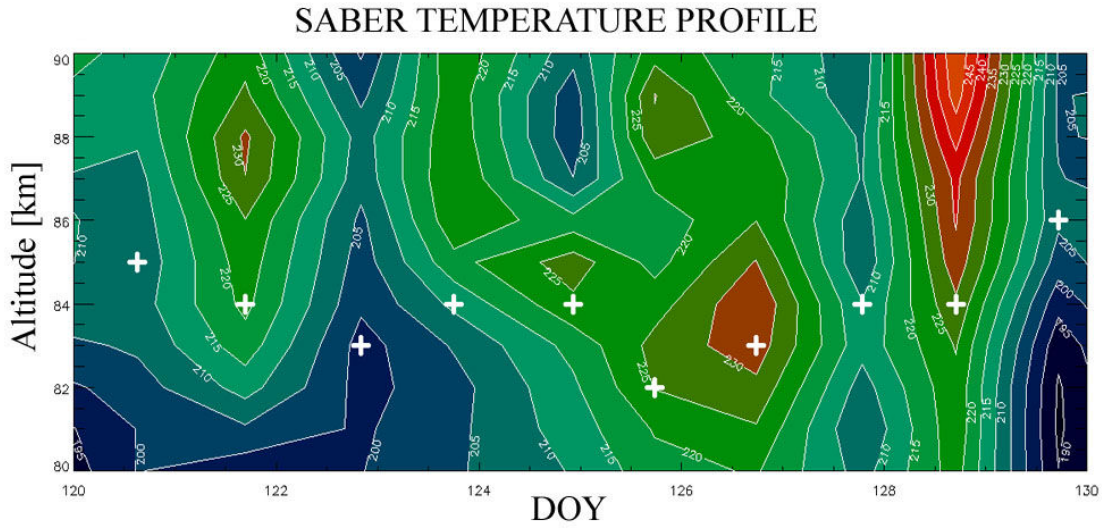

Figure 4-7. Altitude vs. time contour plot of the SABER temperature profile. The SABER profiles were obtained by averaging tangential points, typically 3 ~ 4 points, within 500km from Syowa Station. The over plotted cross mark indicates the position of the peak of the OH volume emission rate.

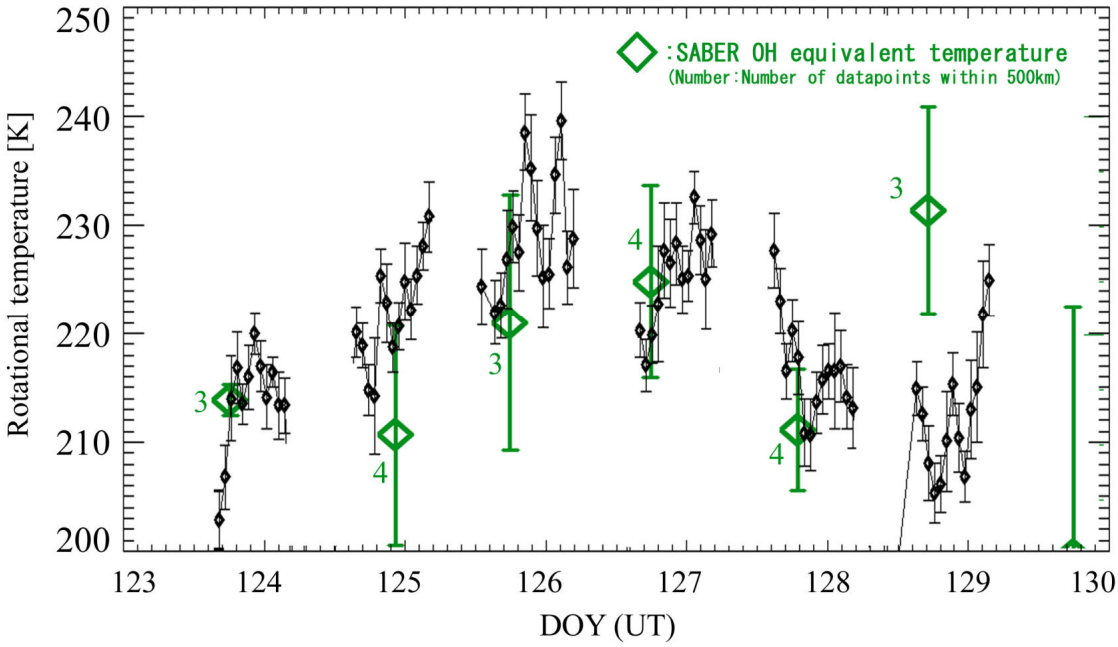

Figure 4-8. The comparison between ground observed OH rotational temperature and OH equivalent temperature derived from SABER data. The SABER profiles were

obtained by averaging tangential points, typically 3 ~ 4 points, within 500km from Syowa Station. The data number used to derive each SABER data is indicated by the number next to the square symbols. The error bar shows the standard deviation of these data.

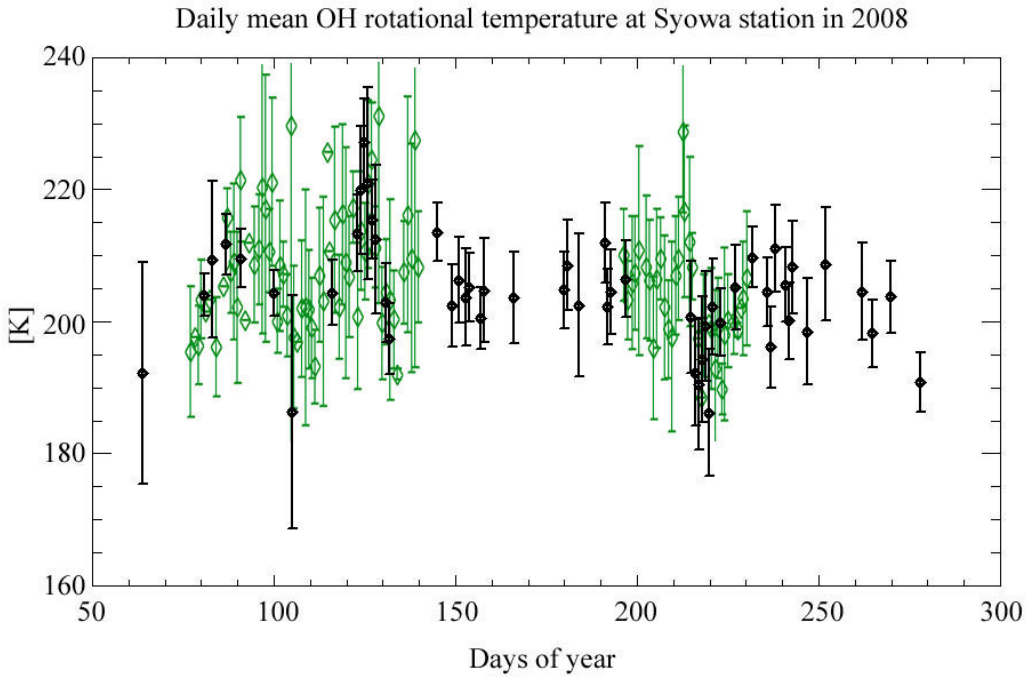

Figure 4-9. The comparison of SABER OH equivalent temperature and ground OH rotational temperature during the period when was SABER operated under the southern hemisphere mode in 2008. The black symbol shows daily averaged ground-base OH temperature. The green symbol indicates OH equivalent temperature derived from SABER data. The error bar shows standard deviation.

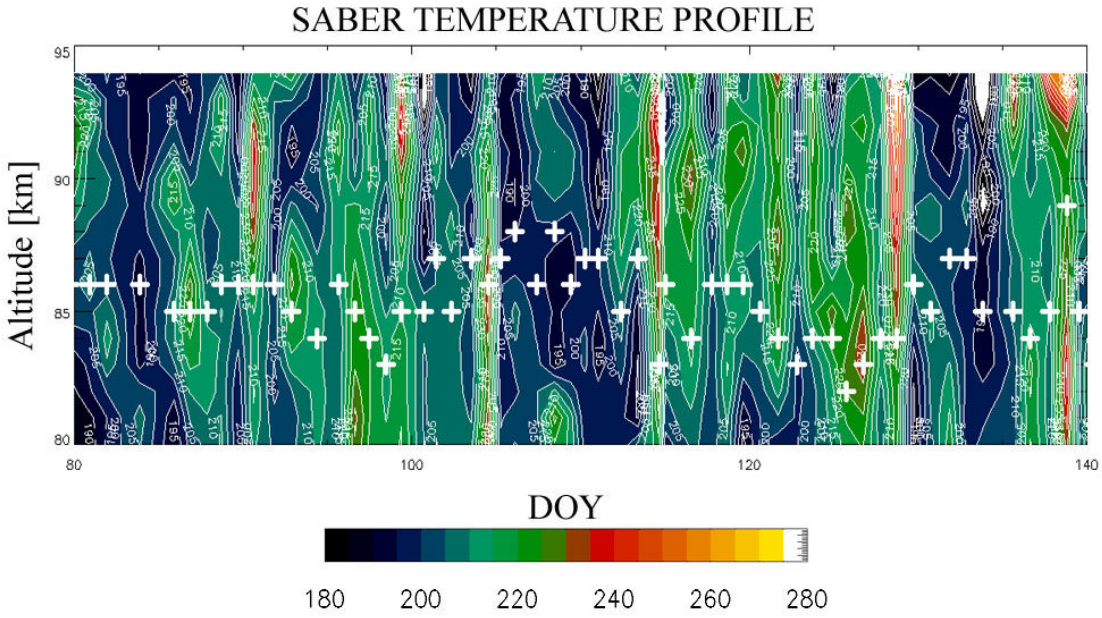

Figure 4-10. Same as Figure 4-7 except for DOY 80 to140.

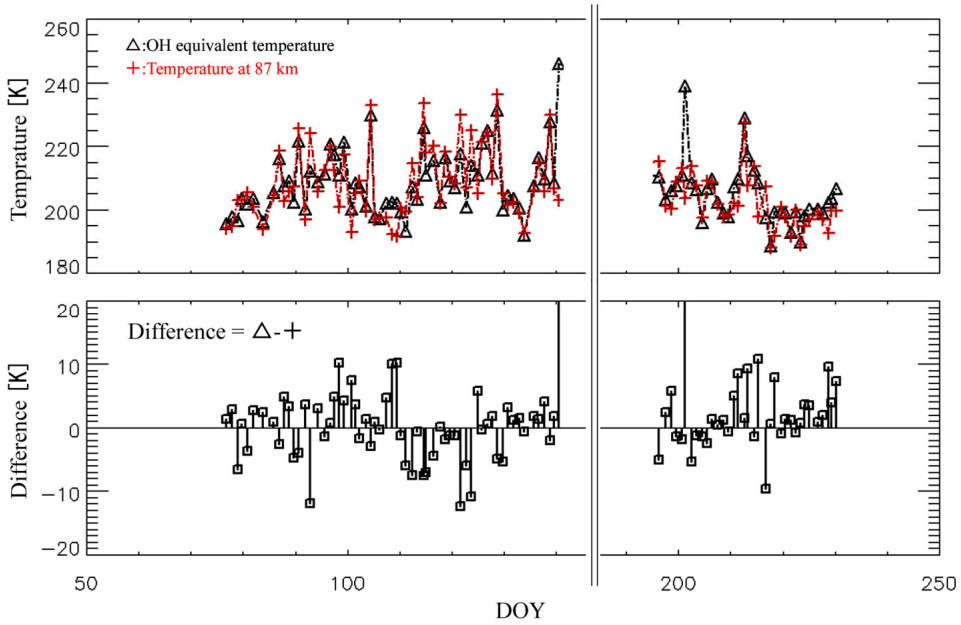

Figure 4-11. The difference between OH equivalent temperature and simple temperature at an altitude of 87km, both from SABER data. The data are averaged of the 3 – 4 points those tangent points satisfy within the 500km distant from Syowa Station.（standard deviation = 3.9 K)

5 Temperature variations due to auroral effects

5-1 Rapid and large temperature fluctuation observed on the night of active aurora event.

The main target of the OH spectrometer installed in Syowa Station is to detect effects of aurora precipitations on temperature and constituents at the mesopause height as mentioned in previous sections. In the observation made in 2008, rapid fluctuation that had a time scale of several minutes that seems to be related to the auroral activity is found on an only one night. Figure 5-1 shows the fluctuation of OH rotational temperature and intensity observed on 27th of March, 2008. The upper color image shows evolution of the visible aurora on a magnetic meridional cross section in the sky. This image is made from the images observed by the all sky color digital camera with a time resolution of 30 sec (see Chapter 2-6). In addition, the magnetic field variation and cosmic noise absorption (CNA) observed at Syowa Station are also displayed in the lower 2 panels. The intensity of each rotational line of OH 8-4 band shown in Figure 5-1 is relative intensity to the background counts. The second panel is the plot of the intensity for Q-branch and is rescaled. The data gaps shown in the temperature plot are missing values discarded based on the criteria (See 3-1). These missing data points are invalid value caused by a contamination from strong auroral emission. The dotted line shown in the color aurora image indicates the field of view of the spectrometer corresponding to the magnetic zenith direction. The data missing periods correspond to the periods of active bright aurora.

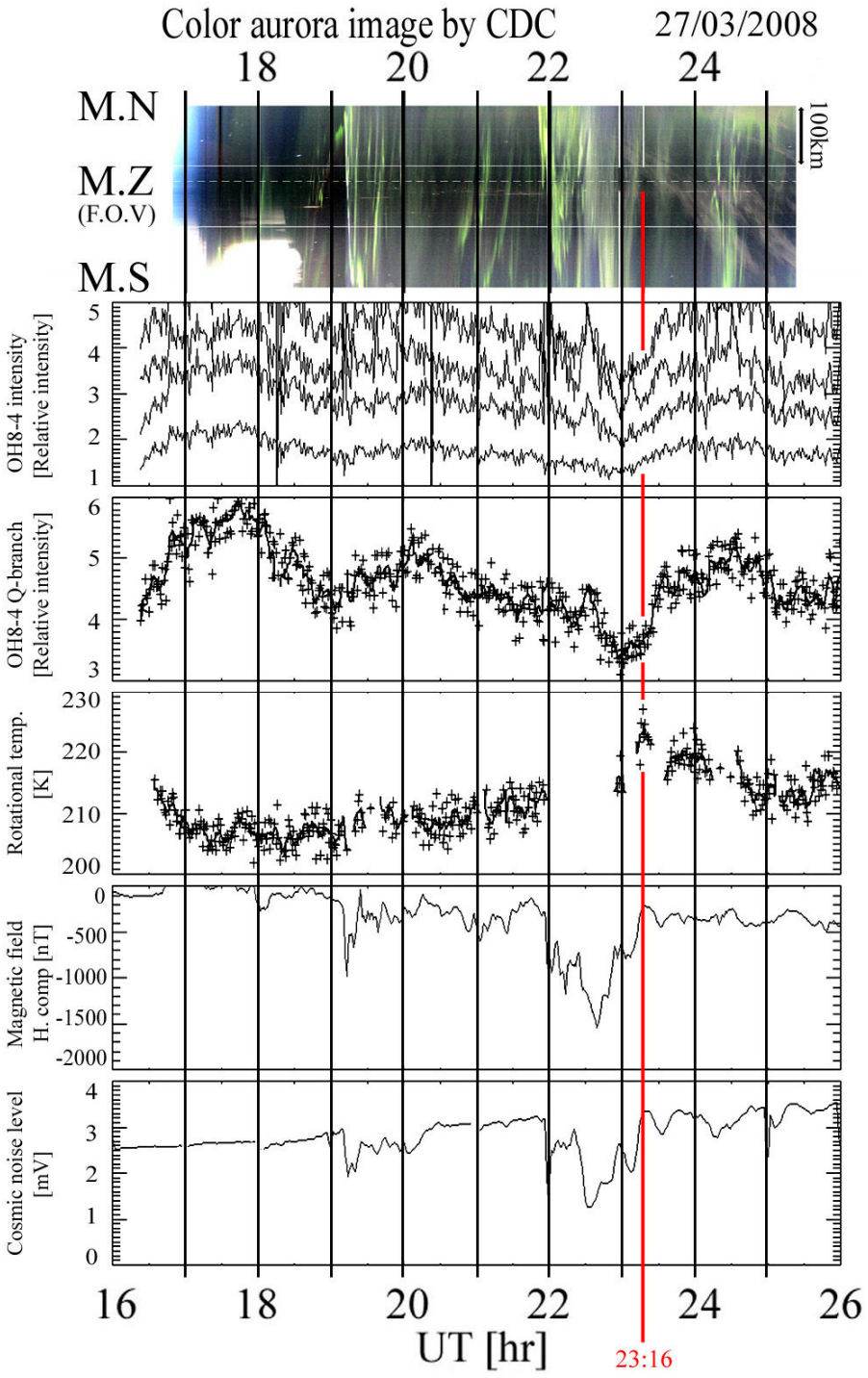

Figure 5-1. Fluctuation of OH rotational temperature and intensity observed on 8th of March, 2008. The top color image shows evolution of the visible aurora on the line between magnetic north to magnetic south in the sky. This image is made from a data set observed by the all sky color digital camera (see Chapter 2-6). In addition, the

magnetic field variation and cosmic noise absorption (CNA) observed in Syowa Station are also displayed in the lower 2 panels. The solid line shown in the plot of magnetic field variation is the horizontal component (H component.). The notation M.N, M.S, and M.Z indicate magnetic north, south and zenith, respectively.

In this night, aurora broke up two times around at 19:20 and 21:50 UT. There are no remarkable variations on both intensity and rotational temperature during first break up of aurora which lasted from 19:20 to 20:00 UT. The maximum variation in the horizontal component of the magnetic field was recorded about 1000 not during this period. The maximum drop of cosmic noise level is about 2.0 dB (3mV to 1.8mV) during the period. However, rapid and large fluctuations were seen in both intensity and rotational temperature during the second break up of aurora, which lasted from 21:50 to 23:15 UT. Fortunately, aurora arc temporarily went out of the field of view of the spectrometer two times at around 23:00 UT and 23:16 UT and valid temperature during those period can be determined. The rising of the rotational temperature was seen during this period. Figure 5-2 shows more details about this fluctuation. This plot is the same as the Figure 1-1 but period from 21 UT to 24 UT is closed up. The solid lines shown in the second and third panels are 5 point (5 minute) running mean values. The five vertical lines to show the time of key phases are embedded. The temperature around 22:57UT was about 215 K but it was not so different from the temperature at 21:55UT. The rapid raising of temperature occurred after 22:57 is remarkable and reached peak temperature about 225 K at 23:16. In addition to the rising of temperature, remarkable decrease of the intensity of OH airglow was also seen nearly at the same time. The timing of the rapid temperature increase corresponded to the end of the disturbances in the magnetic field and the cosmic noise radiation level. The difference in strength of the cosmic noise level between quiet and disturbed conditions is called CNA (Cosmic noise absorption) which reflects the electron density of the D-region (< 90km). A large decrease of the cosmic

noise radiation level means hard electron precipitation to the atmosphere around or under 90 km altitude. In this case, about 20% decrease of the intensity of the OH airglow and ~10K rising of the rotational temperature after ~4 dB CNA were observed. The amplitude and periodicity of these variations are not impossible to be explained by atmospheric gravity wave perturbations. However, phase relationship between intensity of the OH airglow and rotational line for this case is almost anti-phase. Generally, a positive correlation is seen between the intensity and the rotational temperature if the variations are due to the passing of the atmospheric gravity wave [Cho and Shepherd, 2006]. Thus, the variation for this case can be thought as the effect of hard auroral precipitation.

5-2 Discussion and conclusions

According to the Liu and Swenson [2003], the volume emission rate at certain height is determined by the kinetic temperature, density of atomic and molecular oxygen, and molecular nitrogen and expressed by,

$$\varepsilon_{OH} = \frac{f_8[\mathrm{O}][\mathrm{O}_2]\left(k_6^{N_2}[\mathrm{N}_2] + k_6^{O_2}[\mathrm{O}_2]\right)}{\left(260 + 2\times10^{-11}[\mathrm{O}_2]\right)}, \quad (12)$$

where $f_8 = 0.29$ is fraction of emission at vibration level 8, $k_6^{N_2} = 5.7\times10^{-34}\ (300/\mathrm{T})^{2.62}$ and $k_6^{O_2} = 5.96\times10^{-34}\ (300/\mathrm{T})^{2.37}$ are quenching coefficients. The brackets [ ] represent number density in unit of cm^{-3}. ε_{OH} is in unit of photons $\mathrm{cm}^{-3}\ \mathrm{s}^{-1}$. Since quenching coefficients are inversely proportional to the kinetic temperature, the volume emission rate decreases as rising temperature. The pure temperature dependent volume emission rate of the OH airglow calculated using the equation (12) and typical values of [O]= 2.163×10^{11}, [O_2]= 1.276×10^{13}, [N_2]= $4.903\times10^{13}\ \mathrm{cm}^{-3}$ at 90km height (by MSIS model) is showed in Figure 5-3. This pure temperature dependent model shows inversely correlation between kinetic temperature and the volume emission rate (VER). The decrease of intensity of airglow expected for 10 K rising of temperature as in the case of Figure 5-1 is 12 %. This value is roughly comparable with observed value ~ 20%. This shows possibility of the auroral heating of the atmosphere in the mesopause region. However, the direct heating of the mesopause atmosphere by the aurora precipitation seems difficult, at least in the present case as shown below.

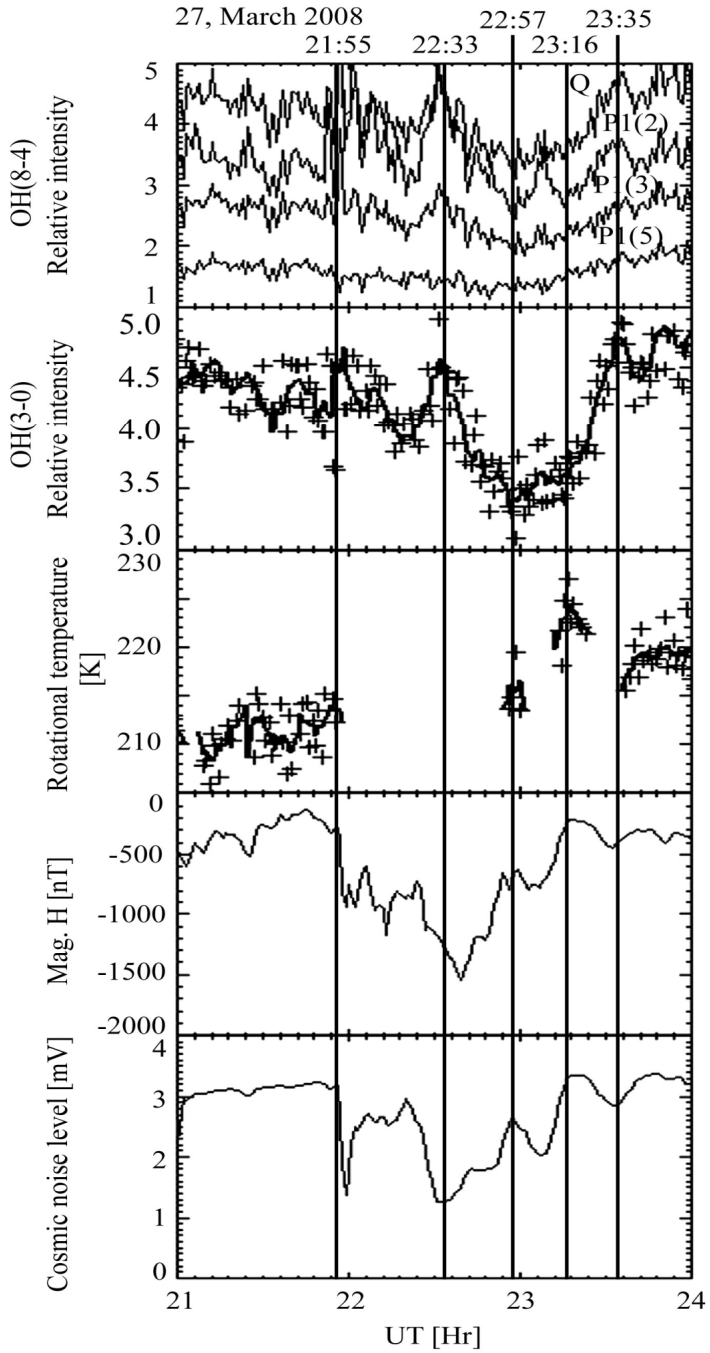

Figure 5-2. Same as Figure 5-1 but during the period from 21 UT to 24 UT. The solid lines shown in the second and third panels are 5 points running mean values. The five vertical lines are embedded to show the time of key phase.

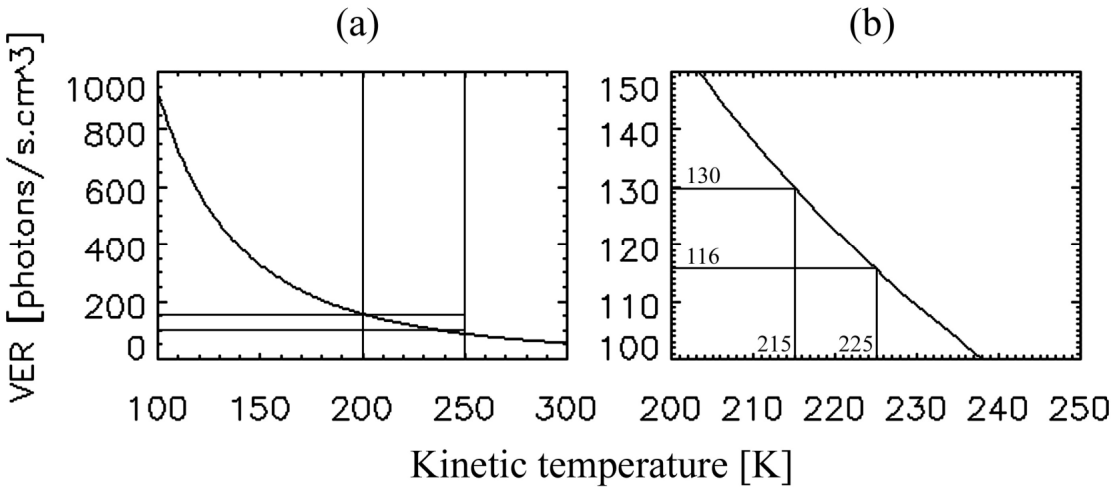

Figure 5-3. Temperature dependence of the volume emission rate (V.E.R) of OH airglow. The number densities of species that related to OH airglow are all fixed as empirical model values at 90km height. Panel (a) and (b) are same but the range is different.

Joule heating and particle heating by auroral precipitations are significant energy sources in the polar thermosphere. However, in general, it is difficult that these effects raise temperature at the mesopause height (~90km) because of the higher density of atmosphere. A heat capacity of neutral atmosphere at 90 km height is about 3×10^{-3} [J/ K m3]. This means heating rate required to explain the temperature increase of 10 K during 15 minutes (the case shown in Figure 2) is about 3.8×10^{-5} [J/s m3]. This value is too high compared to the Joule heating rate obtained by radar observation in past. For example, Joule heating rate observed by the EISCAT (European Incoherent Scatter) radar at 90km height is variable but has an order of 10^{-8} [J/s m^3] at most [e.g., Brekke, 1997]. The particle heating by direct collision of auroral particles with neutral atmosphere is possible if there are enough energy flux depositions by electron precipitations. According to Berger et al. [1970], the energy deposition of an energetic particle which has incident energy of 20 keV and pitch angle of 0 degree deposits about 10^{-19} [J] per unit meter penetration around the 90km height. Thus order of 10^{14} [m-2 s-1] flux can maintain the

required energy deposition of 10^{-5} [J/s m3]. However this flux is also far too high for high energetic electron (> 20 keV) compared to those calculated by previous works [e.g. Brekke, 1983].

A typical mechanism that explains the fluctuations in the OH rotational temperature with a period of several minutes to hours is the passing of atmospheric gravity waves through the layer. In fact, the amplitudes and time scales of the order of the observed case (about 10 K/15 min) are often seen on auroral quiet nights at Syowa Station. However, as shown by Cho et al. [2006] and many ground observers, the phase value of the ground-observed intensity of the OH airglow and the rotational temperature show mostly a positive correlation with a small phase shift. This is due to the passing of an atmospheric gravity wave through the airglow layer accompanied by compression (expansion) and adiabatic heating (cooling) of the atmosphere. This relationship between the OH rotational temperature and the intensity of the OH airglow is discussed through a modeling study by Liu and Swenson [2003]. The observed phase values shown in Figure 5-2 are negatively correlated. This implies that the observed case is not caused by passing atmospheric gravity waves.

A possible mechanism that explains both the increase in rotational temperature and the decrease in the intensity of OH airglow is related to a change in the height distribution of the OH airglow emission. The rotational temperature derived from a ground-based observation is an averaged value over the OH airglow layer. Therefore, if temperature changes linearly with height, and a volume emission profile of the OH airglow has a symmetric shape relative to the peak height, the height integrated rotational temperature is equal to the temperature at the peak height. However, if the emission weakens in the upper part of the emission layer by hard auroral precipitations, the weighting profile of the OH layer is biased to the lower altitude relative to the peak height. Since a typical vertical temperature gradient of this region is negative, the lowering of the weight of an OH distribution causes an increase in the rotational temperature.

Figure 5-4 illustrates this mechanism. The initial profile is the OH volume emission rates synthesized from the data obtained by the SABER instrument onboard the TIMED satellite (details in Russell et al. [1999]) on March 27, 2008. The data used to make the initial OH profile are averaged over the horizontal region within 500 km from the Syowa Station. The OH volume emission rate profile is then fitted by a Gaussian function. The Gaussian function is characterized by a peak of 85 km, and a layer thickness of 8 km is plotted with a dashed line in Figure 5-4. An example of the disturbed layer profile is also shown in Figure 5-4 with a thick solid line where the upper part of the layer is decreased, and the total amount of the layer is 20% less than that of the initial conditions.

The temperature profile shown in Figure 5 4 with a dot-dashed line is zonal mean temperature for March at 70°S referred from the CIRA (COSPAR International Reference Atmosphere) model [Fleming et al., 1990]. A steep temperature gradient is seen within the OH layer. If it is assumed that the OH layer was disturbed similarly to that shown as the solid line in Figure 5-4, the rotational temperature values obtained before and after the disturbance are estimated to be 186 K and 190 K. Therefore, approximately 4 K of the observed temperature increase can be explained by this mechanism. However, the actual temperature profile on the night might not show such a gradient. The 30-day SABER temperature data (DOYs 72-102) were averaged and are shown in Figure 5-4 as a thin solid line together with the standard deviations as horizontal bars. Considering the local time dependence of the temperature structure caused by the atmospheric tidal waves, the profiles observed at LT00:15 to 04:15 (the time of the OH temperature increase is LT2:15) and at the latitude within ±10° from the Syowa Station were used to obtain the averaged profile. It is noted that the averaging corresponds to the extraction of local time-dependent variations such as migrating atmospheric tides. Therefore, the effects of the nonmigrating tides might be smoothed out. According to Murphy et al. [2006], nonmigrating semidiurnal tides are not trivial components in the latitude around the

Syowa Station in March. However, the vertical wavelengths are long enough relative to the OH layer thickness. Thus, these components are not effective for raising the rotational temperature with the height variation of the airglow layer. If this profile is the assumed background condition at the event time, the rotational temperature after the auroral disturbance does not increase but slightly decreases because of the positive vertical gradient of the temperature within the OH layer height. Thus, it is difficult to explain the increase in the rotational temperature only by the layer height variation in such cases.

In addition to the background temperature, local dynamical effects such as gravity waves might be important. The temperature profile plotted with a dotted line is the SABER temperature of a tangential point, which is 60 km from the Syowa Station, observed at 20:30 UT on March 27, 2008. In this profile, a slightly negative gradient and vertical wave structures thought to be caused by gravity waves are seen. If this profile is assumed to be the background condition, the rotational temperature obtained from the ground-based observation under the initial and disturbed conditions are estimated to be 209 K and 211 K. Thus, approximately 2 K of the observed temperature increase can be explained by this mechanism in this case. Even though this single temperature profile is that taken at a different location and time from the temperature increase event at Syowa, and the estimated increase is still smaller than the observed value, the significance of the local temperature structure can easily be determined based on this example.

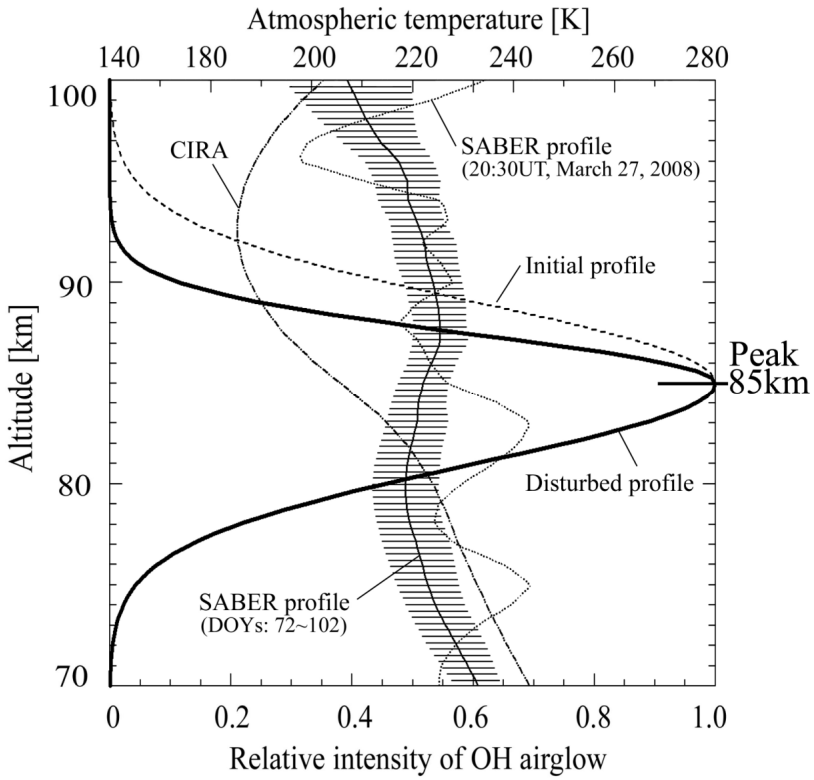

Figure 5-4. A model that explains the observed increase in the rotational temperature and decrease in the intensity of the OH airglow intensity. The SABER temperature obtained near the Syowa station (dotted line), the 30-day averaged (thin solid line with error bars) temperature, and the zonal mean temperature (dot-dashed line) profile for March at 70°S obtained from the CIRA86 atmospheric model are plotted. The initial profile of the OH airglow emission rate is based on the data from the SABER/TIMED (see text).

The mechanism to explain the decrease in OH emission rate is still unsolved. The possibility of decreasing OH emission rate during hard auroral precipitation was predicted by a theoretical work by Maeda [1967]. He reproduced enhancement of O2 dissociation by auroral electron bombardment followed by decrease in production rate of exited OH molecules using a time-dependent 1-D chemical model. Since only a case for extremely high energy flux with a characteristic energy of 100 keV and a total number flux of 10^{14} $m^{-2}s^{-1}$ is shown in this work, decrease in an OH emission rate occurred over

the entire layer. However it is possible to reduce emission in only the upper part of OH emission layer, if appropriate hard precipitations are continued.

The variation related to auroral activities was seen only on the night of 27th, March among all observed nights of 2008. Though the auroral activity of 2008 was very low because of the minimum solar activity, dataset of 6 nights are good condition to compare aurora and OH temperature variations. However, as mentioned above, there were no remarkable fluctuations on OH rotational temperature correlated with auroral activity on these nights except 27th of March, 2008. As an example of the aurora unrelated fluctuation of OH rotational temperature and intensity, plot on 3rd of September, 2008, is shown in Figure 5-5. As shown in the top image by CDC, active aurora was observed in this night. However no remarkable disturbances related to aurora activity is found. From the observation staring time of 16:00 UT to the aurora showing up time of 23:00UT, typical positively correlated fluctuations in intensity and temperature were seen. After the aurora appeared in the field of view, temperature data are missing until 25:30UT. However no notable trends were found during this period in both temperature and intensity. After around 25:30, active aurora showed up and continued until morning twilight. Thus no valid temperature value exists after that. However, intensity of Q-branch was available until twilight. Though the color image and horizontal magnetic field fluctuation that reached 1300 nT at maximum after 25:30UT indicates a very high aurora activity, there are no correlated fluctuation in intensity during the period. The brightness and movement of visual aurora was actually very strong on this night. The only difference of the condition compared with that of 27th of March, 2008 is low magnitude of CNA. As mentioned above, CNA is a measure of electron density at the mesopause region. Thus it may be reasonable that no obvious auroral effect can be detected on the night of 3rd of September, 2008 even if visually active aurora had been seen.

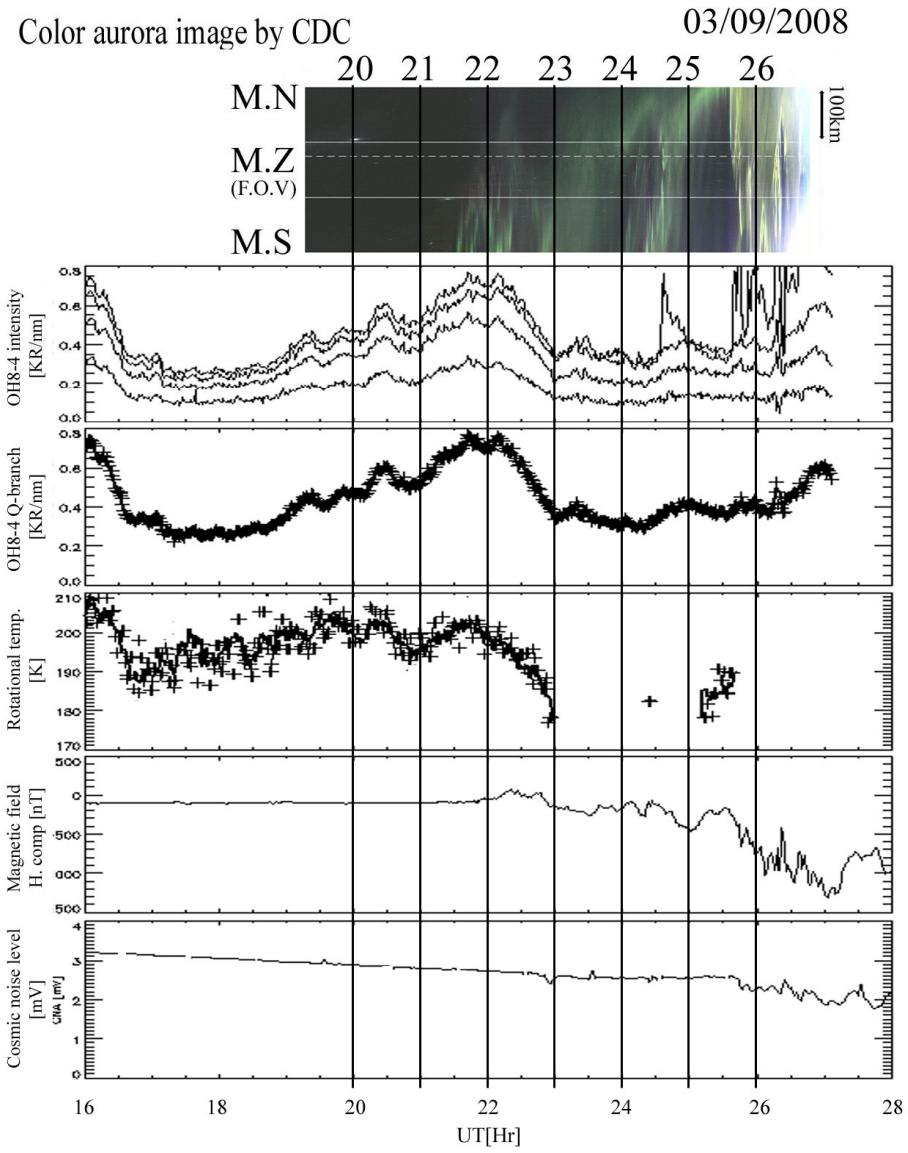

Figure 5-5. Same as Figure 1-1 but on 3rd of September, 2008.

An intensity of energy deposition can be estimated by the luminosity of auroral emission. Thus the luminosities of auroral emission from 557.7nm, 630.0nm and 427.8nm taken by ASI (see 2-6) on 6 active aurora nights are compared. According to theoretical works conducted by Gattinger and Jones [1972] or Rees and Luckey [1974], the parameters of an auroral precipitation such as the average energy and total energy flux can be estimated by using the ground observed intensity of an auroral emission.

The most familiar method is to use the intensity ratio of 630.0nm (OI) to 427.8nm (N_2^+1NG) auroral emissions because the ratio depends on the energy of the incoming auroral electrons [Rees and Lucky, 1974]. Figure 5-6 shows average energy of precipitating electrons after refined Model by Ono, [1993] (triangle symbol) and those summarized by Vallance Jones et al. [1987], based on the energy dependence of the intensity ratio of 630.0 nm emission to 427.8 nm emission [Ono, 1993]. Though, factors of derived average energy from intensity ratio are slightly different for each model, the inverse proportion between average energy and ratio of 630.0nm to 427.8nm is common sense. Figure 5-7 shows the luminosities of auroral emission from 557.7nm, 630.0nm and 427.8nm taken by ASI (see 2-6) on 6 active aurora nights. The lower panel of the each day plot shows intensity ration of 630.0nm to 427.8nm (I(630.0)/I(427.8)). The intensity ratio is plotted only when 557.7nm emission exceeds 10KR. These 6 days were the active auroral days and all of then show ratio, I(630.0)/I(427.8) of 0.2 to 0.3 at least one time or more. This means the average energy of electron precipitations for these days temporary reached from 10 to 20 keV according to the relationship shown in Figure 5-6. However, duration of such high energy precipitation is especialy high on the night of 27th of March, 2008 relative to other nights. In addition to that, the intensity of 427.8nm, I(427.8), which is sensitive to the high energy precipitation, was also high (~4kR) during 22:00 ~ 23:00UT on the night. This fact shows that the precipitation on 27th of March was especialy high.

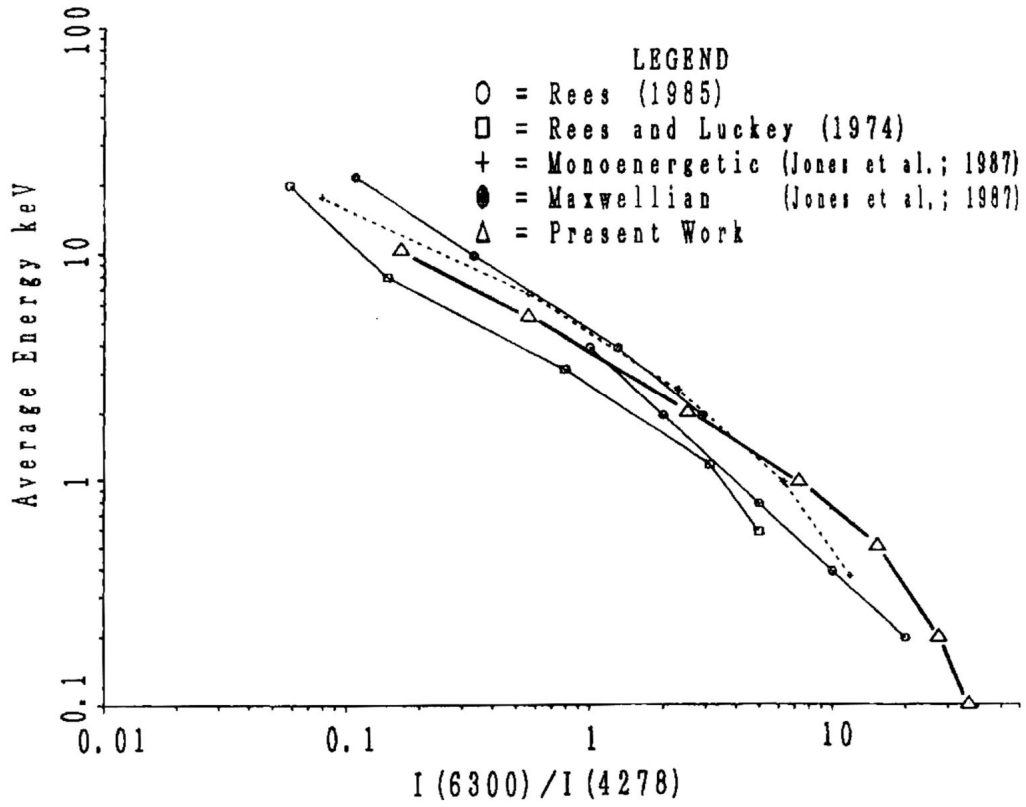

Figure 5-6. Average energy of precipitating electrons after Model by Ono [1993] (triangle symbol) and those summarized by Jones et al. [1987], based on the energy dependence of the intensity ratio of 630.0 nm emission to 427.8 nm emission [Ono, 1993].

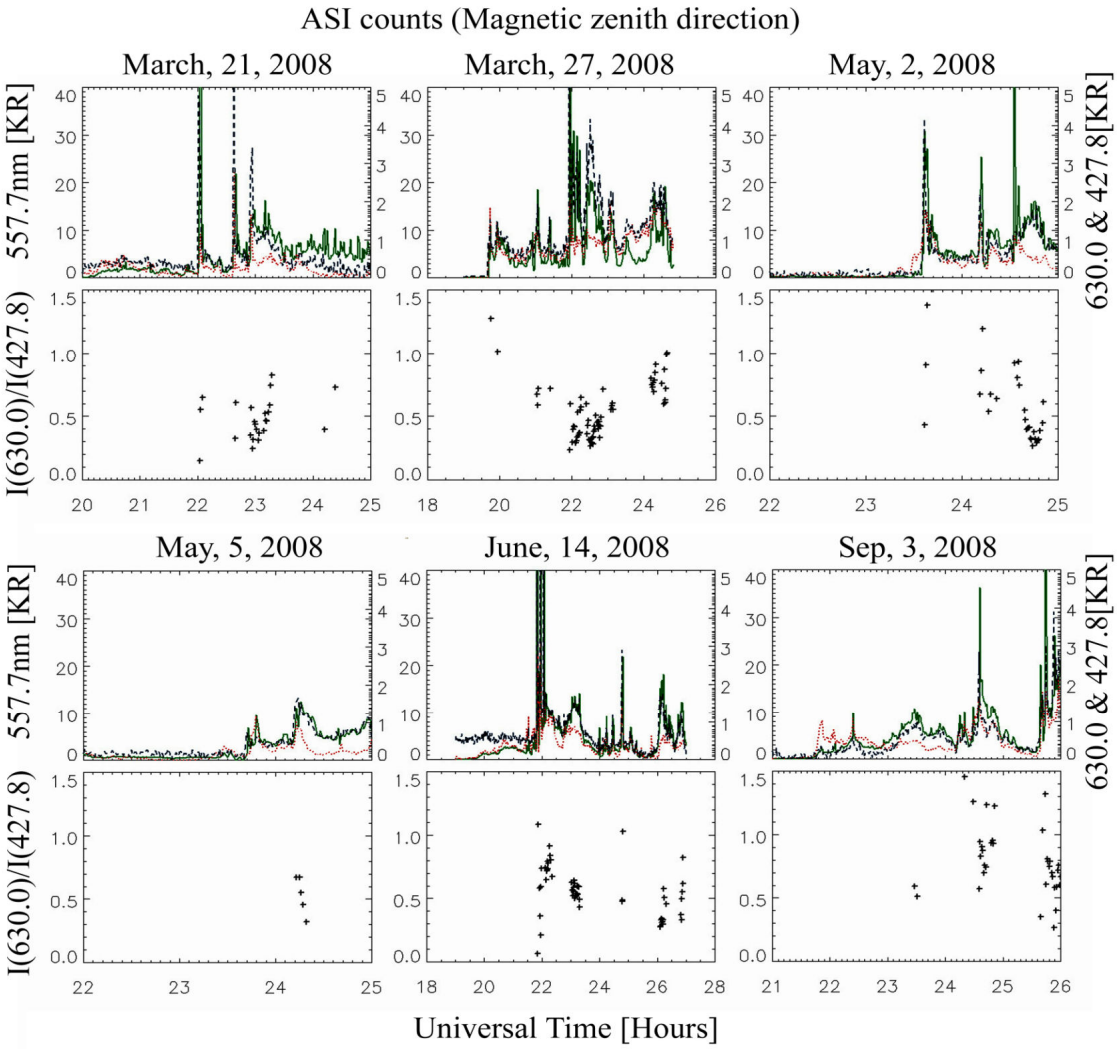

Figure 5-7. The luminosities of auroral emission from 557.7nm (green solid line), 630.0nm (red dotted line) and 427.8nm (blue dushed line) taken by ASI (see 2-6) on 6 active aurora nights. The lower panel of the each day shows intensity ration of 630.0nm to 427.8nm.

Though it may be unnecessary to consider the effect of auroral precipitation on OH rotational temperature and intensity under a moderate auroral activity, this result indicates possibility of auroral effect on OH rotational temperature and intensity accompanied with composition changes at the mesopause when auroral activity is extremely high.

6 Summary and conclusions

A fast spectrometer specifically designed to observe high-resolution spectra of the OH vibrational-rotational band in the auroral zone has been developed. The target band selected was the OH 8-4 band at a wavelength of around 950 nm in a nightglow spectrum. Based on survey observations in the Arctic, this was considered to be the most suitable vibration-rotation band for observation in the polar region, since it suffers less contamination from strong aurora emission. The new spectrograph consists of a fast optical system, a transmission grating and a CCD camera. The operating spectral region just encompasses the OH 8-4 band (900-990 nm) and a moderate spectral resolution (0.27 nm) is realized. A back-illuminated CCD with an infrared-enhanced quantum efficiency is used as an imaging device. The sensitivity and spectral resolution of the spectrograph were calibrated at NIPR. The instrument was installed in the Optical Building at Syowa Station in February, 2008 by the 49th Japanese Antarctic Research Expedition. The instrumental field-of-view (4.5×0.007 deg) is directed towards the local magnetic zenith. The nominal exposure time is 1 min.

In total, observations were carried out over 158 nights. Of these, 59 were perfectly clear, 57 were cloudy or sometimes clear, and the remainder were completely cloudy. The dataset contains both short- and long-term variations. The seasonal trend in the OH rotational temperature and the intensity of OH airglow for 2008 were determined. High and low values for rotational temperature were found in winter and summer, respectively. This is consistent with the trend in typical atmospheric temperatures observed in the polar mesopause region. This trend is thought to be the result of modulation of the global meridional flow, based on a comparison of wind data obtained by the MF radar. No clear local time dependence of OH airglow and temperature can be identified during 2008, whereas a clear trend is seen in auroral activity, with high activity always found after midnight.

In addition to the seasonal variations, a large day-to-day variability in rotational temperature and intensity of OH airglow is observed. A large fluctuation of +20 K during 2 days was observed in early May, 2008. This was found to be induced by enhanced downward motion followed by lowering of the OH airglow layer above Syowa Station, based on a comparison with the OH height and temperature profiles measured by the SABER instruments onboard the TIMED satellite. A good correspondence was found between the equivalent OH temperature derived using SABER data and ground-based measurements. The main cause of fluctuations of the rotational temperature is adiabatic heating associated with vertical motion following layer-height modulation above Syowa Station.

Rapid fluctuations with time scales of several minutes related to auroral activity were found on March 27, 2008, when the activity was the highest of the year. A rise in temperature of 10 K and a simultaneous decrease in OH-airglow intensity of 20% were observed following hard auroral precipitation. The high auroral activity on this night was associated with extremely high cosmic noise absorption (~4 dB) recorded by a RIO meter, and a large horizontal magnetic field disturbance (~-1500 nT) in Syowa Station. Although high auroral activity was also observed on September 3, 2008, there was no accompanying temperature rise. One clear difference between the two nights is the magnitude of CNA. That is also the case for other active aurora days on which no auroral effects are seen.

The most likely mechanism driving the rise in rotational temperature is variation of the altitude of the emission-peak layer due to a change in the numerical density of constituents caused by auroral precipitation.

Although there are no auroral effects in normal auroral activity, this study reveals that there are rapid fluctuations associated with high auroral activity or hard particle precipitation in the polar mesopause region. Auroral effects on the temperature in the mesopause region are not significant in the long term, but there is impulsive energy

input from auroral precipitation when auroral activity is extremely high. This indicates the possibility that auroral precipitation can act as a source of atmospheric disturbances such as gravity waves.

In this thesis, only a single case of a rise in rotational temperature is shown. Thus, the mechanism suggested here to explain this increase is not definitive, and further observations on active auroral nights are required. It is expected that such observations will become easier during the next few years since auroral activity is likely to increase with increasing solar activity (2008 was the minimum of the solar activity cycle). In addition, knowledge of the background temperature profile is valuable for checking the degree of influence of changes in the altitude of the OH layer. For this purpose, simultaneous Lidar observations can be carried out. Although Lidar data does not have a temporal resolution as high as OH spectrometry data, it can yield altitude profiles of atmospheric temperature. A plan to install a Lidar system at Syowa Station is now under discussion by NIPR, so that such simultaneous observations may become possible in the near future.

Appendix: Fluctuations caused by gravity waves

As described in Section 1-3, fluctuations caused by gravity waves are frequently observed in OH airglow intensity and rotational temperature. As described by Cho et al., [2006] and many ground observers, the fluctuations caused by the atmospheric waves show a positive correlation between intensity and rotational temperature for OH airglow. In this appendix, an example of such fluctuations is presented to see that.

The test observation of OH airglow by the Czerny-Turner-type grating spectrometer was conducted in Uji, Japan (34.90N, 135.80E) on 2nd of May, 2006. This spectrometer is originally prepared to survey the spectra of airglow and aurora in the polar region to find less contaminated OH band from an auroral emission. This spectrometer consists of a collecting mirror, three gratings on a turret, and CCD image sensors as detectors. The field-of-view of the spectrometer is 2.5 (horizontal) × 0.004 (vertical) deg and is directed in the zenith direction. All the details about this spectrometer are described in Suzuki et al. [2008].

Figure 6-1 shows variations in rotational line intensity (upper panel) and rotational temperature (lower panel) of OH 7-3 band observed on May 2, 2006 with the spectrometer. The intensity of the rotational line gradually decreased during the night. Small fluctuations with a period of 1 h also were detected. These fluctuations show typical behavior caused by the atmospheric tide (Large trend) and a gravity wave (1hr variations) through the OH layer. These fluctuations show a positive correlation between intensity and rotational temperature of OH airglow.

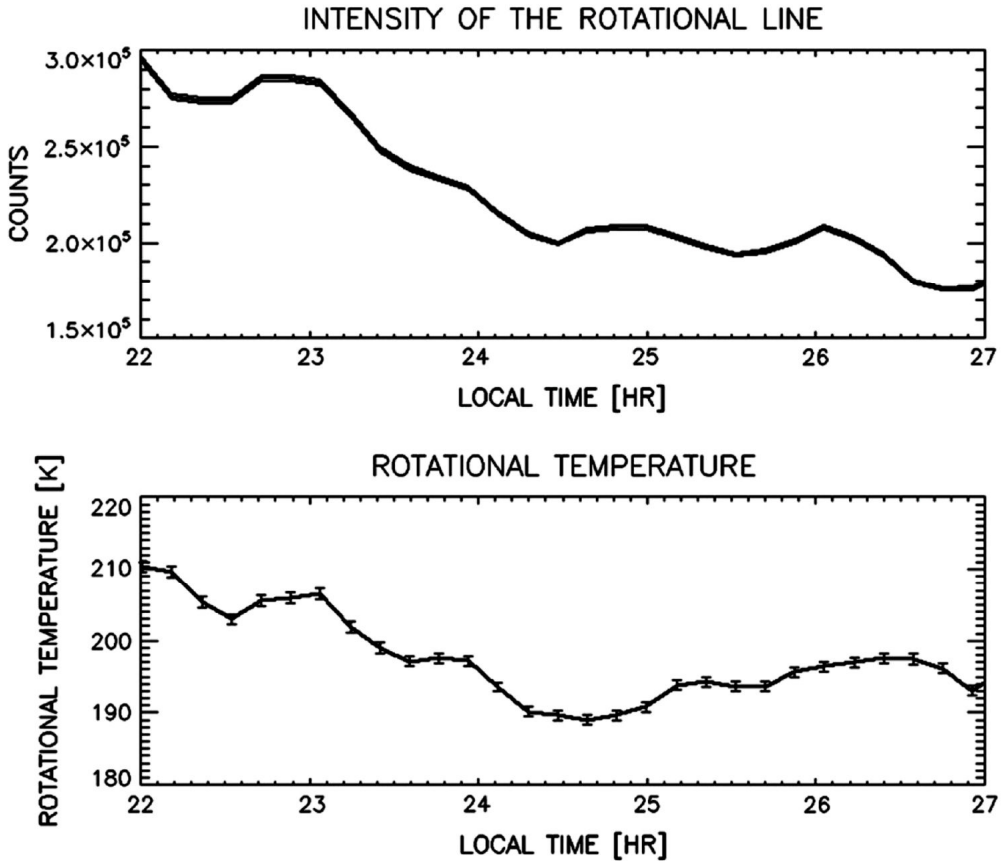

Figure 6-1. Variations in rotational line intensity and rotational temperature observed on May 2, 2006. The intensity is the mean value of rotational lines 2P1, 3P1, and 4P1, of OH 7-3 band. The fitting errors shown by the upper and lower traces are less than 1% and 0.4% for intensity and rotational temperature, respectively.

To see 1 hr period variations more clearly, 60 minutes running mean averaged data is subtracted from Figure 6-1 is shown in Figure 6-2. The positive correlation between intensity and rotational temperature is more clearly seen in this plot. The amplitude of intensity is larger than that of rotational temperature. The relationship between amplitude of intensity and rotational temperature is represented by the equation,

$$\frac{I'}{\bar{I}} = CF \frac{T'_{rot}}{\bar{T}_{rot}}, \qquad (13)$$

where CF is a cancellation factor, prime values are amplitudes of fluctuation caused by the gravity wave, and bars over quantities represent averaged values [Swenson and Liu, 1998]. It is noted that atmospheric temperature T, at a given height and rotational temperature Trot are not the same since the latter is averaged value over OH layer. However if vertical wavelength of a gravity wave is sufficiently larger than thickness of OH airglow layer (~10km), they can be considered as virtually the same. In this case, the vertical wavelength of the gravity wave derived using the horizontal wavelength observed by the all sky imager and the linear dispersion relationship is about 30km. Thus approximation of $T_{rot} = T$ is valid in this case.

According to the model calculations of perturbations caused by upward-propagating waves (downward phase propagation), conducted by Swenson and Liu [1998], the CF for the case on May 2 (λz=30 km) is about 3 ~ 5. This is consistent with the observed fluctuations of OH airglow intensity (2~6%) and rotational temperature (0.5~2%). These are typical features of fluctuation in OH airglow caused by gravity waves.

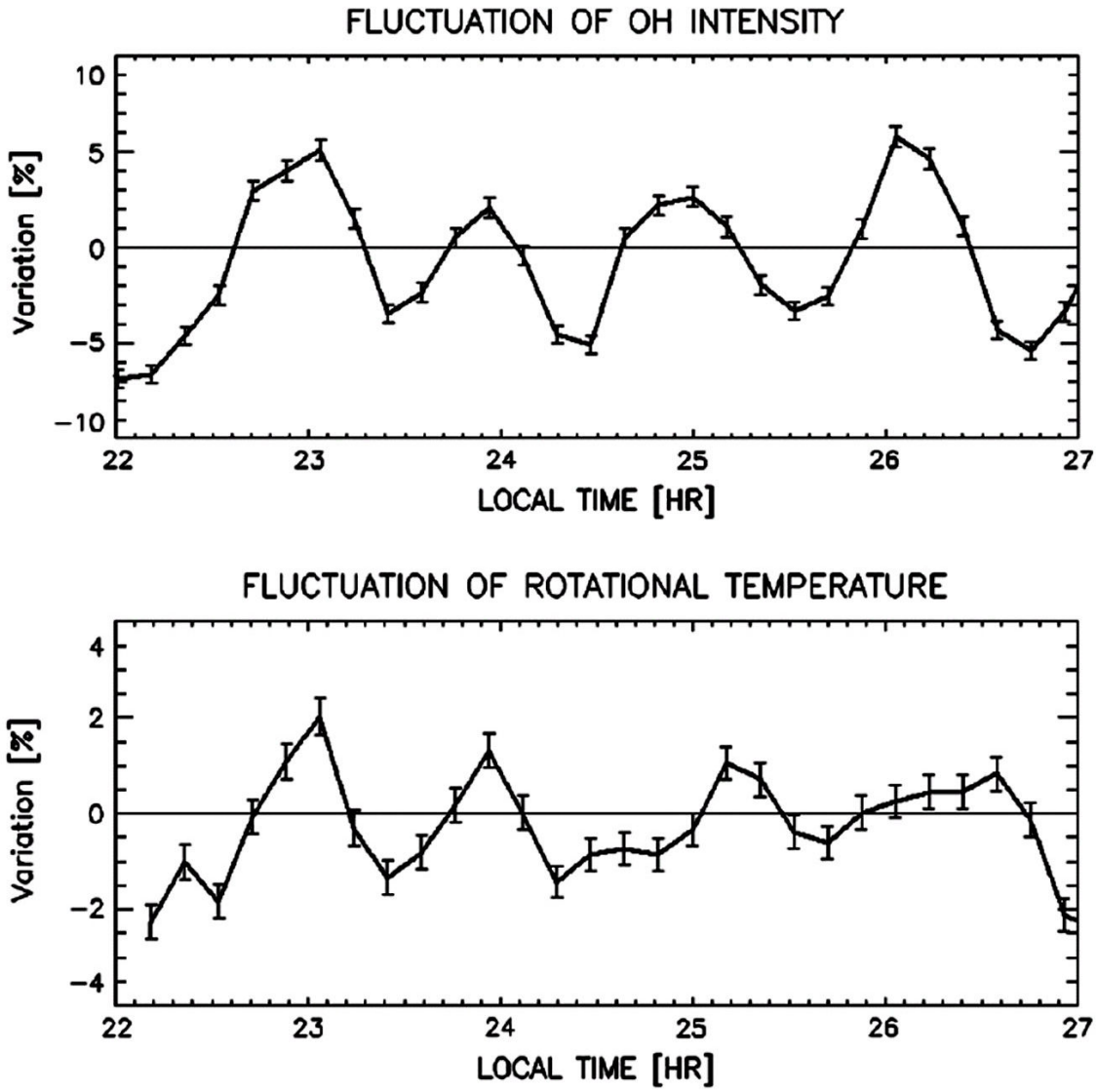

Figure 6-2. Deviations in the rotational line intensity and rotational temperature from the 60-min running average.

References

[1] Baker, D. J. and A. T. Stair, Jr., “Rocket measurements of the altitude distribution of the hydroxyl emission,” Phys. Scr. 37,611–622 (1988)

[2] Bates, D. R. and M. Nicolet, “The photochemistry of atmospheric water vapor,” J. Geophys. Res. 55, 301–327 (1950)

[3] Beig, G., J. Scheer, M. G., Mlynczak, and P., Keckhut, “OVERVIEW OF THE TEMPERATURE RESPONSE IN THE MESOSPHERE AND LOWER THERMOSPHERE TO SOLAR ACTIVITY”, Rev. Geophys., 46, RG3002, (2008)

[4] Berger, M. J., S. M., Seltzer, K., Maeda, J. Atmos. Terr., Phys., 32, pp1015-1045, (1970)

[5] Brekke, A.,” Joule heating and particle precipitation”, Adv. Space Res., Vol.2, No.10, pp.45-53, (1983)

[6] Brekke, A, “Physics of the upper polar atmosphere”, Wiley-Praxis Series in Atmospheric Physics, Praxis Publishing, United Kingdom., (1997)

[7] Brown , L. B., A. J. Gerrard, J. W. Meriwether, and J. J. Makela, “All□sky imaging observations of mesospheric fronts in OI 557.7 nm and broadband OH airglow emissions: Analysis of frontal structure, atmospheric background conditions, and potential sourcing mechanisms”, J. Geophys. Res., 109, D19104, doi:10.1029/2003JD004223, (2004)

[8] Burns, G. B., W. J. R. French, P. A. Greet, F. A. Phillips, P. F. B. Williams, K. Finlayson, and G. Klich, “Seasonal variations and inter-year trends in seven years of hydroxyl airglow rotational temperatures at Davis station (69S; 78E)”, Antarctica, J. Atmos. Sol. Terr. Phys., 64, 1167-1174, (2002)

[9] Chamberlain, J. W., and C. A. Smith, “On the Excitation Rates and Intensities of OH in the Airglow”, J. Geophys. Res., 64(6), 611–614, doi:10.1029/JZ064i006p00611., (1959)

[10] Chandra, S., E. L., Fleming, M. R., Schoeberl, and J.J., Barnett, "MONTHLY MEAN GLOBAL CLIMATOLOGY OF TEMPERATURE, WIND, GEOPOTENTIAL HEIGHT AND PRESSURE FOR 0-120 km", Adv. Space Res., 10, No.6, pp (6)3-(6)12, (1990)

[11] Cho, Y.-M., and G. G. Shepherd, "Correlation of airglow temperature and emission rate at Resolute Bay (74.68°N), over four winters (2001–2005)", Geophys. Res. Lett., 33, L06815, doi:10.1029/2005GL025298 (2006)

[12] Clemesha B. R. and H. Takahash, "Rocket-borne measurements of horizontal structure in the OH(8,3) and Na D airglow emissions", Adv. Spac. Res., Volume 17, Issue 11, Pages 81-84, (1986)

[13] Dick K. A., G.G. Sivjee, and H.M. Crosswhitea, "Aircraft airglow intensity measurements: Variations in OH and OI (5577)", Planet. Spac. Sci., Volume 18, Issue 6, Pages 887-894, (1970)

[14] Dodd, J., S. Lipson, J. Lowell, P. Armstrong, W. Blumberg, R. Nadile, S. Adler, Golden, W. Marinelli, K. Holtzclaw, and B. Green, "Analysis of hydroxyl earthlimb airglow emissions: Kinetic model for state to state dynamics of OH (υ,N)", J. Geophys. Res., 99(D2), 3559-3585, (1994)

[15] Dunkerton, T., "On the Mean Meridional Mass Motions of the Stratosphere and Mesosphere", J. Atmos. Sci., 35, 12, p2525, (1978)

[16] Espy, P. J., R. E. Hibbins, G. O. L. Jones, D. M. Riggin, and D. C. Fritts, "Rapid, large-scale temperature changes in the polar mesosphere and their relationship to meridional flows", Geophys. Res. Lett., 30(5), 1240, doi:10.1029/2002GL016452, (2003)

[17] FIOCCO, G., G. VISCONTI, and F. CONGEDUTI, "Nocturnal Variation of the Intensity and Rotational Temperature of the OH (8,3) Band in the Airglow", Nature 228, 1079 – 1080, doi:10.1038/2281079a0, (1970)

[18] Fleming, E. L., S., Chandra, M. H., Shoeberl, and J. J., Barnett, "MONTHLY

MEAN GLOBAL CLIMATOLOGY OF TEMPERATURE, WIND, GEOPOTENTIAL HEIGHT AND PRESSURE FOR 0-120 km", NASA Technical Memorandum, 100697, (1988)

[19] French, W. J. R. and G. B. Burns, "The influence of large-scale oscillations on long-term trend assessment in hydroxyl temperatures over Davis, Antarctica," J. Atmos. Sol.-Terr. Phys., 66, 493–506 (2004)

[20] French, W. J. R., G. B. Burns, and P. J. Espy, "Anoumalous winter hydroxyl temperatures at 69°S during 2002 in a multiyear context", Geophys. Res. Lett., 32, L12818, doi:10.1029/2004GL022287, (2005)

[21] Frey, H. U., S. B. Mende, J. F. Arens, P. R. McCullough, and G. R. Swenson, "Atmospheric gravity wave signatures in the infrared hydroxyl OH airglow", Geophys. Res. Lett., 27(1), 41–44, doi:10.1029/1999GL010695., (2000)

[22] Fritts,D .C., and P. K., Rastogi, "Convective and dynamical instabilities due to gravity wave motions in the lower and middle atmosphere : Theory and observations", Radio Sci., 20, 1247-1277, (1985)

[23] GATTINGER, R. L., F. R. HARRIS and A. VALLANCE JONES, "THE HEIGHT, SPECTRUM AND MECHANISM TYPE-B RED AURORA AND ITS BEARING ON EXCITATION OF O(3) IN AURORA", Planet. Space Sci., Vol. 33, No. 2. pp. 207-221, (1985)

[24] Gattinger, R., L.,and Vallance, Jones, "The intensity ratios of auroral emission features", Ann. Geophys., 28, pp91-97, (1972)

[25] Giver L. P., Gentry B., Schwemmer G., and Wilkerson T. D., "WATER ABSORPTION LINES, 931-961nm: SELECTED INTENSITIES, N2-COLLISION-BROADNING COEFFICIENTS, AND PRESSURE SHIFTS IN AIR," J. Quant., Spectrosc. Radia. Transfer, Vol. 27, No.4, 423-436 (1982)

[26] Guharay, A., A. Taori, M. Taylor, "Summer-time nocturnal wave characteristics in mesospheric OH and O2 airglow emissions", Earth, Planets and Space, Volume 60, p.

973-979, (2008)

[27] HARRISON, A., W., “Behavior of Hydroxyl Emission During Aurora”, J.Geophys. Res, 75, No.7, 1330 (1970)

[28] Hecht, J., R. Walterscheid, D. Fritts, J. Isler, D. Senft, C. Gardner, and S. Franke, “Wave breaking signatures in OH airglow and sodium densities and temperatures 1. Airglow imaging, Na lidar, and MF radar observations”, J. Geophys. Res., 102(D6), 6655-6668, (1997)

[29] Hedin, A., E., “Extension of the MSIS Thermospheric Model into the Middle and Lower Atmosphere”, J. Geophys. Res. 96, 1159, (1991)

[30] Kendall, D. J. R. and T. A. Clark, “The pure rotational atmospheric lines of hydroxyl,” J. Quant. Spectrosc. Radiat. Transfer 21, 511–526 (1979)

[31] Kieffabera, L. M. and A.W. Petersona, “Structure and fluctuations in the OH airglow at 1.65 μ.”, J. Atmos. Sol.-Terr. Phys., Volume 35, Issue 11, Pages 2013-2022, (1973)

[32] Krassovsky, V. I., “Infrasonic variations of OH emission in the upper atmosphere,” Ann. Geophys. (C.N.R.S.) 28, 739–746 (1972)

[33] Langhoff S. R., Werner H-J., and Rosmus P., “Theoretical transition probabilities for the OH Meinel System,” J. Molecular Spectroscopy, 118, 507–529 (1986)

[34] Lindzen, R. S., “Turbulance and stress owing to gravity wave and tidal breakdown”, J. Geophys. Res., 86, 9707-9714, (1981)

[35] Liu, G., and G. G. Shepherd, “An empirical model for the altitude of the OH nightglow emission”, Geophys. Res. Lett., 33, L09805, doi:10.1029/2005GL025297.(2006)

[36] Liu, A. Z., and G. R., Swenson, “A modeling study of O2 and OH airglow perturbations induced by atmospheric gravity waves”, J. Geophys. Res, 108, NO.D4, 4151, doi:10.1029/2002JD002474 (2003)

[37] Llewellyn E. J. and B.H. Long, “The OH Meinel bands in the airglow—the

radiative lifetime", Can. J. Phys. Rev. can. phys. 56(5): 581-586 (1978)

[38] López-Gonzáleza M. J., M. García-Comasa, E. Rodrígueza, M. López-Puertasa, M.G. Shepherdb, G.G. Shepherdb, S. Sargoytchevb, V.M. Aushevc, S.M. Smithd, M.G. Mlynczake, J.M. Russellf, S. Brownb, Y.-M. Chob and R.H. Wiensg, "Ground-based mesospheric temperatures at mid-latitude derived from O2 and OH airglow SATI data: Comparison with SABER measurements", J. Atmos. Sol.-Terr. Phys., Volume 69, Issues 17-18, Pages 2379-2390, (2007)

[39] Lowe, R. P., K.L. Gilbert and D.N. Turnbull, "High latitude summer observations of the hydroxyl airglow", Planet. Spac. Sci., Volume 39, Issue 9, Pages 1263-1270, (1991)

[40] Makhlouf, U. B., R. H. Picard, and J. R. Winick, "Photochemical-dynamical modeling of the measured response of airglow to gravity waves 1. Basic model for OH airglow", J. Geophys. Res., 100(D6), 11,289–11,311, doi:10.1029/94JD03327, (1995)

[41] Maeda, K., "The auroral O2-dissociation and the infrared OH-emission", Ann. Geophys., 24, 173. , (1968)

[42] Marsh, D. R., A. K. Smith, M. G. Mlynczak, and J. M. Russell III, "SABER observations of the OH Meinel airglow variability near the mesopause", J. Geophys. Res., 111, A10S05, doi:10.1029/2005JA011451. (2006)

[43] Meinel, A. B., "OH emission bands in the spectrum of the night sky," Astrophys. J. 111, 555–564 (1950)

[44] Mies F. H., "Calculated vibrational transition probabilities of OH(X2Π)," J. Molecular Spectroscopy, 53, 150–188 (1974)

[45] Mlynczak, M. G., " Energetics of the mesosphere and lower thermosphere and the SABER experiment", Adv. Space Res., 20(6), 1177–1183, doi:10.1016/S0273-1177(97)00769-2, (1997)

[46] Mlynczak, M., and S. Solomon, "A detailed evaluation of the heating efficiency in the middle atmosphere", J. Geophys. Res., 98, 10,517–10,541, doi:10.1029/93JD00315.

(1993)

[47] Moreels, G., A. V. Jones, and J.E. Blamont, “A Balloon Study of the OH Airglow Emission From Evening Twilight to Sunrise”, Can. J. Phys. Rev. can. phys. 51(9): 888-893 (1973)

[48] Myrabø, H. K., C.S. Deehra and B. Lybekkb, “Polar cap OH airglow rotational temperatures at the mesopause during a stratospheric warming event,” Planet. Spac. Sci., Volume 32, Issue 7, Pages 853-856, (1984)

[49] Myrabø, H. K., G. J. Romick, G. G. Sivjee, and C. S. Deehr, “Night Airglow OH (8–3) Band Rotational Temperatures at Poker Flat, Alaska”, J. Geophys. Res., 89(A10), 9153–9156, doi:10.1029/JA089iA10p09153, (1984)

[50] Myrabø H. K. and O. E. Harang, “Temperatures and tides in the high latitude mesopause region as observed in the OH night airglow emissions”, J. Atmos. Sol.-Terr, Volume 50, Issue 8, Pages 739-748, (1988)

[51] Muraoka, Y., T., Sugiyama, K., Kawahira, S., Sato, T., Tsuda, S., Fukao, and S., Kato, “Cause of a monochromatic inertia-gravity wave breaking observed by the MU radar”, Geophys. Res. Lett., 15, 12,pp1349-1352, (1988)

[52] Nakamura, T., A. Higashikawa, T. Tsuda, and Y. Matsushita, “Seasonal variations of gravity wave structures in OH airglow with a CCD imager at Shigaraki”, Earth Planets Space, 51, 897–906, (1999)

[53] Nielsen, K. P., F. Sigernes, E. Raustein, and C. S. Deehr, “The 20-year change of the Svalbard OH-temperatures,” Phys. Chem. Earth 27, 555–561 (2002)

[54] Okada, M., M., Ejiri, S., Okano, M., Taguchi, and S., Takeshita, “System Design and Initial Result of All Sky Imager at South Pole,” Antarctic Record (Japanese), 41, No.3, 613-630 (1997)

[55] Oliva, E. and L. Origlia, “The OH Airglow Spectrum - a Calibration Source for Infrared Spectrometers”, ASTRONOMY AND ASTROPHYSICS V.254, NO. FEB(I), P. 466, (1992)

[56] Ono, T., “Derivation of energy parameters of precipitating auroral electrons by using the intensity ratio of auroral emissions”, J. Geomag. Geoelectr., 45, pp455-472, (1993)

[57] Onoma S., Y. Otsuka, K. Shiokawa, T. Ogawa, M. Yamamoto, S. Fukao, S. Saito, “Relationship between propagation direction of gravity waves in OH and OI airglow images and VHF radar echo occurrence during the SEEK-2 campaign”, Ann. Geophys. 23, 7, 2385-2390, (2005)

[58] Oznovich, I., D. J. McEwen, and G. G. Sivjee, “Temperature and airglow brightness oscillations in the polar mesosphere and lower thermosphere,” Planet. Space Sci. 43, 1121–1130 (1995)

[59] Pendleton, W. R. Jr., P. J. Espy, and M. R. Hammond, ”Evidence for non-local-thermodynamic-equilibrium rotation in the OH nightglow,” J. Geophys. Res. 98(A7), 11567–11579, (1993)

[60] PETERSON, A.W. and L. M. KIEFFABER, “Infrared Photography of OH Airglow Structures”, Nature 242, 321 – 322, doi:10.1038/242321a0, (1973)

[61] Pick, D. R. Llewellyn, E. J. Jones, A. V, “Twilight airglow measurements of the OH and O2 bands by means of balloon-borne instruments.”, Can. J. Phys., Vol. 49, p. 897 - 905, (1972)

[38] Russel, J. M. Ⅲ, M. G., Mlynczak, L.L., Gordley, J., Tansock, and R., Esplin, “An over view of the SABER experiments and preliminary calibration results”, Proc. SPIE, 3756, 277-288, (1999)

[62] Rees, M. H., and D., Luckey, “Auroral electron energy derived from ratio of spectroscopic emissions 1. Model computations”, J., Geophys. Res., 79, 5158-5186, (1974)

[63] Rees, D., “CIRA86”, Adv. Space Res., Vol. 8, NO. 5-6, (1988)

[64] Rohen, G., et al., “ Ozone depletion during the solar proton events of October/November 2003 as seen by SCIAMACHY ”, J. Geophys. Res., 110, A09S39,

doi:10.1029/2004JA010984.,(2005)

[65] Seppälä, A., P. T. Verronen, E. Kyrölä, S. Hassinen, L. Backman, A. Hauchecorne, J. L. Bertaux, and D. Fussen, “Solar proton events of October–November 2003: Ozone depletion in the Northern Hemisphere polar winter as seen by GOMOS/Envisat.”, Geophys. Res. Lett., 31, L19107, doi:10.1029/2004GL021042, (2004)

[66] Sigernes, F., N. Shumilov, C. S. Deehr, K. P. Nielsen, T. Svenoee, and O. Havnes, “Hydroxyl rotational temperature record from the auroral Station in Adventdalen, Svalbard (78N,15E)”, J. Geophys. Res, 108, No.A9, SIA3-1 (2003)

[67] Shiokawa , K., M. K. Ejiri, T. Ogawa, Y. Yamada, H. Fukunishi, K. Igarashi, and T. Nakamura, “A localized structure in OH airglow images near the mesopause region”, J. Geophys. Res., 108, 4048, doi:10.1029/2002JD002462, (2003)

[68] Sivjee, G. G., K. K. Dick, and P. D. Feldman, “Temporal variations in night-time hydroxyl rotational temperature,” Planet. Space Sci. 20, 261–269 (1972)

[69] Stubbs, L. C., J. S. Boyd, and F. R. Bond, “Measurement of the OH rotational temperatures at Mawson, East Antarctica,” Planet. Space Sci. 31, 923–932 (1983)

[70] Suzuki, H.,” Study of the polar mesopause region by remote sensing of OH airglow.”, Master Thesis of the author, (2006)

[71] Suzuki, H., T., Nakamura, M. Tsutsumi, M., Taguchi “Atmospheric gravity waves identified by ground-based observations of the intensity and rotational temperature of OH airglow,” Polar Sci. 2(1), 1–8 (2008)

[72] Suzuki, S., K. Shiokawa, Y. Otsuka, T. Ogawa, M. Kubota, M. Tsutsumi, T. Nakamura, and D. C. Fritts, “Gravity wave momentum flux in the upper mesosphere derived from OH airglow imaging measurements”, Earth Planets Space, 59, 421–428, (2007)

[73] Swenson, G.R., Liu, A.Z., “A model for calculating acoustic gravity wave energy and momentum flux in the mesosphere from OH airglow.”, Geophys. Res. Lett. 25 (4), pp477-480., (1998)

[74] Takahashi, H., B. R. Clemesha, and Y. Sahai, “Nightglow OH(8,3) band intensities and rotational temperature at 23°S,” Planet. Space Sci. 22, 1323–1329 (1974)

[75] Takahashi, H., T. Nakamura, T. Tsuda, R. A. Buriti, and D. Gobbi, First measurement of atmospheric density and pressure by meteor diffusion coefficient and airglow OH temperature in the mesopause region, Geophys. Res. Lett., 29(8), 1165, doi:10.1029/2001GL014101, (2002)

[76] Takeuchi, I., K. Misawa, Y. Kato, and I. Aoyama, Rotational temperatures and intensities of OH(6-2) and OH(8-3) bands in the night airglow, J. Atmos. Sol.-Terr. Phys., Volume 41, Issue 4, Pages 387-395, (1979)

[77] Tang, J., A. Z. Liu, and G. R. Swenson, “High frequency gravity waves observed in OH airglow at Starfire Optical Range, NM: Seasonal variations in momentum flux”, Geophys. Res. Lett., 29(20), 1966, doi:10.1029/2002GL015794, (2002)

[78] Taylor, M. J., and M. J. Hill, “Near infrared imaging of hydroxyl wave structure over an ocean site at low latitudes”, *Geophys. Res. Lett.*, 18(7), 1333–1336, doi:10.1029/91GL01299, (1991)

[79] Taylor, M. J., D. N., Turnbull and R. P., Lowe, “Spectrometric and imaging measurements of spectacular gravity wave event observed during the ALOHA-93 campaign”, Geophys. Res. Lett., 20, No.20, pp2849-2852, (1995)

[80] Vadas, S. L., M. J. Taylor, P.-D. Pautet, P. A. Stamus, D. C. Fritts, H.-L. Liu, F. T. Sao Sabbas, V. T. Rampinelli,P. Batista, and H. Takahashi, “Convection: the likely source of the medium-scale gravity waves observed in the OH airglow layer near Brasilia, Brazil, during the SpreadFEx campaign”, Ann. Geophys., 27, 231–259, (2009)

[81] Vallance Jones, A. , “Auroral spectroscopy,” Space Sci. Rev. 11, 776–826 (1971)

[82] Walterscheid, R., and G. Schubert, “Dynamical□Chemical Model of Fluctuations in the OH Airglow Driven by Migrating Tides, Stationary Tides, and Planetary Waves”, J. Geophys. Res., 100(A9), 17443-17449, (1995)

[83] Watanabe, T., M. Nakamura, and T. Ogawa, “Rocket Measurements of O2

Atmospheric and OH Meinel Bands in the Airglow", J. Geophys. Res., 86(A7), 5768-5774, (1981)

[84] Wehrbein, W. M., and C. B., Leoby, "An accurate radiative heating and cooling algorithm for use of dynamical model of middle atmosphere", J. Atmos. Sci., 39, p1532, (1982)

[85] Winick, J., R., P., P., Wintersteiner, R., H., Picard, D., Esplin, M. G., Mlynczak, J., M., Russell III, and L., L., Gordley, "OH layer characteristics during unusual boreal winters of 2004 and 2006", J. Geophys. Res, 114, A02303, (2003)

[86] Won, Y. I., Y. M. Cho, R. J. Niciejewski and J. Kim, "Observations of OH(3,1) airglow emission using a Michelson interferometer at 62°S", Adv. Spac. Res., Volume 27, Issues 6-7, Pages 1165-1170, (2001)

[87] Xun Z., J. Yee, and E. R. Talaat, "Diagnosis of Dynamics and Energy Balance in the Mesosphere and Lower Thermosphere", J. Atmos. Sci., 58, p2441, 2001

[88] Yamada, Y., H. Fukunishi, T. Nakamura, and T. Tsuda, "Breaking of small□scale gravity wave and transition to turbulence observed in OH airglow", Geophys. Res. Lett., 28(11), 2153–2156, doi:10.1029/2000GL011945, (2001)